Erosion and Air Entrainment by Stationary and Translating Circular Jets

by

Mahmud Rashedul Amin

A thesis submitted in partial fulfillment of the requirements for the degree of

Doctor of Philosophy

in

WATER RESOURCES ENGINEERING

Department of Civil and Environmental Engineering
University of Alberta

ABSTRACT

Circular turbulent jets are essential in many engineering applications and are thoroughly studied. Most of these studies involve stationary jets. Contemporary studies lack the understanding of translating jets partly because the experimental setup is complicated, and computational models cannot simulate air entrainment and scour by translating jets reliably. This thesis presents some phenomena related to translating turbulent circular jets: scouring sand beds, air entrainment in a quiescent waterbody, and impingement on a flat wall. These phenomena of translating jets were compared against stationary jets. However, there is a research gap in the scouring of sand beds by short impinging circular jets. Therefore, an experimental study of stationary short-impinging jet scouring was also conducted.

The scouring of sand beds by stationary jets is crucial because the failure of hydraulic structures is often related to the downstream scouring of these structures. Many studies have been conducted previously on the scour of sand beds by circular jet of long impinging height of more than 8.3 times the jet diameter. The potential core of such a jet is completely diffused before it impinges on the bed. However, shallow waterbodies are often subjected to scouring by short jets of impinging height 5.5 times the jet diameter. Short impinging height is essential because it ensures a uniform jet velocity and strong impingement. Laboratory experiments were conducted with short axisymmetric jets and sands with mean diameters of 0.54 and 1.1 mm. Semi-empirical prediction equations for the ultimate scour hole and temporal development of the unsteady scour hole was developed.

Practical applications like the fluidization of sand beds for dredging and clam collection, sewer cleaning, and movement of water vessels in shallow waterbodies involve sand beds scouring with translating jets. Therefore, experiments were conducted in a towing tank with a submerged sand bed and circular turbulent jets of different translating velocities to assess the erosion of sand beds under varied hydraulic conditions. A half-model configuration was used with a high-speed camera mounted at the side of the tank to capture sand movement using the Particle Image Velocimetry (PIV) technique. PIV analysis revealed the dynamics of the sand movement and properties of the dynamic scour by translating jets.

Air entrainment by jets is useful in many industrial applications. Many studies are available on air entrainment by stationary jets. However, the mechanism of air-entrainment by a translating jet could be different. An experimental study was conducted with translating turbulent circular jets impinging in a quiescent water pool to study the air entrainment mechanism and bubble characteristics. Shadowgraph images taken with a high-speed camera were used for analysis. It was found that the maximum penetration depth of the bubbles is a function of the jet translating speed and the Capillary number of the air-water interface. The spatial distribution of the bubbles in the bubble swarm cross-section shows Gaussian distribution. However, the terminal velocity of the bubbles shows no noticeable effect of the jet translation.

The impingement of jets is a significant engineering problem. Such problems include jet issuing from hydraulic outlets, the vertical takeoff of space-rovers, and spraying devices. A translating jet impingement adds more complexities to the stationary jet impingement problem. A submerged translating jet is typically subjected to the relative crossflow and the relative drag of the impingement surface. Therefore, laboratory experiments and numerical simulations were conducted to understand the complex interaction between the translating jet and the impingement surface. The experiments were performed inside a towing tank with a 19 mm diameter translating jet. The PIV technique was used to capture the velocity field. Computational Fluid Dynamics (CFD) models were developed for translating jet velocities ranging between 0.03 and 0.09 m/s in OpenFOAM software. The CFD results were compared against the PIV experiments. In addition to the velocity field, the CFD models provided the distribution of the wall pressure and shear stress in the impingement region and the effect of different translating velocities.

In summary, this thesis presents experimental and computational studies related to stationary and translating circular turbulent jets. Practical applications of this work include but are not limited to water injection dredging, submarine cable trenching, shellfish collection, sewer cleaning, and scouring by moving water vessels and space rovers.

PREFACE

This thesis is an original work by Mahmud Rashedul Amin under the supervision of Dr. David Zhu and Dr. Nallamuthu Rajaratnam. My supervisors and I compiled all the published, submitted, and to-be-submitted research works.

The laboratory experiments and numerical models described in Chapters 3 to 6 were planned and executed by myself. The data analysis and simulation conducted in this thesis are my original work with directions from my supervisors.

Chapter 3 of this thesis has been published as: Amin, M. R., Rajaratnam, N., and Zhu, D. Z. (2021). Scouring of sand beds by short impinging turbulent jets. Proceedings of the Institution of Civil Engineers – Water Management, 174(6), 309-320. I was responsible for designing and conducting the experiments, data collection and analysis, and writing the manuscript. Dr. D. Zhu and N. Rajaratnam were the supervisory authors and assisted in the manuscript editing.

Chapters 4 and 6 are currently being prepared as journal manuscripts. Chapter 5 has been submitted as a journal manuscript: Amin, M. R., Zhu, D. Z., and Rajaratnam, N. (2021). Air-bubble entrainment in stagnant water by translating turbulent jets. International Journal of Multiphase Flow, under review.

I also contributed to the following publications:

Amin, M. R., Rajaratnam, N., and Zhu, D. Z. (2022). Flow and energy loss downstream of rectangular sharp-crested weirs for free and submerged flows. ASME Journal of Fluids Engineering, 144(3), 031201.

Amin, M.R., Rajaratnam, N., and Zhu, D. (2022). Scour of Sand Beds by Long and Short Impinging Jets- Similarities and Differences. Proceedings of 39th IAHR World Congress, Granada, Spain, pp. 1–7.

Amin, M.R., Rajaratnam, N., and Zhu, D. (2019). Energy loss below rectangular sharp-crested weirs for free flows. Proceedings of 38th IAHR World Congress, Panama City, Panama, pp. 1–7.

To my parents Mr. Muhammad Golam Rasul and Mrs. Rizia Khanam,

and my family for unconditional support, sacrifice, and inspiration

ACKNOWLEDGMENTS

TABLE OF CONTENTS

LIST OF TABLES

LIST OF FIGURES

LIST OF SYMBOLS

Symbol	Definition
b	half-radius of the scour hole so that at $r = b$, $\varepsilon = \varepsilon_m/2$
Ca	Capillary number for the air-water interface, $Ca = \mu_w V_i/\sigma_w$
C_p	Pressure coefficient
d	Jet diameter at nozzle
D_{50}	mean diameter of the bed material
$\Delta\rho$	density difference for bed material and fluid
D_b	Bubble diameter
d_t	Jet dimeter in the half-model configuration of scour test
E_c	Erosion parameter
f	frequency of the vortex shedding by a translating jet in stagnant water
F_d	Densimetric Froude number, $F_d = V_j/[\{(\rho_w-\rho_s)/\rho_w\}gD_{50}]^{1/2}$
Fr	Froude number, $Fr = U_j^2/gL$
g	Acceleration by gravity
h	Impinging height of the jet
H	Maximum penetration depth of the bubble plume for a translating jet
H_0	Maximum penetration depth of the bubble plume for a stationary jet

L	Characteristic length
L^*	Length ratio, $L = \lambda/L$
L_p	Length of the potential core
Mo	Morton number, $Mo = g\mu_w^4 \rho_w^{-1} \sigma_w^{-3}$
P_a	Ambient pressure
P_D	Probability density distribution of the bubble sizes
P_s	Static pressure on the wall due to jet impingement
r	Radial distance from the center of the scour hole
R	Ratio of the jet translating velocity to the jet velocity at the nozzle, $R = U_t / V_j$
r_0	radius of the scour hole
Re	Jet Reynolds number, $Re = \rho_w V_j d / \mu_w$
R_{it}	Ratio of the jet impact velocity to the jet translating velocity, $R_{it} = V_i / U_t$
R_{jc}	Jet velocity to crossflow velocity ratio, $R_{jc} = U_j/U_t$
R_{ti}	Ratio of the jet translating velocity to the jet velocity at the nozzle, $R_{ti} = U_t / V_j$
S_{tr}	Strouhal number, $S_{tr} = fD_j/U_t$
t	Time of scour
$u`$	Fluctuation velocity of the local disturbances at air-water interface
U^+	Fluctuation intensity, $U^+ = u`/U_j$
U_t	Translating velocity of the jet

V_i Average jet velocity at the location of impact with the water surface

V_j Jet velocity at nozzle

We   Weber number, $We = \rho_w V_i^2 D_j / \sigma_w$

α The angle of inclination of the jet in the direction of the jet translation

α_b Probability of bubble occupancy

α_r Submerged angle of repose of sand

δ Ridge height of the scour hole

ε Static scour depth at distance r

ε_d Dynamic scour depth

θ Shields' parameter

λ Wavelength of the vortex shedding by a translating jet in stagnant water

λ_l Wavelength of local disturbances at air-water interface

μ Kinematic viscosity of fluid

μ_b Logarithmic mean of the bubble diameter

ρ Density of the jet fluid

σ_b Log standard deviation of the bubble diameters

σ_s Non-uniformity of sand

σ_w Surface tension at the air-water interface

τ_0 Shear stress on the impingement wall or bed

Subscripts

∞	Asymptotic condition of the scour hole
m	maximum
w	Water

CHAPTER 1. GENERAL INTRODUCTION

1.1 Background

Numerous challenging problems in fundamental research and industrial contexts involve the applications of turbulent jets. These applications include fluid mixing by jets, cooling thermal components by jet impingement, cleaning or removing objects coating using high-pressure jets, scouring loose beds, cutting metals, generating propulsion of aircraft, marine or spacecraft, and many other applications. However, although many studies have been conducted on the applications of stationary turbulent jets, studies related to translating jets are limited. Nevertheless, many industrial applications require the use of translating jets.

The motivation of this study is threefold. First, although the stationary jets have been studied extensively, some specific problems in multiphase flow regimes need careful experimental study. For example, problems like loose-bed scouring by jets placed close to the bed need more attention because of the vast extent of practical applications. An analytical solution for this type of multiphase problem is complicated, and a numerical solution is unreliable until validated with experimental data. Second, the characteristics of a translating jet are not well understood. Despite having some similarities with jets in a crossflow, the presence of a fixed boundary near the jet makes the translating jet characteristics different. For example, erosion of a loose bed or impingement on a flat wall by a submerged translating jet is fundamentally different from a jet in a crossflow. Unlike the jet in a crossflow, both the ambient fluid and fixed boundary have relative velocities with respect to the translating jet. Third, previous studies are mostly limited to stationary jets because it is difficult to conduct experiments with moving or translating jets, and the translation of the jet adds more complexities to the analytical or numerical solution of such problems.

Based on the above-stated motivations, the following studies have been conducted using circular turbulent jets.

1.1.1 Scouring of Sand Beds by Short-Impinging Turbulent Jets

Previously, many experimental studies have been conducted to study the scouring of sand beds by

circular turbulent jets of long impinging heights so that the impingement occurs at the developed region of the jet. This technique is particularly advantageous in correlating the diffusion of the jet with the applied shear stress on the soil surface (e.g., see Hanson and Cook, 1997) and developing prediction equations for the amount of scour. However, many engineering applications require the jet to be placed close to the impingement surface, as it ensures a uniform velocity distribution and strong impingement. Furthermore, the extent of the impingement region and length scales for long and short jet impingement is different (Beltaos and Rajaratnam, 1977). Therefore, an experimental study of sand bed scouring with short impinging circular turbulent jets is presented here as an effort to fill the research gap in scouring by stationary jets and use the acquired experience in scouring by translating jets.

1.1.2 Erosion of Sand Beds by Translating Turbulent Jets

Scour by sand bed by translating jets has many practical applications, including channel bed fluidization to facilitate dredging or clam collection, removal of dumped rock cover, trenching of seabed for laying of submarine cables or pipes, and sewer cleaning. Although previous studies primarily focused on scouring by stationary jets, studies on scouring by translating jets are limited. This is because the experimental setup for translating jet is complicated. Contrary to the stationary jet scouring experiments, a translating jet does not stay in the same location of the sand bed to cause a significant amount of scouring. Thus, this study hypothesizes that scouring by a translating jet will be less than a stationary one and will depend on the translating velocity of the jet. An experimental study is conducted for scour testing of sand beds with translating circular turbulent jets.

1.1.3 Air Entrainment by Translating Turbulent Plunging Jets

Mechanisms of air entrainment by plunging jets are complicated and depend on many factors like the jet impact velocity, interacting fluid properties, jet diameters, and the plunging height of the jet. Contemporary knowledge of the air entrainment by stationary plunging jets is still inadequate. For a translating plunging jet, the air entrainment process is more complicated and requires research attention as it has some critical industrial applications like oxygenation and effluent mixing. Due to the translation of the plunging jet, the submerged portion of the jet has similarities with a jet in crossflow. Further, the air bubbles generated in this process have a relative movement in the upstream direction. This feature and the vortices generated with a translating jet may affect

2

the air bubble characteristics. An experimental study is conducted in the laboratory using a towing tank filled with water and translating circular plunging jets of different diameters, impinging height, and impact velocities. The hypothesis of this study is that the mechanism of air entrainment, bubble characteristics and maximum penetration depth of the bubbles will be affected by the jet translation.

1.1.4 Impingement of Translating Turbulent Jets on a Flat Wall

Many studies have been conducted on the normal and oblique impingement of submerged circular turbulent jets on a solid surface. Typically, the flow is characterized by different regions, and these regions are simplified into different jets or shear flows, namely the free circular jet and radial wall jet. Along with the mechanics of the jet, previous researchers also looked into energy dissipation, shear stress, and pressure on the wall. Understanding of the impingement of jets facilitated its application in many industrial processes, including drying textiles, cooling turbine blades, and annealing metal sheets. However, some of these applications relate to either a translating jet or a moving impingement surface. Although the instrumentation for this problem is complicated, being a single-phase problem, a numerical study for such a problem is easier to conduct to get reliable results. This study includes the development of computational fluid dynamics (CFD) models to study the impingement of a translating circular turbulent jet of different translating velocities and an experimental study using the particle image velocimetry (PIV) technique to validate the CFD models.

1.2 Research Objectives

This research aims to understand some specific features of translating turbulent jets: scouring of sand beds, air-entrainment in a stagnant waterbody, and impingement on a flat surface. Towards this overall aim, the specific objectives of this thesis are the followings:

1. To understand the scouring of sand beds by short-impinging stationary circular turbulent jets, and to develop semi-empirical solutions to estimate temporal and asymptotic scour dimensions for jets of any impinging height.

2. To understand the mechanism of sediment motion for sand bed scouring by translating circular turbulent jets, and to develop empirical equations to estimate the dynamic scour depth for

3

circular jets of different translating velocities and impingement angles.

3. To investigate the air entrainment mechanism in quiescent waterbody due to the impact of translating circular turbulent jets, and assess the air-bubble characteristics, i.e., bubble distribution, diameter, and relative velocity.

4. To understand the mechanics of translating jet impingement on a flat wall and estimate corresponding parameters, i.e., velocity distribution, pressure, and shear stress on the wall using computational fluid dynamics (CFD) models.

1.3 Organization of the Thesis

This thesis is organized into eight chapters. In Chapter 2, a review of literature on topics related to this thesis has been conducted. Chapters 3 and 4 present experimental studies of the scouring of sand beds by stationary and translating circular jets, respectively. Chapter 5 demonstrates another experimental study on the air entrainment in stagnant water by translating plunging jets. In Chapter 6, numerical studies and experimental validation for the impingement of translating circular jets on a flat wall are conducted. Chapter 7 includes a summary of the observations and conclusions developed from the study and recommendations for future research. Finally, Appendix A shows an analytical study of the flow and energy dissipation below a sharp-crested weir using the theory of plane jet.

CHAPTER 2. LITERATURE REVIEW

2.1 Introduction

This chapter contains a literature review of previous studies related to the topics of this thesis. Since the studies associated with translating jet applications are novel and very limited, this section primarily focused on the acquired knowledge of stationary jet experiments, except for a review on jets in crossflow. However, the following chapters of this thesis contain reviews of corresponding translating jet applications.

2.2 Sand Bed Scouring by Circular Turbulent Submerged Jets

A good number of studies are available on the scour of cohesionless soils by circular turbulent jets (e.g., Aderibigbe and Rajaratnam, 1996; Bombardelli, Palermo, and Pagliara, 2018; Gioia and Bombardelli, 2005; Palermo, Bombardelli, and Pagliara, 2018; Westrich and Kobus, 1973, to name a few). The scouring of the sand bed occurs due to the applied shear stress by the jet on the soil surface. Before erosion occurs, the applied shear stress on the soil bed is maximum because the impingement height is minimum. As the soil erodes, the effective impingement height of the jet increases. Consequently, the applied shear stress reduces, and the erosion rate becomes very slow. This phase is typically termed the asymptotic phase. In the scouring of cohesionless soils with circular impinging jets, more than 70% of the total scour occurs in only the first 30 minutes (Rajaratnam, 1982).

Previous studies reported that at the beginning of scouring, the maximum scour depth occurs at a small distance away from the point of jet impingement (Poreh and Hefez, 1967; Rajaratnam and Beltaos, 1977). This is a result of the distribution of the boundary shear stress on the soil surface imposed by the impinging circular turbulent jet (Rajaratnam and Beltaos 1977). Later in the scouring process, the maximum scour depth occurs at the point of impingement. The formation of a circular ridge is observed around the periphery of the scour hole as the eroded sand particles eventually deposit there.

The characteristic lengths of the scour hole (e.g., the maximum scour depth) grow linearly with the logarithm of time (Rouse, 1939). After an appreciable amount of time, this length approaches

an asymptotic value. The dimensionless plots of the growth of the scour hole depth are similar (Rajaratnam and Beltaos, 1977). Ansari et al. (2003) provided an empirical relation using a sine function to describe the temporal development of the scour hole depth. The sine function is advantageous since the logarithmic relationship is invalid near the initial and asymptotic phase of the scouring process. However, during the intermediate stage of scouring, the sine function may not describe the scouring process well compared to the logarithmic relation.

Haehnel et al. (2008) simplified the impinging jet scouring problem assuming that the sand particles leave the bed surface due to excessive shear stress under uniform flow parallel to the bed surface, and provided an expression for scouring hole growth as a function of the sediment properties and jet characteristics. Here, excess shear stress denotes the amount of shear stress over the critical shear stress at which an impending motion of the sand particles occurs. However, this expression underestimates the depth of erosion for sand in the intermediate stages of the scour testing. Bombardelli et al. (2018) assumed that the rate of scour at any time could be scaled with the excess shear stress at that particular time and provided a relation for scour hole growth as a function of the sediment properties and jet characteristics like Haehnel et al. (2008). However, this requires the estimation of the asymptotic scour hole depth.

To estimate the asymptotic scour depth, Aderibigbe and Rajaratnam (1996) adopted a dimensionless parameter, named the erosion parameter E_c, given by $E_c = V_{\mathrm{j}}(d/h)/\sqrt{gD_{50}\Delta\rho/\rho}$, where V_{j} is the jet velocity at the nozzle, d is the jet diameter, h is the impingement height, g is the gravitational acceleration, D_{50} is the mean diameter of the bed material, and $\Delta\rho$ is the difference between the bed material density and fluid density ρ. The erosion parameter represents the ratio of the force acting on the sediment bed directly under the jet at the uneroded bed level to the corresponding resistive force due to the buoyant weight of the particle. With the introduction of E_c, it has become possible to estimate the asymptotic scour depth $\varepsilon_{m\infty}$ using a simple expression as a function of E_c.

$$\frac{\varepsilon_{m\infty}}{h} = 1.3E_c^{0.15} - 1 \tag{2.1}$$

Adopting the phenomenological theory of turbulence, Bombardelli and Gioia (2006) developed a theoretical expression for the asymptotic scour depth. However, this contains similar parameters

as used in the equation of Aderibigbe and Rajaratnam (1996).

Previous studies reported that the asymptotic scour holes are self-similar, and the dimensionless scour hole in asymptotic conditions can be expressed as a Gaussian equation (e.g., Aderibigbe and Rajaratnam, 1996; Rajaratnam, 1982, and others),

$$\frac{\varepsilon}{\varepsilon_{m\infty}} = e^{-0.693(r/b_{m\infty})^2} \tag{2.2}$$

where r is the radial distance measured from the jet centerline; ε is scoured depth below the original bed level at distance r; $b_{m\infty}$ is the half-radius of the scour hole so that at $r = b_{m\infty}$, $\varepsilon = \frac{1}{2}\varepsilon_{m\infty}$.

Studies by Aderibigbe and Rajaratnam (1996), Rouse (1939), and Westrich and Kobus (1973) showed that two distinctive flow regimes might exist in the equilibrium scour hole. Rouse (1939) described the "Maximum Jet Deflection" flow regime where the flow turns back on itself inside the scour hole by about 180°, and the "Minimum Jet Deflection" flow regime was where the jet flowed along the boundary of the scour hole ridges. Westrich and Kobus (1973) identified "Scour Form I" and "Scour Form II" flow regimes based on the flow characteristics inside the equilibrium scour hole. Aderibigbe and Rajaratnam (1996) classified the flow regimes for the equilibrium scour hole as the "Strongly Deflected Jet Regime" (SDJR) when $E_c > 0.35$ and "Weakly Deflected Jet Regime" (WDJR) when $E_c < 0.35$.

In the SDJR flow regime, the deflected jet carries lots of sediment in suspension, and the suspended sediments recirculate with the flow inside the scour hole. The flow is weak near the periphery of the scour hole, which results in the deposition of some sediments and the formation of a ridge. The suspended sediments settle inside the scour hole if the jet is stopped during scour testing. Therefore, the dynamic scour hole depth is greater than the static one for the SDJR. In the WDJR flow regime, the jet weakly penetrates the bed, and the flow follows the boundary of the scour hole. Typically, the amount of suspended sediments inside the scour hole is minimal. This results in almost the same dynamic and static scour depth for the WDRJ.

2.3 Air Entrainment by Circular Turbulent Plunging Jets

Many factors may contribute to air entrainment in the waterbody by a plunging jet. According to

Kiger and Duncan (2011), the dominant nondimensional groups relevant to this problem are Froude number, $Fr = V_j^2/gL$; Weber number, $We = \rho_w V_j^2 L/\sigma$; Capillary number, $Ca = \mu_w V_j/\sigma$; Reynolds number, $Re = \rho_w V_j d/\mu_w$; density ratio, $\gamma = \rho_a/\rho_w$; viscosity ratio, $M = \mu_a/\mu_w$; fluctuation intensity, $U^* = u'/V_j$; and length ratio, $L^* = \lambda_l/L$. Here, g is the acceleration by gravity, L is a reference length, ρ is the density, μ is the dynamic viscosity, σ is the surface tension of the air-water interface, u' is the fluctuation velocity of the local disturbances, and λ_l is the wavelength of the disturbances. Subscripts a and w refer to the properties of air and water, respectively. Inception conditions of air entrainment for low viscosity fluids like water are often characterized by the value of the critical Reynolds number and the Capillary number.

Inception conditions for air entrainment by stationary jets have been studied extensively in previous works. In general, previous studies characterized the plunging jets into two regimes for air entrainment purposes- the continuous jet and the droplet regimes. Only the continuous jet regime will be considered in this study, which implies the jet does not break up before it impacts the water surface. For low-density fluids like water, the air entrainment may result from the low pressure due to the entrainment of the surrounding water. Also, air may entrain in the boundary layer of a jet with higher surface disturbances before it plunges into the waterbody (Sene, 1988). Typically, the jet pulls down the water surface at the impact point and forms a conical meniscus surrounding the jet. Air pockets form at the confluence of the jet and the meniscus, which may detach and create air bubbles at higher jet velocities. This is why the impact velocity of the jet plays a dominant role in the inception of air entrainment (Kiger and Duncan, 2011). McKeogh and Ervine (1981) reported that for air-water systems, the critical air entrainment conditions occur for $Re = 2000$ and $Ca = 0.04$.

As a result of the air entrainment due to the impact of the plunging jet in waterbodies, air bubbles generate below the water surface. The air bubbles are observed to disperse in two distinct regions – a biphasic conical region surrounding the jet with smaller bubbles of diameters 1 mm or less and a region with bigger rising bubbles (Biń, 1993). In the biphasic conical region, the bubbles are pushed down by the momentum of the jet, and some bubbles may coalesce and get bigger. At the maximum penetration depth, the buoyancy force of the bubbles and the downward momentum force of the jet becomes equal. The bubbles then escape sideways, get free from the jet momentum and rise freely due to buoyancy. Typically, the Sauter diameter of the rising bubbles is independent

of the jet velocity or nozzle size and ranges between 3 to 4 mm (Biń, 1993). The bubble size distribution in the biphasic conical region is typically a log-normal distribution, skewed to the smaller-sized bubbles (Evans et al., 1992).

Although the maximum penetration depth for individual bubbles may vary, studies were conducted to find the average maximum penetration depth of the bubble. Many studies relied on the assumption that at maximum penetration depth, the rising velocity of the bubbles must be equal to the local jet velocity (e.g., Ervine and Falvey, 1987; Guyot et al., 2019; and others). However, buoyancy forces resulting from the entrained air make this problem complicated. Cumming (1975) carried out a theoretical study and showed that the maximum penetration depth is a function of the square of the jet velocity and the entrainment ratio. Other studies mainly provided purely empirical relations for estimating the maximum bubble penetration depth.

2.4 Impingement of Circular Jets on a Flat Wall

The normal impingement of a submerged circular jet against a flat wall is well studied by Beltaos and Rajaratnam (1974), Nishino et al. (1996), and Rajaratnam et al. (2010), among others. The flow pattern for such jet impingement can be divided into three distinct flow regions. The flat wall does not affect the flow in the first region, and the jet behaves like a free jet. Therefore, this region is called the "Free Jet Region". In the second region, the flow experiences significant deflection due to the impact on the flat wall. The flow direction changes from vertical to parallel to the surface of the wall. This region is called the "Impingement Region". In the third region, the flow demonstrates the properties of a wall jet. Therefore, this region is called the "Wall Jet Region". It is expected to have transition zones between these flow regions.

In the free jet region, turbulence in the nozzle causes jet velocity decay. However, the axial velocity remains undiminished in the form of a core for a certain distance. This core is termed the potential core. For a well-designed nozzle, Beltaos and Rajaratnam (1977) reported that the length of the potential core is within $6.1d$ to $6.3d$. For jet issuing from a simple circular pipe, Hashiehbaf et al. (2015) found that the potential core length is $4d$. For general purposes, Lee and Chu (2003) proposed an average potential core length of $6.2d$. The portion of the jet along the length of the potential core is called the "Near-Field Region". After this region, the remaining part of the free

jet is termed the "Far-Field Region" (Phares et al., 2000).

In the far-field region, the axial velocity of the jet decays with increasing axial distance. As a result, the time-averaged axial velocity profiles of the jet change. However, the shape of the dimensionless axial velocity profiles remains unchanged and independent of the Reynolds number. The mean radial velocity is relatively small compared to the mean axial centerline velocity and can be estimated from the continuity equation with the known axial velocity component. Although the radial velocity is mostly positive, it is negative near the edge of the jet due to the entrainment of ambient fluid (Pope, 2000).

The impingement region begins at an axial distance of about $0.86h$ from the nozzle along the jet axis, and radially it spreads about a radial distance of $0.22h$ from the jet centerline (Beltaos and Rajaratnam, 1974; Ghaneeizad et al., 2015). The impingement height is termed as short impingement height and long impingement height for $h<5.5d$ and $h>8.3d$, respectively. The zone $5.5d{\leq}h{\leq}8.3d$ is transitional. The characteristic parameters of the impingement region include the axial velocity, pressure distribution and shear stress on the wall. According to Rajaratnam et al. (2010), the axial velocity profiles inside the impingement region are similar up to a distance of $0.96h$. The static pressure is greater than the ambient pressure, and the maximum pressure lies along the jet centerline. The pressure profiles are self-similar. The maximum wall shear stress occurs at a radial distance of $0.14h$.

The wall jet region starts at a radial distance of $0.36h$, while the range between $0.22h$ and $0.36h$ is a transition zone (Beltaos and Rajaratnam, 1974). Studies confirmed that the velocity profiles at the wall jet region are self-similar (Poreh et al., 1967).

2.5 Circular Jets in Crossflow

A jet in a crossflow typically refers to a jet issuing into a free-flowing stream at a large angle to the direction of the streamflow (Margason, 1993). This type of jet is also known as transverse jet and is very common in nature and engineering applications. Examples of transverse jets include the launch abort system of space vehicles, effluent discharge into a free stream, cooling of turbine blades, and fuel injection into the crossflow of an oxidizer. This discussion considers a circular jet injected flush into the crossflow of the same fluid. Only the incompressible regime of the jet is

considered.

Let us consider a jet with velocity V_j is issuing at a right angle to a stream flowing freely at a velocity U_t. The stagnation pressure of the ambient stream causes the jet to bend to the direction of flow. Due to turbulent mixing at the outer layer of the jet, this layer easily bends and forms the characteristic kidney shape (Rajaratnam, 1976). The length and location of the end of the potential core depend on the jet velocity to crossflow velocity ratio, R_{jc}. For $R_{jc} > 4$, the endpoint of the potential core stays above the origin of the jet, while for smaller values of R_{jc} the endpoint is pushed downstream. The maximum bending of the jet occurs after the potential core. This zone of maximum bending is known as the zone of maximum deflection. The rest portion of the jet is known as the vortex region. As the jet deviates from its circular shape to form the kidney shape, a counter-rotating vortex pair (CVP) forms in the second region and continues to grow to keep the angular velocity constant. This CVP is responsible for the jet cross-section to change from circular to kidney shape. In the third zone, the CVP keeps growing but starts to lose angular velocity.

The penetration of the jet into the crossflow is described by the jet trajectory. It is known that the jet trajectory is a function of R_{jc} and d, and can be shown by the general form as described in Mahesh (2013)

$$\frac{y}{R_{jc}d} = A\left(\frac{x}{R_{jc}d}\right)^{B} \tag{2.3}$$

where x and y are the coordinates of the jet trajectory in the directions of the crossflow and initial jet flow, respectively; A and B are constants. However, the values of A and B depend on how the trajectory is defined. The trajectory can be defined on the basis of the jet's outer boundary, inner boundary, axis, or centerline of the jet. For R_{jc} from 5 to 35, Pratte and Baines (1967) found $A = 2.63$ and $B = 0.28$ for the outer boundary, $A = 1.35$ and $B = 0.28$ for the inner boundary, $A = 2.05$ and $B = 0.28$ for the centerline of the jet. For R_{jc} from 2 to 10, Margason (1968) found $A = 1.59$ and $B = 0.33$ for the centerline of the jet. A list of values of A and B is provided in Margason (1993) based on previous studies by different researchers, which shows A varied between 1.2 to 2.6, while B varied between 0.28 to 0.4.

In all cases, the transverse jet is more prone to velocity decay and mixing with the ambient fluid

compared to a free jet (Mahesh, 2013; Margason, 1993). The velocity decay is rapid in the near field and slows in the far field (Smith and Mungal, 1998). As the injection angle of the issuing jet in crossflow increases from 0 to 90° (oblique to normal to the crossflow), the decay of the jet velocity generally increases (Margason, 1993).

CHAPTER 3. SCOURING OF SAND BEDS BY SHORT IMPINGING CIRCULAR JETS[*]

3.1 Introduction

The scouring of a sand bed by water jets is important as it can lead to the failure of hydraulic structures due to the scouring often occurring downstream of those structures. Several investigators (e.g., Doddiah et al., 1953; Poreh and Hefez, 1967; Westrich and Kobus, 1973; Aderibigbe and Rajaratnam, 1996; Mazurek et al., 2001; Ansari et al., 2003; Mazurek and Hossain, 2007) have tried to understand the dynamics of scouring with impinging jets in both cohesive and cohesionless soil beds in the laboratory and field environments. The impinging jet was used because the interaction of the jet with the soil bed can be correlated with the resistance of the soil to erosion, namely the critical shear stress with the erosive capacity of water. Scouring in a cohesionless soil bed is particularly of interest because many of the natural stream beds are mainly composed of sand, and sand beds are more vulnerable to scouring than clay beds due to the lower resistance to erosion.

Although studies of erosion involving jet impingement have considered mostly circular, plane, and wall jets with vertical, oblique, and parallel arrangements (e.g., Adduce and La Rocca, 2006; Adduce and Sciortino, 2006; Guan et al., 2016; Si et al., 2018 and 2019), the impingement of submerged circular and vertical jets is the most convenient as it can be operated in the field as well as in the laboratory environments, and the flow is easy to maintain with either a constant head tank or a pump. However, based on the impingement height in terms of the jet diameter, the experiments of impinging jet scouring can be broadly classified as either short or long impingement height. According to Beltaos and Rajaratnam (1977), the impingement height h of a submerged circular turbulent jet can be considered short if $h < 5.5d$, where d is the jet nozzle diameter, and long for $h > 8.3d$. The range $5.5d \leq h \leq 8.3d$ is considered as the transition region.

---

[*] The content of this chapter has been published as: Amin, M. R., Rajaratnam, N., & Zhu, D. Z. (2021). Scouring of sand beds by short impinging turbulent jets. Proceedings of the Institution of Civil Engineers – Water Management, 174(6), 309-320. https://doi.org/10.1680/jwama.20.00109

Most of the previous studies were performed mainly for the long impingement height. Although a few studies have referred to short impingement heights (e.g., Rajaratnam and Beltaos, 1977; Aderibigbe and Rajaratnam, 1996), these studies suffer from inadequate experimental data. For a submerged free jet, the maximum centerline velocity of the jet at any axial distance less than $6.3d$ is still the same as the velocity at the nozzle (Rajaratnam, 1976). Therefore, the short impinging jet possesses more erosive capacity than the long impinging jet having the same jet exit velocity. Further, the scouring mechanism is different due to a different velocity profile of the jet at the impingement region compared to a fully developed jet. Nevertheless, scouring by a short impinging jet closely represents many practical scouring phenomena, such as the cratering of the soil bed by the subsonic jet below a spacecraft (Haehenl et al., 2006), underwater jet trenching for pipe or cable laying operations (Zhang et al., 2017), fluidization of the channel bed with a jet for dredging purposes (Sullivan, 2000) and harvesting clams (Manning, 1960), and cleaning of sewers with high-pressure jets (Calomino et al., 2007).

Another important aspect of scouring of sand beds with a vertically impinging jet is the dynamic depth of scour. As the jet scours the bed, bed particles are thrown outside the scour hole forming a "ridge" around the scour hole. During the process of scouring, the jet forms a toroidal vortex inside the scour hole. While this vortex throws bed particles outside the scour hole, a portion of the bed particles remains in suspension, being trapped inside the vortex. When the jet is stopped, these particles settle inside the scour hole. Consequently, the depth of the scour hole when the jet is stopped, known as the static scour depth, is smaller than the depth when the jet is running, known as the dynamic scour depth. Most of the previous studies only measured the static scour depth because it is rather difficult to obtain the dynamic scour depth precisely. Although a few studies (Aderibigbe and Rajaratnam, 1996; Rajaratnam and Mazurek, 2003; Chakravarti et al., 2014) reported the dynamic scour depth for the asymptotic state of the scour experiments (when the growth of scour depth with time is very small), the temporal development of the dynamic scour depth has been overlooked. Between the static and dynamic scour depths, the latter is apparently more important. This is because the The failure of hydraulic structures due to the scouring below the foundation is possibly associated with the dynamic scour depth rather than the static scour depth. Besides, the dynamic scour depth could be as large as three times the static scour depth (Rajaratnam and Mazurek, 2003; Chakravarti et al., 2014). Therefore, overlooking the dynamic

scour depth during the design stage can be catastrophic.

The scouring of sand bed with short impinging vertical circular turbulent jets and the corresponding dynamic scour depth are of engineering concern. This study presents experimental results that allow for a fair insight into these scouring phenomena. The salient features of the scour hole, such as the characteristic lengths at the unsteady and asymptotic states are assessed and representative expressions are developed. The scour hole profiles are evaluated for similarity and a general expression for the scour hole is developed.

3.2 Theoretical Approach

Following the approach of Aderibigbe and Rajaratnam (1996), the expression for the asymptotic scour hole depth can be derived by combining the maximum bed shear stress with Shields' relation for cohesionless soil in impending motion. The maximum bed shear stress, τ_m, for a fully developed axisymmetric vertical impinging jet is given by Beltaos and Rajaratnam (1974)

$$\tau_m = 0.16 \frac{\rho V_j^2}{(x/d)^2} \tag{3.1}$$

where V_j is jet velocity at the nozzle, x the distance of the bed from the nozzle along the jet axis, and ρ the density of the jet fluid. Although the present study is for short impinging jets, the height of the jet nozzle from the bottom of the scour hole at the asymptotic state is quite long. Therefore, the jet can be approximated as a fully developed jet.

From Shields' relation for a cohesionless soil bed, the Shields parameter is defined as

$$\theta = \frac{\tau_m}{\Delta \rho g D_{50}} \tag{3.2}$$

where θ is Shields parameter, g the gravity acceleration, D_{50} the mean size of the sand particles, and $\Delta \rho$ the density difference between the sand particle and the eroding fluid. For the asymptotic scour hole, critical shear stress condition exists at the bottom of the scour hole. Therefore, combining the maximum shear stress and Shields' relation for critical shear stress condition (Equations 3.1 and 3.2) gives

$$\frac{x'}{d} = \frac{0.4}{\sqrt{\theta}} \left(\frac{V_j}{\sqrt{(\Delta\rho/\rho)gD_{50}}} \right)$$

(3.3)

where x' the value of x for critical shear stress condition. Shields parameter θ is constant for the same sand-water phase for the impending motion of the sand particles. Therefore, for critical shear stress condition, Equation 3.3 can be re-written as

$$\frac{x'}{L} = C_1 E_c$$

(3.4)

where $E_c = V_j(d/L)/[(\Delta\rho/\rho)gD_{50}]^{1/2}$ the erosion parameter proposed by Rajaratnam and Beltaos (1977), L a characteristic length for the scouring process, and $C_1 = 0.4/(\theta)^{1/2}$ a constant. Considering the scour depth along the jet centerline, one can write $x' = nL+\varepsilon_{m\infty}$, where n is a coefficient, and $\varepsilon_{m\infty}$ is the maximum static scour hole depth at the asymptotic condition. While H is the impinging height of the jet, nL gives the effective impinging height. Further, Aderibigbe and Rajaratnam (1996) assumed that C_1 is a function of E_c. Therefore, Equation 3.4 becomes

$$\frac{\varepsilon_{m\infty}}{L} = C_2 E_c{}^m - n$$

(3.5)

where C_2 and m are constants. Aderibigbe and Rajaratnam (1996) adopted the characteristic length $L \approx h$, and $x' = h+\varepsilon_{m\infty}$, which resulted in $n=1$. They combined data of Clarke (1962), Westrich and Kobus (1973), Rajaratnam (1982), and their own experiments, obtaining $C_2 = 1.26$ and $m = 0.11$. Ansari et al. (2003) added data from Sarma (1967) along with their own experiments and found $C_2 = 1.3$ and $m = 0.15$. However, all these experimental data came from long impinging jet experiments. Haehnel et al. (2006) assumed $L=h+d$, to prevent $E_c \rightarrow \infty$ for short impinging jets as $H \rightarrow 0$. This makes sense since according to Beltaos and Rajaratnam (1974), d becomes more important as a scale than h as the impinging height gets smaller. Therefore, Equation 3.5 can be re-written as

$$\frac{\varepsilon_{m\infty}}{h+d} = C_2 E_c{}^m - n$$

(3.6)

Equation 3.6 is the general equation for the asymptotic scour hole depth for cohesionless soil scouring with axisymmetric jets of any impinging heights. The applicability of this equation is

assessed using previous studies and new experimental data.

3.3 Experimental Setup and Experiments

Twelve experiments in total were conducted with two sand sizes, three impinging heights, and two jet velocities to evaluate the effects of these parameters (see Table 3.1). Altogether, these parameters produced different values of the erosion parameters, except for the experiments with zero impinging height. These experiments were carried out for sand of mean sizes $D_{50} = 0.54$ mm and 1.10 mm, so that they represented fine and coarse sand, respectively. Their uniformity coefficient were $C_u = 1.66$ and 2.02, respectively. The coefficient of curvature were $C_c = 1.00$ and 0.59, respectively. These parameters indicate that the sand particles were quite uniform. Specific gravity for both sands was 2.65. Jet velocities at the nozzle $V_j = 2.12$ and 2.61 m/s were selected to produce a reasonable amount of scouring for both types of sands.

However, the range of velocities was dictated by the experimental setup. The jet Reynolds number, $Re = V_j d / \nu$, where ν is the kinematic viscosity of water, for the two water velocities were 26,483 and 32,595, respectively, indicating turbulent jets. Three impinging heights of $h = 0$, $2d$, and $4d$ were used in the experiments to ensure short impinging jets. The experiments are named using the code: sand type (1: $D_{50} = 0.54$ mm, 2: $D_{50} = 1.1$ mm)-nozzle velocity (S: $V_j = 2.12$ m/s, B: $V_j = 2.61$ m/s)-relative impinging depth ($h/d = 0$, 2, or 4). For example, the experiment with 0.54 mm sand, 2.12 m/s nozzle velocity, and 0 relative impinging height is named as 1-S-0.

The experiments were performed inside an octagonal plexiglass tank, 578 mm wide and 610 mm deep (see Figure 3.1a). The jet tank was placed inside a 1000 mm diameter cylindrical overflow tank and was filled with sand up to a depth of 300 mm. A well-designed circular nozzle of 12.5 mm diameter was attached at the end of a 120 mm diameter pipe jet plenum placed vertically at the center of the jet tank. Pipes of lengths of either 330 mm or 385 mm were used for the jet plenum to create small or big velocities at the jet nozzle, respectively. An overflow cup was placed at the upper end of the jet plenum. The jet plenum assembly could be moved vertically or horizontally using a traverse system.

At the test start, the sand bed was level, and the jet tank was slowly filled with water. A submersible pump was used to recirculate water between the overflow tank and jet tank through the jet plenum,

producing an impinging jet onto the sand bed. The nozzle was kept under water inside the jet tank so that the jet was submerged. The nozzle flow rate was measured from the effective water head at the nozzle using Bernoulli's principle. This flow rate was verified by direct measurement of the inflow and outflow at the jet plenum using a magnetic flow meter and volumetric measurement, respectively. The static and dynamic scour hole depths were measured at intervals of 1 min, 2 min, 5 min, 10 min, 20 min, 30 min, 1 hr, 2 hr, 3 hr, and 24 hr. The static depth measurement was accomplished using an offset point gauge with an accuracy of ± 0.1 mm. The jet flow was stopped for this measurement for the suspended particles to settle.

The dynamic scour depth was measured along the jet centerline while the jet was running, using a 1 m long and 2 mm diameter depth rod placed inside a 0.5 m long and 3 mm diameter pipe (see Figure 3.1a). This pipe was placed inside the center of the jet plenum, well above the jet nozzle so that it would not interfere with the jet flow. The depth rod inside this pipe was held by a retaining clip. A vertical scale showed the position of the upper end of the depth rod. At the measurement time, the depth rod was simply dropped inside the scour hole by removing the retaining clip. The position of the depth rod was recorded, and the difference between this measurement and the initial uneroded bed surface measurement gave the dynamic depth. Once the dynamic depth was measured, the depth rod was quickly moved up and clamped in its resting position. The accuracy of this measurement was ± 1 mm.

The definition sketch (Figure 3.1b) shows the characteristic lengths of a typical scour hole, where ε is the scour hole depth at radial distance r from the jet centerline, ε_m and ε_{md} are the static and dynamic scour hole depths, respectively, along the jet centerline. Further, r_0 is the radius of the scour hole, defined as the distance from the jet centerline to the apex of the ridge, and b is the half-radius of the scour hole, defined as $b = r$ when $\varepsilon = \varepsilon_m/2$. The ridge height is represented by δ. The characteristics lengths for the asymptotic scour holes are written with a subscript ∞, i.e., $\varepsilon_{m\infty}$, $\varepsilon_{md\infty}$, $r_{0\infty}$, b_∞, and δ_∞.

3.4 Experimental Results

For the description of the scour hole geometry, Exp. 1-B-4 is considered here. The static scour hole profiles at different times show approximately linear side slopes, representing two distinct

zones inside the scour hole (Figure 3.2a). The slope near the jet impingement point is steeper, and near the periphery is milder. The steeper slope near the scour hole center represents the "active scour zone", where the toroidal vortex is active. The milder slope represents the "passive scour zone", where the sand particles continuously move down the slope inside the scour hole and get trapped in the toroidal vortex. The side slope of the scour hole in the passive scour zone represents the submerged angle of repose of the sand particles.

A closer look inside the static scour hole reveals that near the center of the scour hole the sand particles are bigger. This is because the smaller sand particles are thrown out of the scour hole by the vortex, while the bigger particles remain inside the vortex due to more weight. Therefore, a mechanical sorting of sand particles occurs due to the vortex action. A similar phenomenon was observed by Mih and Kabir (1983) for a vertical circular jet impingement on a gravel bed. When the jet is stopped, the particles inside the vortex settle down forming the steeper slope in the active scour zone. The angles of inclination in the two scour zones are due to the difference in the sand particle size mechanically sorted by the vortex. The side slopes of the scour hole in Exp. 1-B-4 in the active and passive scour zones are approximately 43° and 25.5°, respectively.

Another interesting observation relates to the temporal development of the ridge. The apex of the ridge at different times stays at a constant virtual slope to the original bed surface. The angle of this virtual slope is approximately 8°. Rouse (1939) also observed a similar slope of the ridge apex for the impingement of vertical plane wall jet on the sand bed.

Since the side slope of the scour hole in the passive scour zone represents the submerged angle of repose, irrespective of the experimental conditions, the side slopes for the same sand bed in different experimental conditions should be identical. To verify this, the asymptotic profiles of the static scour holes for different experiments are compared in Figure 3.2b. This figure shows that the side slopes are the same with slight variations between the experiments with 0.54 mm and 1.1 mm sands. These variations are due to the different submerged angle of repose of these sands (Haehnel et al., 2006). Indeed, Figure 3.2b provides further insight into the scouring process. In general, the asymptotic profiles show that the size of the scour hole increases with the impingement height. This is because for the short impingement height jet scour experiments, as the nozzle comes closer to the original uneroded bed surface, the jet is strongly deflected by the return flow. Further,

considering the jet spreading, the impingement area reduces with reducing impingement height, while the centreline jet velocity is still the same as the nozzle. Therefore, the eroding capacity of the jet in terms of the static scour reduces as the impingement height decreases.

The development of the characteristic lengths of the scour hole of different experiments shows that the dynamic scour hole depth reaches the asymptotic state earlier than the static scour hole depth (Figure 3.3). It happens because the dynamic scour depth is the result of the direct interaction of the impinging jet and the sand bed, while the static scour depth depends on the removal of the sand particles trapped in the vortex inside the active scour zone. The rate of the removal of sand particles from the scour hole becomes slower with time. Thus, it takes longer for the static scour depth to reach the asymptotic state. Further, instead of continuous growth, the dynamic scour depth fluctuates with time. This is reasonable since the bed under the jet influence is a moving bed. Considering the other characteristic lengths shown in Figure 3.3, ε_m, r_0, and b are seen to grow with time. Since ε_m shows continuous growth with time, it is a good candidate for the assessment of the time development of the scour hole. However, δ seems to reach the asymptotic state early in some of the experiments for $D_{50} = 1.1$ mm.

Table 3.2 shows the characteristic lengths of the asymptotic scour hole for different experiments. Considering all the experiments, the minimum dynamic scour depth is found as 106 mm or $8.5d$, which indicates that the approximation of a fully developed jet inside the scour hole for Equation 3.1 is reasonable. A quantitative comparison of the dynamic and static scour depths in terms of the ratios $\varepsilon_{md\infty}/\varepsilon_{m\infty}$ varies between 2.1 to 4.3. For a circular impinging jet on a sand bed with long impingement height and small tailwater, Rajaratnam and Mazurek (2003) obtained $\varepsilon_{md\infty}/\varepsilon_\infty \approx 3$. For a gravel bed and a submerged circular impinging jet of long impinging height, Chakravarti et al. (2014) found $\varepsilon_{md\infty}/\varepsilon_{m\infty} \approx 1.6\text{-}3.6$. Despite different experimental conditions, $\varepsilon_{md\infty}/\varepsilon_{m\infty}$ values for this study are comparable to the previous. The values $r_{0\infty}/b_\infty$ for all the experiments ranged between 3.1 and 4.7, while $r_{0\infty}/\varepsilon_{m\infty}$ between 2.1 and 2.9. The dimensionless ridge heights $\delta_\infty/\varepsilon_{m\infty}$ are between 0.23 and 0.42 for all the experiments.

3.5 Analysis and Discussion

3.5.1 Characteristic Lengths in Asymptotic State

Asymptotic static scour depth data from Rajaratnam (1982), Aderibigbe and Rajaratnam (1996), Ansari (2003), and this study are plotted in Figure 3.4a. All of these studies except the present one involve scouring with long impinging jets. Figure 3.4a shows that the data is separated into two groups. For $E_c \leq 1.35$, the asymptotic static scour depth can be represented by a power function of E_c. For $1.35 < E_c < 28$, $\varepsilon_{m\infty}$ linearly varies with E_c. The evolution of the jet flow dynamics inside the scour hole with the jet impinging height is responsible for this separation. Rouse (1939) observed two different jet regimes in scouring with plane vertical jets. He termed those regimes as "maximum jet deflection", and "minimum jet deflection" where the jet turns nearly 180º, and where it follows the boundary of the scour hole, respectively. Similarly, Westrich and Kobus (1973) classified the flow regimes into "scour form I" and "scour form II" based on the interaction of the jet with the scour hole. Aderibigbe and Rajaratnam (1996) classified the flow regimes as either the "strongly deflected jet regime" or the "weakly deflected jet regime". Nonetheless, at least two different flow regimes exist in the souring of cohesionless bed with impinging jets. The effect of these flow regimes is significant for the characteristic scour depths since this controls how the sand particles are trapped in the toroidal vortex and remain in suspended motion. A fraction of these particles deposits along the ridge with time, and the rest settles inside the scour hole as the jet ceases.

Regression analysis of the data in Figure 3.4a gives the equation for asymptotic static scour depth (Equation 3.7).

$$\frac{\varepsilon_{m\infty}}{h+d} = 1.30 E_c^{0.14} - 1 \qquad \text{for } E_c \leq 1.35 \,; (R^2 = 0.83)$$

$$(3.7)$$

$$\frac{\varepsilon_{m\infty}}{h+d} = 0.14 E_c + 0.15 \qquad \text{for } 1.35 < E_c < 28 \,; (R^2 = 0.97)$$

Figure 3.4(b) shows that the asymptotic dynamic scour depths can be represented by a single equation, irrespective of the jet impingement regime. This indicates that although the jet impingement height affects the dynamics of sand particle transport from the scour hole, it does not impact the fluidization of the sand bed significantly. Regression analysis shows that a linear

function of E_c fits the datasets satisfactorily (Equation 3.8).

$$\frac{\varepsilon_{md\infty}}{h+d} = 0.49E_c - 0.06 \; ; (R^2 = 0.98) \tag{3.8}$$

Other characteristic lengths of the scour hole, such as $r_{0\infty}$, b_∞, and δ_∞ are plotted against E_c in Figures 4c, d, and e, respectively. Similar to the plot of $\varepsilon_{m\infty}$, data separation is observed at $E_c = 1.35$. Regression analysis shows a power function of E_c for $E_c \leq 1.35$, and a linear function of E_c for $1.35 < E_c < 28$ can describe these characteristic lengths satisfactorily. These relations are described in Equations 3.9 to 3.11.

$$\frac{r_{0\infty}}{h+d} = 1.55E_c^{0.15} - 1 \quad \text{for } E_c \leq 1.35 \; ; (R^2 = 0.87)$$

$$\tag{3.9}$$

$$\frac{r_{0\infty}}{h+d} = 0.39E_c + 0.02 \quad \text{for } 1.35 < E_c < 28 \; ; (R^2 = 0.95)$$

$$\frac{b_\infty}{h+d} = 1.20E_c^{0.06} - 1 \quad \text{for } E_c \leq 1.35 \; ; (R^2 = 0.83)$$

$$\tag{3.10}$$

$$\frac{b_\infty}{h+d} = 0.12E_c - 0.06 \quad \text{for } 1.35 < E_c < 28 \; ; (R^2 = 0.93)$$

$$\frac{\delta_\infty}{h+d} = 1.08E_c^{0.04} - 1 \quad \text{for } E_c \leq 1.35 \; ; (R^2 = 0.87)$$

$$\tag{3.11}$$

$$\frac{\delta_\infty}{h+d} = 0.05E_c - 0.03 \quad \text{for } 1.35 < E_c < 28 \; ; (R^2 = 0.90)$$

Some scattering of the data is observed in the plot of δ_∞ (Figure 3.4e) for $E_c = 0.7$-1.35. Aderibigbe and Rajaratnam (1996) explained this in terms of their experimental setup. In their experiments, the impinging height and the water depth above the original bed level were about the same, so that the jet was just submerged. It resulted in a strong radial flow for lower impingement height, which contributed to a lower ridge height.

3.5.2 Temporal Development of the Characteristic Lengths

To investigate the temporal development of the maximum scour hole depth (ε_m), one needs to find the appropriate length and time scales to obtain a dimensionless relation. Rajaratnam and Beltaos (1977) used the maximum asymptotic static scour depth ($\varepsilon_{m\infty}$) as the length scale, and t_* as the time scale, which is the time in ε_m versus $\log t$ plot where ε_m starts to deviate from the initial linear trend with time t. They also used another time scale t_+, such as $t = t_+$, when $\varepsilon_m = \frac{1}{2}\,\varepsilon_{m\infty}$. Ansari et al. (2003) adapted a sine function to describe the time development of ε_m, where $\varepsilon_{m\infty}$ and t_∞ were used as the length and time scales, respectively, and t_∞ was the time to reach the asymptotic scour depth. However, for short impinging jet experiments with comparatively higher values of E_c, it is difficult to obtain t_*, t_+, or t_∞ with confidence because the scour depth reaches to the asymptotic state rapidly. Therefore, asymptotic lengths ($\varepsilon_{md\infty}$, $\varepsilon_{m\infty}$, $r_{0\infty}$, and δ_∞) are used as the length scale and h/V_j as the time scale.

Figure 3.5 shows the temporal development of the dimensionless characteristic lengths. The static depth and radius show a good correlation with $R^2 = 0.74$ and 0.80, respectively. However, for the dynamic depth and ridge height, the correlation is poor, with $R^2 = 0.28$ and 0.41, respectively. This is because these two lengths reach the asymptotic state quickly, and not in a predictable manner. Therefore, the temporal development relations are appropriate for the static scour depth and radius of the scour hole only and given by

$$\frac{\varepsilon_m}{\varepsilon_{m\infty}} = 0.03 \ln\left(\frac{tV_j}{h}\right) + 0.58 \; ; (R^2 = 0.74) \tag{3.12}$$

$$\frac{r_0}{r_{0\infty}} = 0.04 \ln\left(\frac{tV_j}{h}\right) + 0.35 \; ; (R^2 = 0.80) \tag{3.13}$$

3.5.3 Similarity in the Scour Hole Profiles

In previous studies with long impinging jets, the similarity in the scour hole profiles was observed. In this short impinging jet scouring study, this similarity has been investigated for the development of the scour hole with time, and for the asymptotic scour hole. The dimensionless profiles are obtained using ε_m as the scale for ε, and r_0 as the scale for r. The conventional approach of using b as the scale for r is also used to verify which scale provides a better result in finding the similarity of profiles.

23

Figure 3.6 provides the dimensionless profiles for different times of Exp. 1-B-4. Dimensionless asymptotic scour hole profiles for all the experiments are shown in Figure 3.7. These show that r0 works better as a scale for radial distance. One reason for this is the way r_0 is defined. Since r_0 is defined up to the crest of the ridge, it works better to scale the entire profile, whereas, b is defined as $b = r$ when $\varepsilon = \varepsilon_m/2$. Therefore, b only describes the inner part of the scour hole well. Further, it is easy to accurately identify the crest of the ridge during measurement, whereas b is rather estimated from the measured profiles by interpolation.

Figure 3.7a shows the data for the dimensionless asymptotic scour hole profiles of this study along with the curve provided by Aderibigbe and Rajaratnam (1996) as a general profile for asymptotic scour hole. Due to the previously described reason, b is not performing well as a scale for the radial distances. The curve fit provided by Aderibigbe and Rajaratnam (1996) is indeed a Gaussian curve assuming a Gaussian scour hole profile, and based on long impinging jet experiments. However, for short impinging jets, the side slope of the scour hole is almost linear, corresponding to the submerged angle of repose of the bed material. Therefore, it is necessary to develop a general equation of the asymptotic scour hole for the short impinging jet experiments using $\varepsilon_{m\infty}$ and $r_{0\infty}$ as the length scales.

Figure 3.7b shows the dimensionless asymptotic scour hole profiles using $\varepsilon_{m\infty}$ and $r_{0\infty}$ as the length scales. It is observed that $r_{0\infty}$ provides less scatter than b_∞ as the length scale. Except for the dynamic scour zone, experiments with different sands show different slopes due to the different submerged angle of repose of the sand particles. A general curve is proposed in Figure 3.8 based on the dimensionless asymptotic scour hole data where O is the origin of the coordinate system in the plot. Line AB represents the slope for the dynamic scour zone, which is assumed constant, equal to 2 vertical to 1 horizontal. This agrees with the experimental data. The slope of the line BC is a function of the submerged angle of repose, α_r, of the sand particle. Therefore, the angle at point B, α' is a function of α_r. Line CE is the dimensionless length $\delta_\infty/\varepsilon_{m\infty}$. Now, since the coordinates of A, B, C, and D are known, the equations of the lines AB, BC, and CD can be written as follows

$$
\frac{\varepsilon}{\varepsilon_{m\infty}} =
\begin{cases}
2\left(\dfrac{r}{r_{0\infty}}\right) - 1, & \text{for line AB} \\[2mm]
\tan \alpha' \left(\dfrac{r}{r_{0\infty}} - 1\right) + \dfrac{\delta}{\varepsilon_{m\infty}}, & \text{for line BC} \\[2mm]
-\tan \alpha' \left(\dfrac{r}{r_{0\infty}} - 1\right) + \dfrac{\delta}{\varepsilon_{m\infty}}, & \text{for line CD}
\end{cases}
\tag{3.14}
$$

where $\tan \alpha'$ is a function of the angle of repose α_r. Therefore, $\tan \alpha'$ can be expressed in terms of α_r, using the geometry of Figure 3.8 as

$$
\tan \alpha' = \left(\frac{r_{0\infty}}{\varepsilon_{m\infty}}\right) \tan \alpha_r
\tag{3.15}
$$

Experimental data show that the mean value of $r_{0\infty}/\varepsilon_{m\infty}$ and $\delta_\infty/\varepsilon_{m\infty}$ are 2.6 and 0.34, respectively. Therefore, the final form of the general equation for the dimensionless scour hole profile is given by

$$
\frac{\varepsilon}{\varepsilon_{m\infty}} =
\begin{cases}
2\left(\dfrac{r}{r_{0\infty}}\right) - 1, & \text{for line AB} \\[2mm]
2.6 \tan \alpha_r \left(\dfrac{r}{r_{0\infty}} - 1\right) + 0.34, & \text{for line BC} \\[2mm]
-2.6 \tan \alpha_r \left(\dfrac{r}{r_{0\infty}} - 1\right) + 0.34, & \text{for line CD}
\end{cases}
\tag{3.16}
$$

Values of α_r for 0.54 mm and 1.1 mm sands are 25.5° and 30.1°, respectively.

3.6 Summary and Conclusions

The scouring of sand bed is experimentally investigated for vertical jets of short impinging height of 5.5 times the jet diameter. Dynamic depth of scour is measured along with static scour profiles. Experimental results show that the short and long impinging jet scouring experiments are quite different. Some of the important findings include:

- The characteristic lengths at the asymptotic state normalized with the total length of the jet impinging height and diameter are functions of the erosion parameter.
- The dynamic scour depth is larger than the static scour depth and reaches the asymptotic state quickly. The ratio of the dynamic to static scour depths varies between 2.1 to 4.3, for E_c ranges

between 3 to 28.

- The side slopes of the scour hole indicate two distinct scour zones, the active and passive scour zones. The slope at the passive scour zone represents the submerged angle of repose of the sand.
- The dimensionless profiles of the scour hole are similar, considering profiles at different measurement time and at the asymptotic state.

Semi-empirical prediction equations are developed for the characteristic lengths of the scour hole at asymptotic state using experimental data from this study and previous studies, for the erosion parameter varies between 0 to 28, covering both long and short impinging jet regimes. Empirical prediction equations are developed for the temporal development of the static scour depth and radius. A general expression for the dimensionless scour hole profile is developed as a function of the submerged angle of repose of sand. Although the study of scour on sand bed by impinging jets is not novel, this study includes the short impingement regime with bigger erosion parameters (e.g., E_c = 28), and temporal development of dynamic scour. Both of these aspects were not investigated before.

Table 3.1: Details of experiments

Exp. No.	D_{50}	Q	V_j	h	h/d	E_c	Re
	(mm)	(L/s)	(m/s)	(mm)			
1-S-0	0.54	0.26	2.12	0	0	22.7	26483
1-S-2		0.26	2.12	25	2	7.6	26483
1-S-4		0.26	2.12	50	4	4.5	26483
1-B-0		0.32	2.61	0	0	27.9	32595
1-B-2		0.32	2.61	25	2	9.3	32595
1-B-4		0.32	2.61	50	4	5.6	32595
2-S-0	1.1	0.26	2.12	0	0	15.9	26483
2-S-2		0.26	2.12	25	2	5.3	26483
2-S-4		0.26	2.12	50	4	3.2	26483
2-B-0		0.32	2.61	0	0	19.6	32595
2-B-2		0.32	2.61	25	2	6.5	32595
2-B-4		0.32	2.61	50	4	3.9	32595

For all experiments, the jet diameter at the nozzle was $d = 12.5$ mm.

Table 3.2: Characteristic lengths of the scour hole in the asymptotic state

Exp. No.	$\varepsilon_{m\infty}$	$\varepsilon_{md\infty}$	$\varepsilon_{md\infty}/\varepsilon_{m\infty}$	r_{∞}	b_{∞}	r_{∞}/b_{∞}	δ_{∞}	$r_{\infty}/\varepsilon_{m\infty}$	$\delta_{\infty}/\varepsilon_{m\infty}$
	(mm)	(mm)	(-)	(mm)	(mm)	(-)	(mm)	(-)	(-)
1-S-0	44	126	2.86	122	40.0	3.1	17	2.8	0.39
1-S-2	51	106	2.08	119	36.8	3.2	13	2.3	0.25
1-S-4	51.5	110	2.14	116	29.5	3.9	16	2.3	0.31
1-B-0	53	-	-	155	47.8	3.2	22	2.9	0.42
1-B-2	54	157	2.91	149	42.0	3.5	21	2.8	0.39
1-B-4	58	143	2.47	147	46.0	3.2	21	2.5	0.36
2-S-0	25	107	4.28	64	19.3	3.3	8	2.6	0.32
2-S-2	36	115	3.19	94	20.0	4.7	13	2.6	0.36
2-S-4	36	112	3.11	101	22.0	4.6	15	2.8	0.42
2-B-0	30	129	4.30	63	18.0	3.5	7	2.1	0.23
2-B-2	42	112	2.67	103	26.6	3.9	11	2.5	0.26
2-B-4	47	134	2.85	109	26.5	4.1	15	2.3	0.32
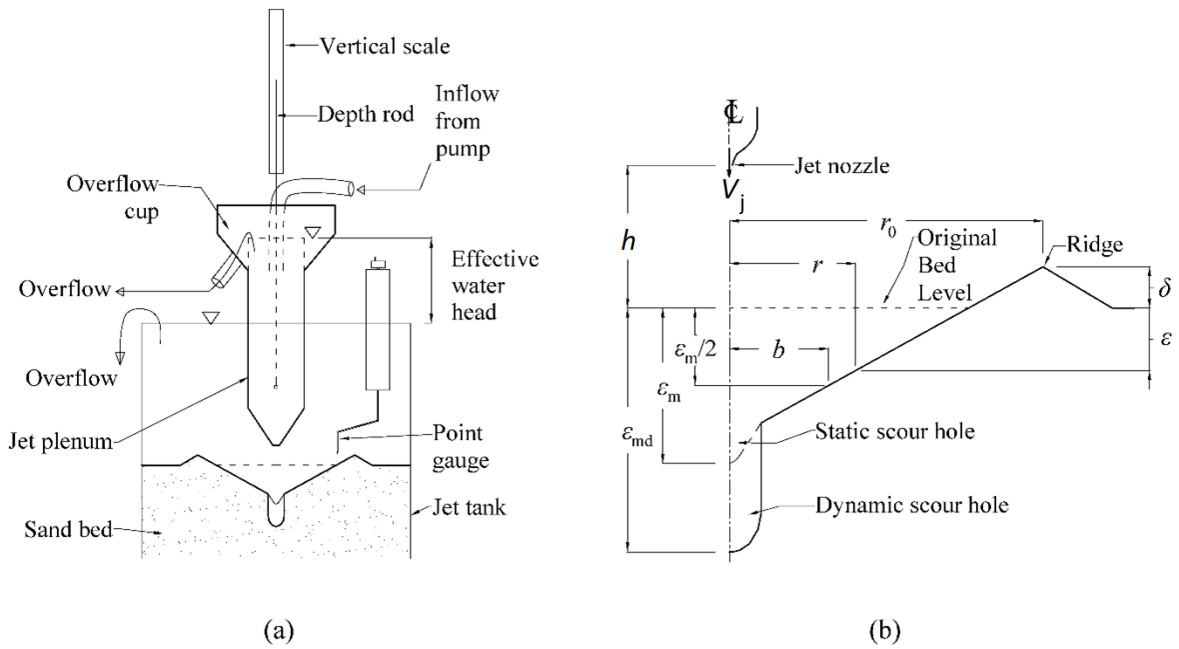
Figure 3.1: Experimental setup for scour testing and dynamic scour depth measurement by short impinging jets: (a) schematic diagram, (b) definition sketch

(a)

(b)
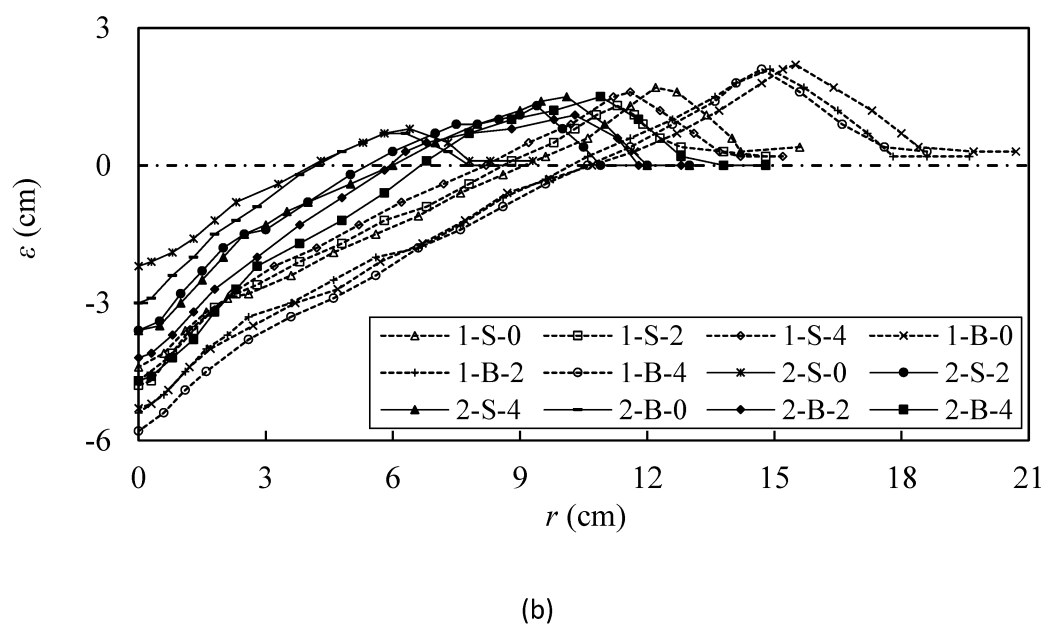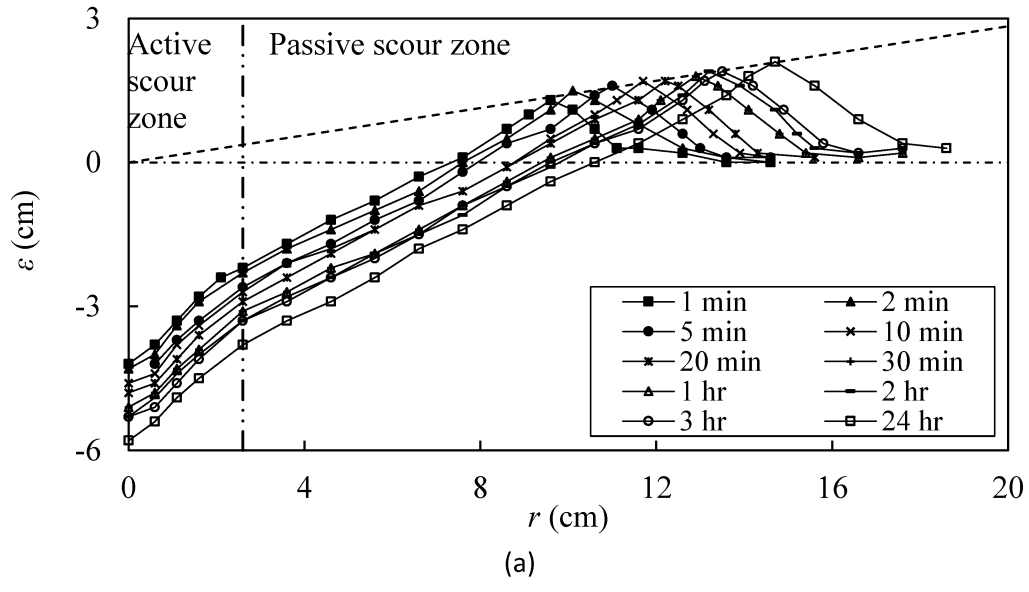
Figure 3.2: Static scour hole profiles (a) Temporal development for Exp. 1-B-4, (b) Asymptotic profiles for different experiments
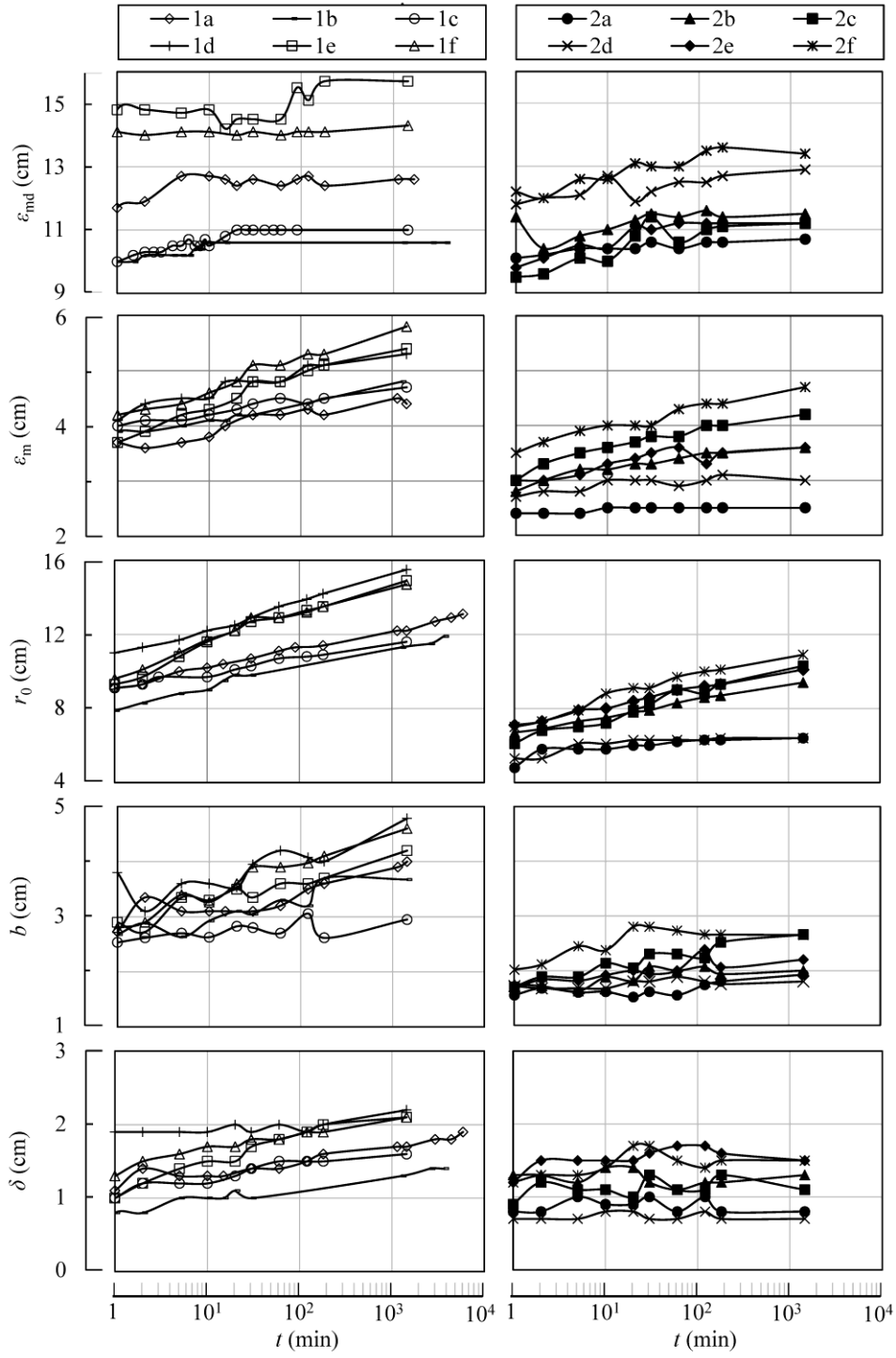
Figure 3.3: Temporal development of the characteristic lengths of the scour hole

31
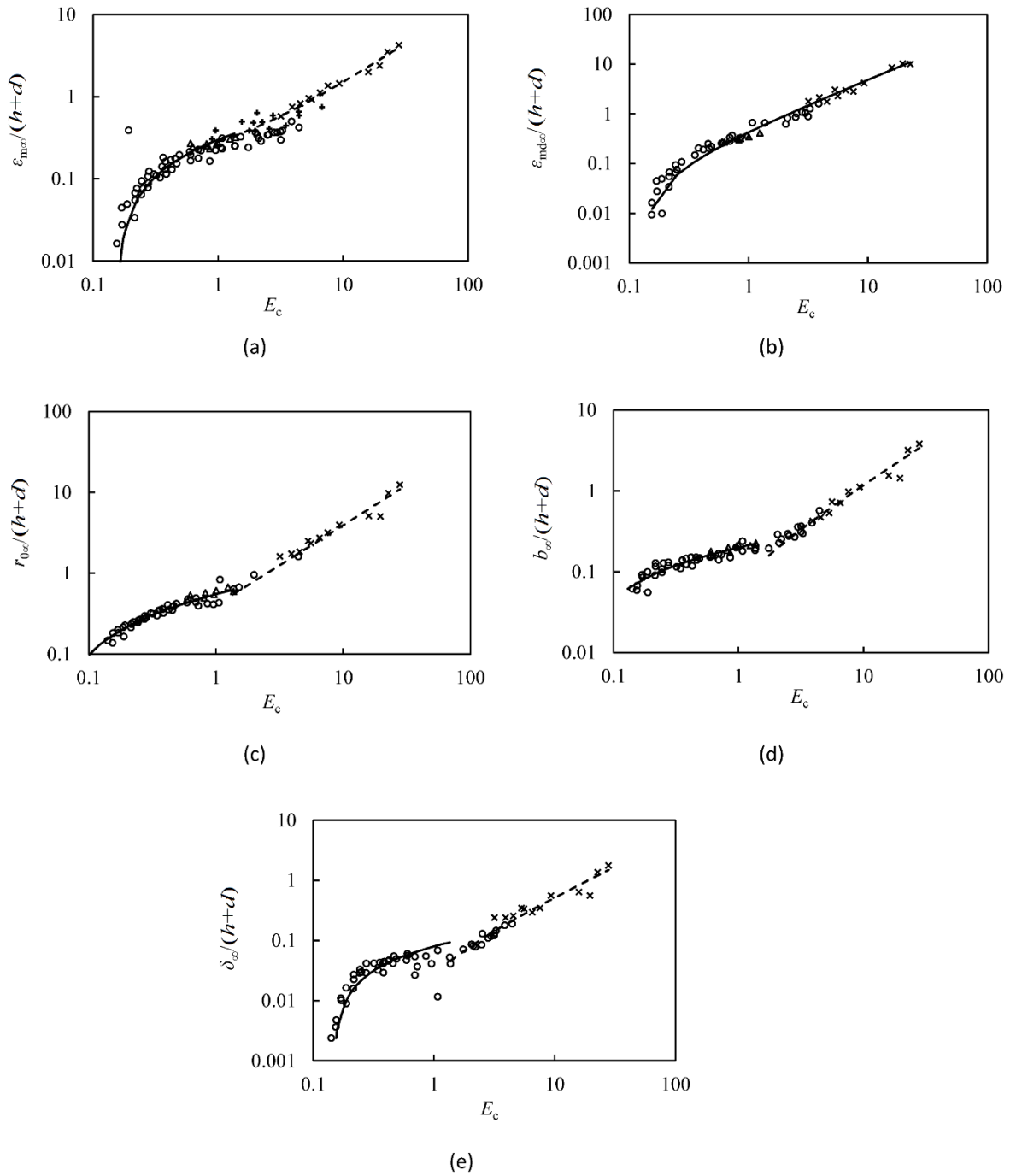
Figure 3.4: Normalized characteristic scour lengths in asymptotic state as a function of the erosion parameter; (a) static scour depth; (b) dynamic scour depth; (c) radius; (d) half-radius; and (e) ridge height. Symbol denotes: (✕) experimental observations, (Δ) Rajaratnam (1982), (○) Aderibigbe and Rajaratnam (1996), (+) Ansari et al. (2003); (−) power function; (- -) linear function
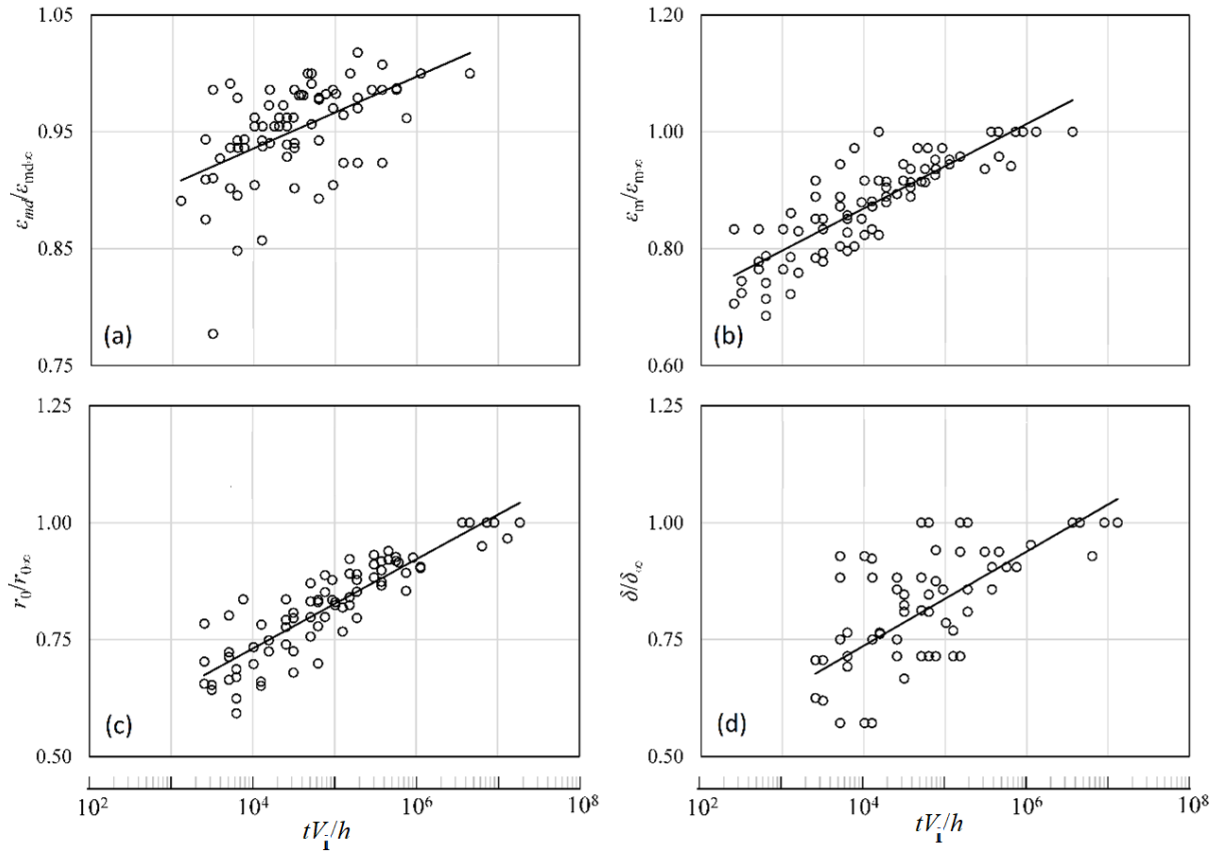
Figure 3.5: Temporal development of the characteristic lengths of the scour hole; (○) experimental observations and (−) best fit lines for (a) $\varepsilon_{md}/\varepsilon_{md\infty}$ vs. tV_j/h; (b) $\varepsilon_m/\varepsilon_{m\infty}$ vs. tV_j/h; (c) $r_0/r_{0\infty}$ vs. tV_j/h; (d) δ/δ_∞ vs. tV_j/h
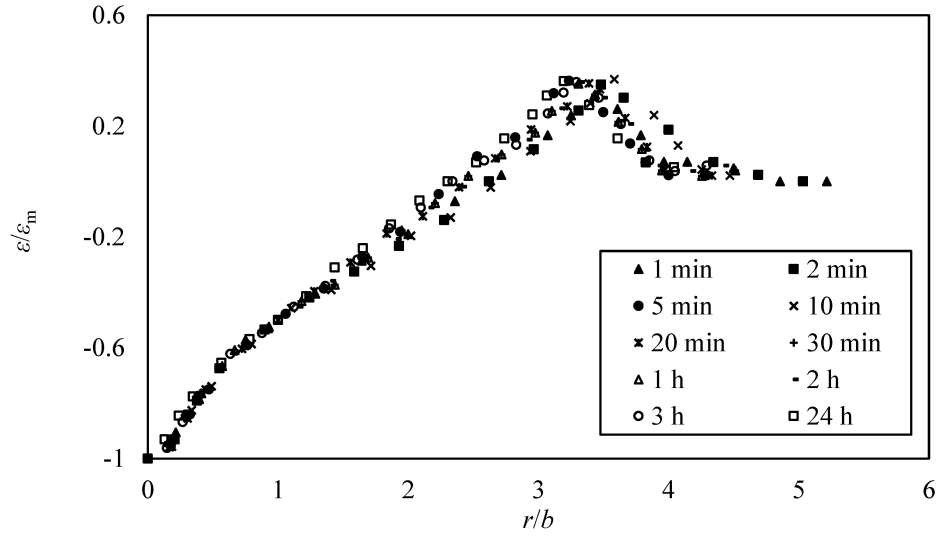
(a)
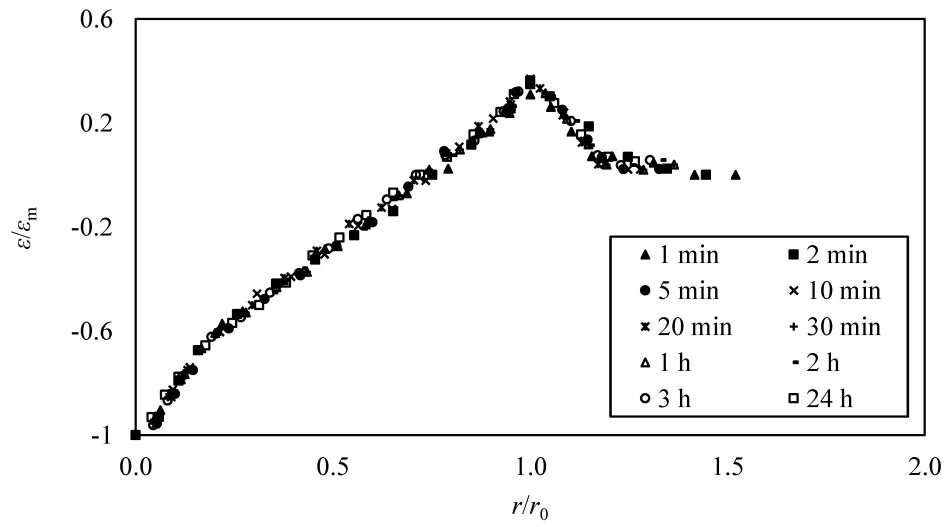
(b)

Figure 3.6: Dimensionless scour hole profiles at different times of Exp. 1-B-4 using (a) ε_m and b, (b) ε_m and r_0 as length scales
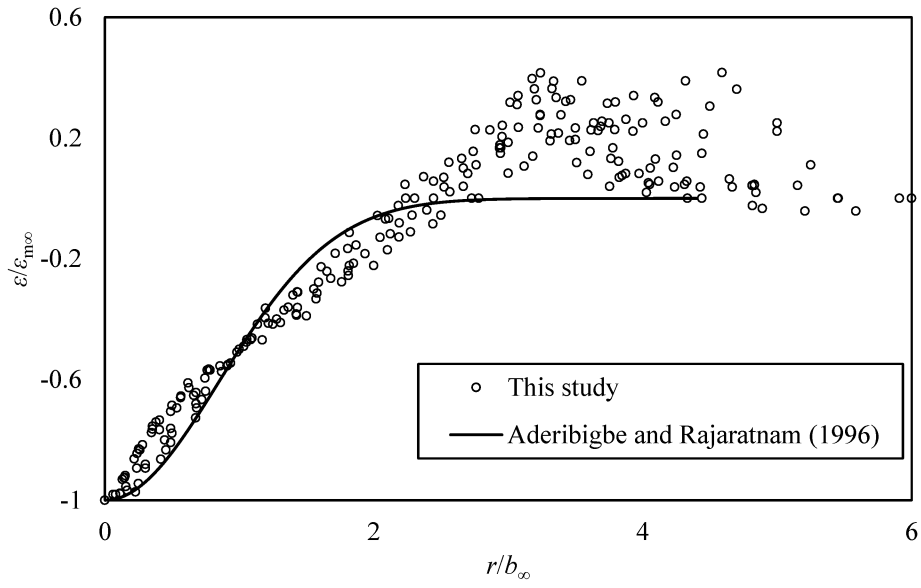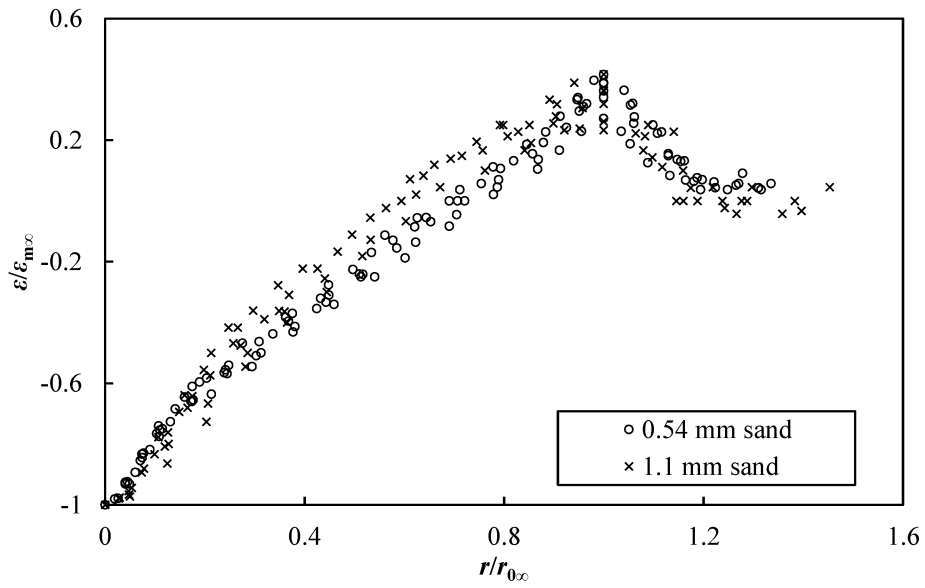
Figure 3.7: Dimensionless asymptotic scour hole profiles for all the experiments using (a) $\varepsilon_{m\infty}$ and b_∞, and (b) $\varepsilon_{m\infty}$ and r_∞ as length scales

Figure 3.8: Schematic diagram of general curve fitting for dimensionless asymptotic scour hole profile for sand bed scouring by short impinging jets

CHAPTER 4. EROSION OF SAND BEDS WITH TRANSLATING CIRCULAR JETS

4.1 Introduction

Scour of cohesionless beds by translating turbulent jets is an important topic because of several engineering applications. These applications include water-jet assisted dredging (Sullivan, 2000), ocean bed fluidization for clam harvesting (Manning, 1959), jet induced trenching to lay submarine cables or pipes (Zhang et al., 2017), removal of dumped rock cover with moving jet (Schoen, 2014), and sewer cleaning with high-pressure jets (Calomino et al., 2007). Further, risks of unintended erosion are associated with translating jets generated in other operations, e.g., cratering below a spacecraft by subsonic jets (Haehnel et al., 2006), and erosion of shallow channel bed due to discharge below a moving vessel (Yeh et al., 2009). Although a number of studies have been conducted on the scouring of cohesive and cohesionless soil by impinging stationary jets (Amin, 2016; Amin, et al., 2021; Ansari et al., 2003; Bombardelli et al., 2018; Bombardelli and Gioia, 2006; Mazurek, 2001), there is a paucity of studies on the scouring by translating jets. This is because the experimental setup for translating jet scour testing is complicated; the dynamics of a translating jet has some analogy with a jet in crossflow, and is not well understood, and the knowledge on the impingement of translating jet is not sufficient.

Understanding scouring by translating jet requires the knowledge of scouring by impinging stationary jets with different impinging heights and inclination angles. A vertically impinging circular jet of diameter d is considered long for $h > 8.3d$, and short for $h < 5.5d$, where h is the impinging height of the jet (Beltaos and Rajaratnam, 1977). Mostly, the previous studies considered scour testing with a long jet so that the impingement of the jet happens in the developed region of the jet. Researchers related the critical shear stress of the bed to the velocity of the jet at the impingement location because the velocity decay for a developed jet is predictable (e.g., Hanson and Cook, 1997). Recently, Amin et al. (2021) conducted experiments with short jets and showed that there are both similarities and differences in scour features for short and long jets. Experiments with short translating jets will be interesting because most of the engineering applications of jets require strong jets, which are typically short impinging jets. Moreover, it is necessary to assess the scour by short translating jets in oblique configurations to compare the

amount and mechanism of scour at different impinging angles.

Another rarely studied aspect of stationary jet scour research on sand bed is the dynamic depth of scour. During the jet scour experiments, a portion of the sand particles remain in suspension due to the vortex created by the impinging jet, and the depth of scour is termed as the dynamic scour depth. When the jet is stopped, these particles settle down inside the scour hole, resulting a smaller depth of scour, namely the static scour depth. Dynamic scour depth is more important because the failure of hydraulic structures is associated with this scour depth. Further, some practical problems, like dredging of waterbody and fluidization of sand bed for clam collection involve dynamic scouring. Despite the importance of dynamic scour depth, only few studies (Rajaratnam and Mazurek, 2003; Amin et al., 2021; Chakravarti et al., 2014) measured this parameter due to the difficulty in measurement when the jet is running. However, studies with stationary jets showed that dynamic depth progresses to the asymptotic depth relatively quickly (Amin et al., 2021), while static depth increases slowly with time. Here, asymptotic depth is characterized by the scour depth at a particular time of scour, after which the growth of scour depth is negligible. Nonetheless, for a translating jet scouring, the dynamic depth is more important as the jet does not stay at the same location for a considerable amount of static scour to occur.

Although a good number of studies have been carried out on scour by stationary jets, only a few studies involved scouring with translating jets. Many of these translating jet scour studies were conducted for clay beds (Gu et al., 2018; Nobel, 2013; Rockwell, 1981; Zhang et al., 2016 and 2017). Since there is a fundamental difference in scour mechanism between cohesive and cohesionless soil (Amin, 2018), it is important to particularly review the moving jet experiments conducted in sand beds in connection to this study. Studies of scour in sand beds with translating jets include scour of sand bed with inclined plane jets (Perng and Capart, 2008), with inclined circular jets (Berghe et al., 2011; Su et al., 2007), with vertical circular jets (Weegenaar et al., 2015; Yeh et al., 2009). A summary of these studies is shown in Table 4.1.

Perng and Capart (2008) used a moving jetting head consisting of a series of circular orifices which formed a plane jet inclined at 60° to the opposite direction of travel, i.e., the angle of inclination of the jet at the direction of the jet translation, α =210°. The translating velocity of the plane jet U_t ranged between 10 to 100 mm/s, while the water velocities at the nozzle V_j were between 8 to 10.9

m/s. They used a medium quartz sand of median diameter, $D_{50} = 0.33$ mm, and assumed that the turbulent current induced by the jet stratified into sediment-laden and sediment-free sublayers, and thus proposed a shallow-flow theory. The sediment-laden sublayer may continue as supercritical flow inside the trench formed by the jet, or may produce an internal hydraulic jump, depending on the translating speed of the jet. However, compared to an axisymmetric jet, the plane jet scouring is a much simpler problem being a 2D case instead of 3D. It will be worth investigating the flow regimes for a circular translating jet with smaller impinging angles ($\alpha \leq 90°$).

Small scale scour experiments were performed by Su et al. (2007) and Berghe et al., (2011) inside a glass-walled tank with needle jets of small internal diameter ($d = 0.6$ mm) and very fine sand beds ($D_{50} = 0.08, 0.17$ mm). In these studies, V_j varied between 6 to 36 m/s and U_t was ranged between 0 to 70 mm/s. The needle jets were inclined ($\alpha = 210°$) and positioned at various vertical locations starting from the sand bed surface to inside the bed. The amount of the bed fluidization was found to depend on V_j and U_t. It was reported that the geometry of the trench scoured by the jet depends on five mechanisms- entrainment, erosion, deposition, breaching, and overspill. A model was proposed based on the gravity and jet-driven turbidity currents theory. The effect of α in the scouring process was absent in these studies, and the scale of the experiments was very small compared to the prototype cases, e.g., the jetting swords for burying submarine cables.

Large scale laboratory experiments of scour of sand bed ($D_{50} = 0.26$ mm) with a translating vertical circular jet ($d = 127$ mm) was conducted by Yeh et al., (2009). The experiments were carried out in a towing tank, with $V_j = 2.05$ m/s and $U_t = 0.09 - 0.51$ m/s. It was found that the maximum static scour depth and ridge height depend on the ratio of the jet nozzle velocity to traveling velocity (V_j/U_t), and the erosion parameter E_c (E_c is defined later in this work). However, this study mostly considered the static features of scour, which are smaller in scale compared to the dynamic ones and thus not very significant for most of the practical purposes.

Weegenaar et al. (2015) studied the fluidization of sand bed ($D_{50} = 0.14$ and 0.28 mm) by a moving vertical circular jet ($d = 5 - 11$ mm, $h = 17$ mm, $V_j = 30 - 40$ m/s, $U_t = 0.25 - 1$ m/s) to assess the performance of jets used in the water-assisted dragheads of dredgers. This study showed that the fluidized sand flux was proportional to the jet momentum flux, and more specific energy was needed to fluidize finer sand than coarser sand. However, the evolution of the dynamic depth, or

the extent of the fluidized zone was not reported.

In general, the previous studies on the scour of sand beds by traveling jets were application specific (Table 4.1). While the study of Yeh et al. (2009) was comprised of large-scale laboratory experiments, the studies by Su et al. (2007), and Berghe et al. (2011) used small-scale physical models of the prototypes. Interestingly, although small-scale, the latter studies used bigger jet velocities. Weegenaar et al. (2015) used the biggest jet nozzle velocities of all the experiments discussed. The maximum scour depth measured in the studies of Su et al. (2007), Berghe et al. (2011), and Weegenaar et al. (2015) was dynamic scour depth. For the dynamic depth measurement, the concept of the wall of symmetry was used so that the fluidized zone could be captured with a camera. Since the practical applications demand a strong impinging jet, the impinging heights in these studies were quite small. Further, the ratio of the jet nozzle velocity to the jet traveling velocity was quite large in all the studies except Yeh et al. (2009).

It should be noted that in the studies where inclined jets were used, the large inclination angle (210°) allowed the jet to continue to fluidize the bed along the direction of horizontal jet travel, while the sands settle down and filled up the scoured trench upstream of the jet. This technique is particularly useful for laying of submarine pipelines where downstream scouring of trench and upstream burying of pipes occur at the same time. On the contrary, with vertically impinging traveling jets, the depth of the upstream trench could be significant even after the settlement of some sand particles. Translating jet experiments with oblique impingement to the direction of travel would be particularly interesting, as the scouring mechanism could be different and could be useful for many applications. For examples, in cleaning in storm sewer system, traveling jets with oblique impingement to the direction of travel could be beneficial. However, this will need to be confirmed by laboratory experiments with traveling jets of different impinging angles.

The present study involves laboratory investigation of scour in cohesionless beds with circular translating jets at different impinging angles. The features of the static and fluidized zone are discussed along with a comparison with stationary jet results. The kinematics of the sediment motion is also discussed for the conducted experiments to explore the fluidization regimes.

4.2 Experimental Setup and Experiments

The experiments were conducted in the T. Blench Hydraulics Laboratory at the University of Alberta in Canada. Figure 4.1 shows the schematics of the experimental setup. A 10 m long, 0.8 m wide, and 0.8 m deep towing tank was used for the scour experiments, with a computer-controlled carriage on the top that moves along the length of the tank (x – direction). The carriage held a 1 m long and 25 mm diameter PVC pipe with a well-designed circular nozzle at the lower end to produce a circular jet. The upper end of the pipe was attached to a flexible hose, connected to a 0.5 HP centrifugal pump. The pump drove water from the towing tank to produce the jet and thus recirculated water during scour testing. A valve, and a magnetic flowmeter were attached between the pump and the flexible hose to control and measure the flow. The attachment of the PVC pipe at the carriage allowed to produce a submerged jet with α between 30° and 90°, and h between 0 and 150 mm. A 1.5 m long, 0.5 m wide, and 0.25 m deep plexiglass sandbox was used to create a 0.25 m deep sand bed for scour testing. The sand box had sand traps on both sides to prevent sand moving on the towing tank bed during scour test.

For the static scour measurement, a point gauge was mounted on the carriage on the opposite side of the PVC pipe. It could be moved in both y and z - directions to take profiles of the scoured trench. A high-speed camera (Phantom v211, Vision Research, Wayne, New Jersey), equipped with a Nikon lens ((Nikon AF Micro NIKKOR 60 mm f/2.8D) was used to capture the sand movement and identify the fluidized zone. The camera was placed close to the front panel of the towing tank focusing on the center of the sand box at z-x plane. A LED lamp was placed under the camera to illuminate the sands on that plane.

Before the start of scour testing, the sand bed inside the sand box was levelled, with the towing tank filled with water to 0.6 m depth. The nozzle was adjusted to set the desired jet impinging height and angle. The jet nozzle was set 2 m upstream of the sand box center by translating the carriage. The travel length of the carriage was set to 4 m so that the sand box remained about at the middle of the run and could be less affected by acceleration or deceleration of the carriage. The PVC pipe was set close to the tank sidewall so that the gap between the jet nozzle and the wall was about 2 mm. This ensured that the jet was very close to the wall to resemble a half-model for jet scour testing, similar to the approach of Pagliara et al. (2008). The half-model features the same

jet velocity so that $d = \sqrt{2}d_t$, where d_t is the jet diameter in half-model and d is the equivalent full-model jet diameter. This half-model configuration facilitates the observation of the dynamic characteristics of the scour hole. According to Unger and Hager (2006 and 2007) and Bombardelli et al. (2018), the boundary layer along the glass wall has minimal effect on the jet characteristics for such arrangement. Further, Rajaratnam and Pani (1974) reported that if the wall shear stress can be neglected, the circular wall jet can be treated as a circular free jet. Figure 4.2 shows that the scour profiles for half and full-model for scour testing by stationary and translating jets match quite well. The little discrepancies in the profiles may have resulted since an 18 mm nozzle was used for the full-model. For a 12.5 mm nozzle in the half model, using a 17.6 mm nozzle would be more appropriate since $d = \sqrt{2}d_t$. However, a 17.6 mm nozzle was not available.

At the beginning of the test, the pump was started to create the jet. Flowrate in the nozzle was measured with a magnetic flowmeter, and controlled with a valve. The carriage was then operated using LabVIEW software by National Instruments to translate the jet at the desired translating velocity. During the jet translation, sand movement was recorded using the high-speed camera. After the carriage completed its 4 m run, the jet was stopped by switching off the pump, and the carriage was moved over the sand box. Then the point gauge was used to take profile of the scoured trench at the middle of the sand box. After that the carriage was moved to its initial position upstream of the sand box and the sand bed was prepared for a new test.

Table 4.2 shows the details of the experiments. To assess the effect of jet inclination for short jets ($h = 4d_t$), test series A to D were conducted for $30° \leq \alpha \leq 90°$. In each of these series, the effect of jet translation was explored for $0 \leq U_t \leq 224$ mm/s. Test series E was conducted to realize the effect of long impingement ($h = 9d_t$) for scour at different translating velocities. Test series F and G were carried out for a single translating velocity ($U_t = 12$ mm/s) to understand the effect of jet diameters and jet velocities, respectively.

Since previous studies for translating jet scouring mostly used finer sands with a median sediment size of $D_{50} < 0.33$ mm, all the test series except H were conducted with a coarse sand of $D_{50} = 0.54$ mm and a sediment non-uniformity of $\sigma_s = (D_{84}/D_{16})^{1/2} = 1.4$. The test series H was conducted with finer sands of $D_{50} = 0.23$ mm and $\sigma_s = (D_{84}/D_{16})^{1/2} = 1.3$, to compare the results for fine and coarse sands.

4.3 Scouring Features

4.3.1 Static Scour Profiles

Figure 4.3 shows the scour profiles of the sand bed as the sand particles settle down after the jet passed. Therefore, these profiles are the static scour profiles in the transverse direction of the jet translation (y – direction). For impingement angles $\alpha \geq 60°$, the profiles show deposition rather than erosion (test series A and B). This is because at these angles, the amount of sediment deposition downstream of the jet exceeds the amount of sediment movement outside the ridge. As U_t increases, deposition increases for $60° \leq \alpha \leq 90°$. However, for test series C and D, at smaller impingement angles (i.e., $\alpha \leq 30°$), and smaller translational velocity ($U_t = 12$ mm/s), mild trench and prominent ridge formation are seen with maximum static scour depth, $z_{sm} = 8$ mm and 26 mm, for $\alpha = 45°$ and 30°, respectively. For fine sand in test series H ($D_{50} = 0.23$ mm), trench with distinctive ridge can be seen even for bigger impingement angle ($\alpha = 90°$) and for 2 mm/s $\leq U_t \leq 52$ mm/s. This confirms that, for the same experimental conditions, static scour for finer sand is more than the coarser sand – an observation similar to experiments with stationary jets in previous studies (e.g., Aderibigbe and Rajaratnam, 1996; Amin et al., 2021). However, considering test series A and E, the effect of the impingement height for $4d \leq h \leq 9d$ seems negligible. Figure 4.3b shows the effect of jet diameters and velocities on the static scour depth in test series F and G, respectively. As the jet diameter or velocity increases, the static scour depth and ridge height increases. However, for all the test series, the static scour depths for translating jet scour are minimal, even for lower translating velocity, i.e., $U_t = 12$ mm/s. This is because the jet does not stay at the same location long enough to allow the sand moving out of the scour regime.

4.3.2 Dynamic Scour Profiles

The dynamic sour profiles, extracted from the mean of the instantaneous sediment movement images are shown in Figure 4.4. Test series A, B, C, D, H, and E in Figure 4.4a show that as U_t increases, the dynamic scour profiles become shallow and elongated in the direction of the jet translation (x-direction). The shape of the profiles also varies with the jet impingement angle. In general, as the impingement angle decreases, the profiles become shallow. Comparison of test series A and H shows that the dynamic profile for finer sand is deeper and longer. For $U_t = 52, 72,$ and 92 mm/s, pulsating forms are seen in the profiles of test series H. This indicates that the finer sand behaves like a fluid medium with wave formations at higher translating velocities.

Comparison of test series A and E shows that the depth of the profiles decreases with the increase of h. The profiles also become elongated as h increases. Figure 4.4b shows that the size of the fluidized regime increases noticeably with the increase of jet diameters (test series F), or jet velocity (test series G).

Figure 4.5 shows dimensionless profiles of the dynamic scour for test series A, B, C, and D. The corresponding profiles in Figure 4.4a are normalized with the longitudinal length of the fluidized regime (x_m), and the maximum dynamic scour depth (z_m), in x and z – directions, respectively. For each test series, the profiles for different U_t collapse into a single shape. Therefore, the general equation for the dynamic scour profile can be expressed as functions of x and α

$$\frac{z}{z_m} = \varphi_1(\alpha)\left(\frac{x}{x_m}\right)^3 + \varphi_2(\alpha)\left(\frac{x}{x_m}\right)^2 + \varphi_3(\alpha)\left(\frac{x}{x_m}\right) + \varphi_4 \tag{4.1a}$$

where the sought mathematical function φ is given by the Equations 4.1b to 4.1e, for $30° \leq \alpha \leq 90°$ and $E_c = 5.8$.

$$\varphi_1 = -7.5 \sin\alpha + 9.0 \tag{4.1b}$$
$$\varphi_2 = 11.5 \sin\alpha + 15.6 \tag{4.1c}$$
$$\varphi_3 = -3.6 \sin\alpha + 6.0 \tag{4.1d}$$
$$\varphi_4 = 0.3 \sin\alpha + 0.28 \tag{4.1e}$$

Equation 4.1 fits the dynamic scour profiles well with $R^2 = 0.98$, 0.95, 0.71, and 0.85 for test series A, B, C, and D.

4.3.3 Maximum Dynamic Scour Depth

Figure 4.6 shows the variation of maximum dynamic scour hole depth z_m for different parameters. In Figure 4.6a, considering test series A to D, z_m reduces with r and increases with α. Test series H with $D_{50} = 0.23$ mm exhibits bigger z_m than test series A with $D_{50} = 0.54$ mm. Similarly, test series A with $h = 4d$ shows bigger z_m than test series E with $h = 9d$. These variations of z_m with D_{50} and h are similar to the scour by stationary jets. Yeh et al. (2009) showed reported that a rational function predicts the relative scour depth in terms of the velocity ratio. However, a rational function does not satisfy the experimental data of this study for dynamic scour depth. Rather, a

general relation is developed considering the relative dynamic scour depth is a function of the impingement angle and translating velocity.

$$\frac{z_m}{(h+d)} = \psi_1(R_{tj})\alpha^2 + \psi_2(R_{tj})\alpha + \psi_3(R_{tj}) \tag{4.2a}$$

where sought function ψ is given by Equation 4.2b to 2d, for $30° \leq \alpha \leq 90°$, $29 \leq r \leq 224$, and $E_c = 5.8$

$$\psi_1(r) = 0.67R_{tj}^2 - 0.04R_{tj} \tag{4.2b}$$

$$\psi_2(r) = -84.12R_{tj}^2 + 4.21R_{tj} \tag{4.2c}$$

$$\psi_3(r) = 2025.30R_{tj}^2 - 103.22R_{tj} + 1.05 \tag{4.2d}$$

Figure 4.6b shows the data fitting for Equation 4.2.

4.3.4 Stationary vs Translating Jet Scouring

As shown in Figure 4.6a, z_m reduces with the increase of U_t. It can be inferred that z_m is bigger for a stationary jet ($U_t = 0$) than for a translating jet ($U_t > 0$). To check this hypothesis, experimental results for $U_t = 0$ mm/s is compared with $U_t = 12$ mm/s for test series A, B, C, and D in Figure 4.7. It should be noted that the stationary jet scour is a function of testing time, while the translating jet scour is a function of translating speed. Therefore, to compare the stationary case with the translating one, dynamic scour depth for a short time of scour ($t = 150$ s) is compared with the dynamic scour depth for a small translating speed ($U_t = 12$ mm/s). It is observed that the scour depth for stationary jet scour is more than the translating jet. Further, as the impingement angle α increases, the difference in scour depth between stationary and translating jet scour decreases.

Figure 4.8 shows that for $1.9 \leq E_c \leq 9.6$, the dimensionless scour depths for different translating velocities vary linearly with the erosion parameter E_c. According to (Amin et al., 2021), Equation 4.3 gives the asymptotic scour depth $z_{m\infty}$ for a stationary jet,

$$\frac{z_{m\infty}}{(h+d)} = 0.49\,E_c - 0.06 \tag{4.3}$$

Based on this expression and experimental results as shown in Figure 4.8, a general relation can be proposed for predicting the depth of scour as a function of E_c for vertically impinging jet of any

translating velocity,

$$\frac{z_m}{(h + d)} = C_1 E_c - C_2 \qquad (4.4)$$

where C_1 and C_2 are dimensionless coefficients, which depend on the jet translating velocity U_t.

4.4 Sediment Kinematics

Sand motion inside the scour hole is captured by producing streamlines from the high-speed camera images using PIV technique. Figure 4.9a shows the mean streamlines of sediment motion for test series A. For $U_t = 12$ to 52 mm/s, a vortex forms at the leeward side of the jet and remains close to the jet. The streamlines near the vortex center are sparsely distributed, indicating the sand particles are moving radially towards the periphery of the vortex due to centrifugal force. Although the pressure gradient inside the vortex tries to keep the sand particles near the center, Lasheras and Tio (1994) reported that the sand particles have greater inertia due to the density difference in sand-water system and thus the centrifugal force becomes dominant. As the jet is translating, it scours the sand bed in the windward direction, and entrains sand particles. A portion of the entrained sand translates directly to the leeward side and deposits there. Another portion gets entrapped in the vortex. As the vortex translates along with the jet, it captures some fresh sands and simultaneously discharges some to the leeward side. A flow separation is observed inside the scour hole, indicating the boundary of the vortex and deflected jet. The vortex is typically elliptical in shape and the orientation of the vortex changes from vertical to horizontal with U_t. For $U_t = 72$ and 92 mm/s, sand particles are entrained inside the jet without any distinct principal vortex. However, multiple small vortices may be present without noticeable sand entrapment as reported by Unger and Hager (2005) for sand bed scouring at a cylindrical pier.

Figure 4.9b shows the streamlines of sand motion for a small translating velocity, i.e., $U_t = 12$ mm/s. For test A1, H1, and E1 with $\alpha = 90°$, the streamlines show similar vortex formation. For test H1, the fluidized zone and vortex are larger compared to test A1 for the same hydraulic conditions. This is because H1 contains finer sands than A1 ($D_{50} = 0.23$ mm versus 0.54 mm). For test E1 with long impinging height ($h = 9d$), the vortex center stays near the bottom of the scour hole whereas for short impinging height ($h = 4d$) in test A1, it stays near the initial undisturbed surface of the sand bed. For $30° \leq \alpha \leq 60°$, the vortex forms at the windward side of the translating

jet. The principal vortex remains close to the jet boundary while the minor vortices remain either near the deflected jet or near the principle vortex. Figure 4.10 shows schematics of the sediment motion inside the scour hole for a translating jet with different jet inclinations.

Figure 4.11 shows the vertical distribution of the velocity component in x- direction, u inside the principal vortex. Although for all the cases, the jet is translating to the right, the rotation of the principal vortex is in opposite direction for normal and obliquely impinging jets., characterized by the distribution of u. Velocity distribution in the opposite directions are nearly equal for $\alpha = 45°$. For $\alpha = 30°$, the velocity distribution is symmetric about the horizontal axis of the vortex center.

Figure 4.12 shows the velocity distribution of sand particles inside the fluidized zone. For $\alpha = 90°$ (Figure 4.12a), the maximum velocity varies between 0.18 to 0.30 m/s for $U_t = 12$ to 92 mm/s. The maximum velocity for the stationary case is bigger and is observed in the vortex region. On contrary, for translating jets, the maximum velocity region of the sediment motion is inside the jet. The velocity vectors are mostly todards the leeward direction of the jet translation. However, in Figure 4.12b, the oblique impinging cases (test series B1, C1, and D1) show velocity vectors in both the windward and leeward direction of the jet. This indicates that the sediments initially moves to the windward direction due to the oblique impingement of jet since the jet has a jet velocity component in that direction. Thereafter, the sediments near the boundary of the fluidized zone travel backward to the leeward side of the jet and deposit there. Maximum velocity magnitude for oblique cases varies between 0.18 to 0.27 m/s. For fine sand with $D_{50} = 0.23$ mm, the velocity distribution of the sand particles resembles to the velocity distribution of a jet in crossflow, probably due to the fluidized nature of the sand bed with smaller grain size. For all the translating jet cases with $R_{tj} = 0.004$ to 0.034, the direction of the velocity vectors show that the u component of the velocity is the dominant velocity for sand movement. Therefore, in Figure 4.13, the profiles of the u –velocity are plotted as a function of the vertical depth. Note that inside principle vortex, there is a reversal of the direction of u, as shown in Figure 4.11. Therefore, inside the vortex, the bottom portion of the u-velocity near the bed is considered in Figure 4.13, similar to the approach of Unger and Hager (2007).

To explore the similarity of the u-velocity profiles, the dimensionless profiles are created with the maximum u – velocity u_m as the scale for u, and z_m as scale for z, where z_m is the vertical distance

from u_m to $0.5u_m$. The dimensionless profiles collapsed into a Gaussian equation,

$$\frac{u}{u_m} = e^{-\left(\frac{1}{1.2}(z/z_m)\right)^2}$$

(4.5)

4.5 Summary and Conclusions

This work shows the results of an experimental study of scour of cohesionless soils with circular translating jets impinging at different inclinations. The testing was conducted in a half-model configuration, so that the experiments could be observed from the side of the tank. Direct measurements of static scour features were made using a point gauge. A high-speed camera was used to identify the fluidized zone, and understand sediment kinematics. The main conclusions of this study are as follows:

1. The static scour depth is minimal for a translating jet scour, compared to the stationary case for $D_{50} = 0.54$ mm, 32 mm/s $\leq U_t \leq$ 92 mm/s and $30° \leq \alpha \leq 90°$. However, depressions on the surface of the bed are observed for $U_t = 12$ mm/s, and $30° \leq \alpha \leq 45°$.

2. The dynamic scour profiles in the longitudinal direction gets shallower and elongated as the jet translating velocity increases.

3. For a constant translating velocity, the maximum depth of the fluidized zone decreases as the jet angle of inclination decreases.

4. For constant translating velocity, jet inclination angle, and jet velocity, the maximum depth of the fluidized zone increases with the jet diameter. Similarly, for constant translating velocity, jet inclination angle, and jet diameter, the maximum depth increases with the jet velocity.

5. For the same experimental conditions, the maximum depth of dynamic scour decreases with the increase of impinging height, and increases with the decrease of the median size of the sand.

6. Dimensionless profiles of the fluidized zone at different jet translating velocities and a fixed impinging angle show similarity.

7. For the same experimental conditions, the maximum dynamic scour depth for a stationary jet with even a short time of scour (≈ 150 s) is bigger than the one for a translating jet with a

slower translating velocity ($\approx$12 mm/s).

8. Dimensionless maximum dynamic scour depth can be expressed as functions of the erosion parameter and the jet velocity to translating velocity ratio. This is similar to the case for stationary jet, where this depth can be expressed as a function of the erosion parameter

9. Sediment kinematics study of the fluidized zone reveals that a principal vortex is present inside the scour hole along with few minor vortices. The principal vortex resides on the leeward side of the jet for $\alpha = 90°$, whereas it stays on the windward side of the jet for $\alpha < 90°$. The vortices and the jet itself entrain sediment and play important role in the sediment transport.

10. Due to the translation of the jet, the horizontal velocity component is the dominant component for sediment transport. This velocity can be expressed by a Gaussian relation.

This study is one of the first on the detailed observation of sediment motion for translating jet scouring of loose bed. Empirical expressions have been developed for the fluidized zone, and sediment kinematics is discussed based on PIV technique. This study will help in practical engineering problems with moving jet scour, and will facilitate computational modeling by providing experimental measurements.

Table 4.1: Studies on the scour of sand beds by translating jets.

Study	Type of Jet	α	d (mm)	V_j (m/s)	U_t (m/s)	D_{50} (mm)	h (mm)	h/d	V_j/U_t	E_c	Application
Perng and Capart (2008)	Plane jet	210°	-	8-10.9	0.01-0.1	0.33	0	0	80-1090	-	Engineering tools moving on the sea bed
Su et al. (2007), and Berghe et al. (2011)	Circular Jet (Needle)	210°	0.6	6-36	0-0.07	0.08-0.17	0	0	85-∞	∞	Marine Trenchers
Yeh et al. (2009)	Circular jet	90°	127	2.05	0.09-0.51	0.26	760	6	4-24	5.28	Scour due to discharge below a vessel
Weegenaar et al. (2015)	Circular jet	90°	5-11	30-40	0.25-1	0.14-0.28	17	1.5-3.4	30-160	1.54-9.90	Water-jet assisted dragheads of dredgers
This study	Circular jet	30°-90°	8.5-25.5	0.9-4.48	0-0.092	0.23-0.54	50-112.5	2.0-6.4	9.8-∞	1.9-9.6	Generic

Table 4.2: Details of the experiments

Test series	Test ID	D_{50} (mm)	d_t (mm)	d (mm)	h (mm)	V_j (m/s)	α (°)	U_t (mm/s)	$R_{tj} \times 10^{-3}$ (-)	Re × 10^4 (-)	F_d (-)	E_c (-)	Comment
A	A0 A1 A2 A3 A4 A5	0.54	12.5	17.7	50	2.69	90	0 12 32 52 72 92	0 4.5 11.9 19.3 26.8 34.2	4.8	28.8	5.8	Vertical jet ($\theta = 90°$) at different translating velocities. Test ID: AU_t, e.g., A0 for non translating, A12 for translating at 12 mm/s.
B	B0 B1 B2 B3 B4 B5	0.54	12.5	17.7	50	2.69	60	0 12 32 52 72 92	0 4.5 11.9 19.3 26.8 34.2	4.8	28.8	5.8	Oblique jet ($\theta = 60°$) at different translating velocities
C	C0 C1 C2 C3 C4 C5	0.54	12.5	17.7	50	2.69	45	0 12 32 52 72 92	0 4.5 11.9 19.3 26.8 34.2	4.8	28.8	5.8	Oblique jet ($\theta = 45°$) at different translating velocities
D	D0 D1 D2 D3 D4 D5	0.54	12.5	17.7	50	2.69	30	0 12 32 52 72 92	0 4.5 11.9 19.3 26.8 34.2	4.8	28.8	5.8	Oblique jet ($\theta = 30°$) at different translating velocities
E	E0 E1 E2 E3 E4 E5	0.54	12.5	17.7	112.5	2.69	90	0 12 32 52 72 92	0 4.5 11.9 19.3 26.8 34.2	4.8	28.8	2.9	Long impingement ($h = 9d$) of vertical jet at different translating velocities
F	F1 F2 F3 F4 F5	0.54	6 8 12.5 14 18	8.5 11.3 17.7 19.8 25.5	50	2.69	90	12	4.5	2.3 3.0 4.8 5.3 6.9	28.8	3.1	Variable jet diameters with vertical impingement and a fixed translating velocity
G	G1 G2 G3 G4 G5	0.54	12.5	17.7	50	0.90 1.79 2.61 3.59 4.48	90	12	13.3 6.7 4.6 3.3 2.7	1.6 3.2 4.6 6.4 7.9	9.6 19.2 27.9 38.4 47.9	1.9 3.8 5.6 7.7 9.6	Variable jet velocities with vertical impingement and a fixed translating velocity
H	H0 H1 H2 H3 H4 H5	0.23	12.5	17.7	50	2.69	90	0 12 32 52 72 92	0 4.5 11.9 19.3 26.8 34.2	4.8	44.1	8.8	Fine sand ($D_{50} = 0.23$ mm) with vertical jet impingement and different translating velocities

Notes: Re = jet Reynolds number, Re $= \rho_w V_j d/\mu_w$, ρ_w is density of water, ρ_s is density of sand, μ_w is dynamic viscosity of water; F_d: densimetric Froude number, $F_d = V_j/[\{(\rho_w-\rho_s)/\rho_w\}\ gD_{50}]^{1/2}$, g is acceleration by gravity; E_c: erosion parameter, $E_c = F_d\{d_t/(h+d_t)\}$. Note that d_t is used for E_c since the impinging height for full-model $= \sqrt{2}h$, and therefore, the ratio $h/(h+d_t)$ is same for both full and half-model.

Figure 4.1: Experimental setup for scour testing with translating jet (a) front panel of the towing tank, and (b) definition sketch for scour dimensions.
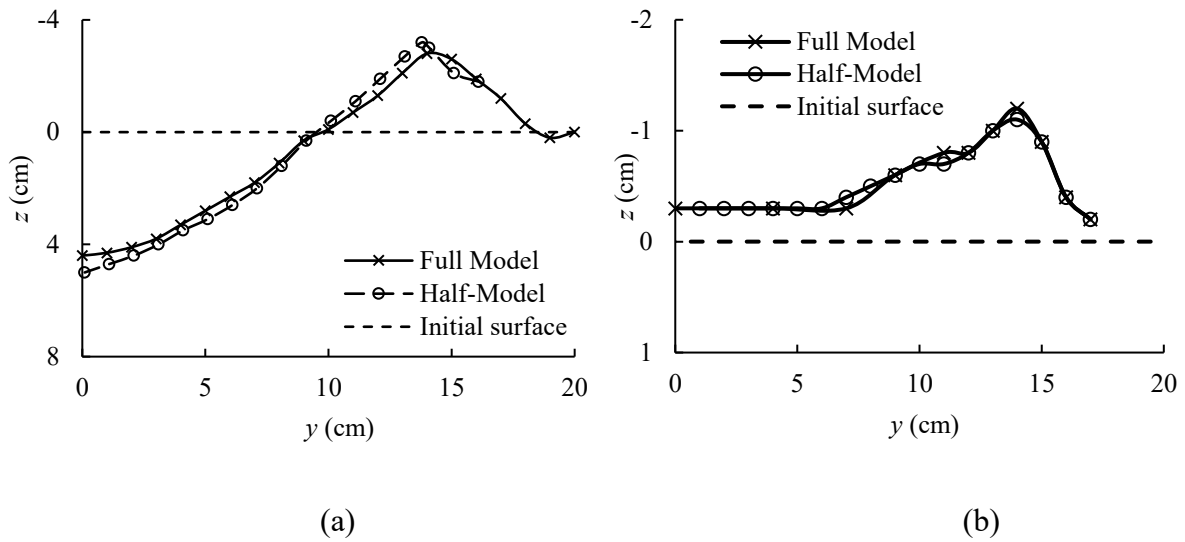
Figure 4.2: Scour profiles along the cross-channel for half versus full-model arrangements: (a) scouring by stationary jet. $D_{50} = 0.54$ mm, $d_t = 12.5$ mm, $d = 18$ mm, $h = 50$ mm, $V_i = 2.69$ m/s, and $U_t = 0$ m/s; (b) scouring by translating jet. $D_{50} = 0.23$ mm, $d_t = 12.5$ mm, $d = 18$ mm, $h = 50$ mm, $V_i = 2.69$ m/s, and $U_t = 0.012$ m/s.
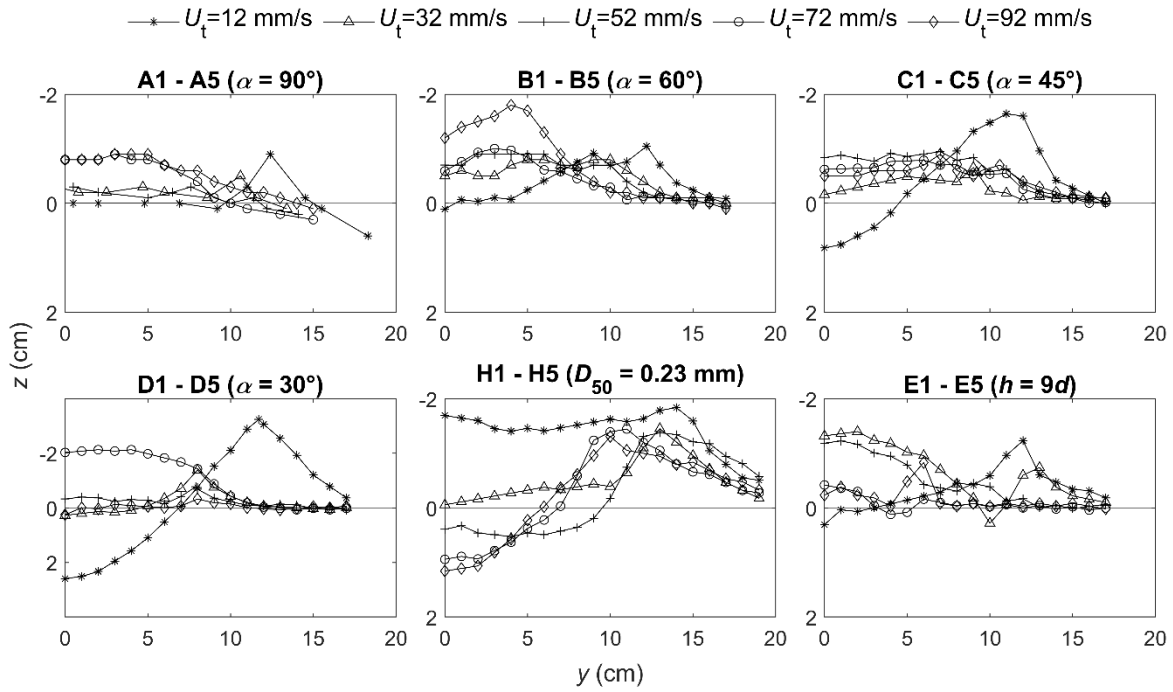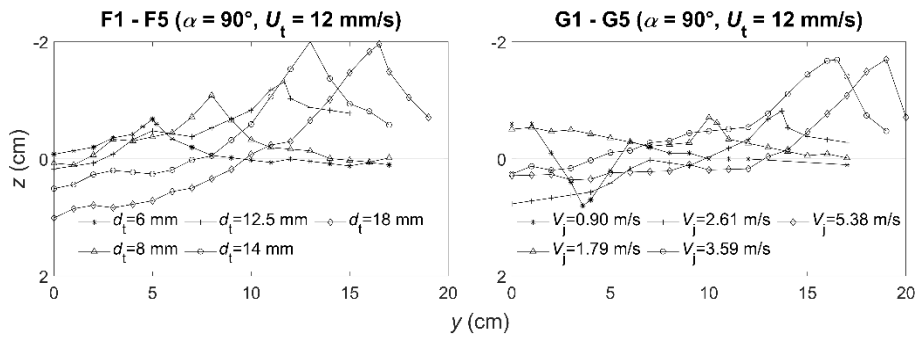
Figure 4.3: Static scour profiles at transverse direction of jet translation (a) profiles for 12 mm/s $\leq U_t \leq$ 92 mm/s and 30° $\leq \alpha \leq$ 90°; (b) profiles for 6 mm $\leq d_t \leq$ 18 mm (F series), and 0.90 m/s $\leq V_j \leq$ 3.59 m/s (G series). $z = 0$ and $y = 0$ indicate initial soil surface before scour, and tank wall, respectively.
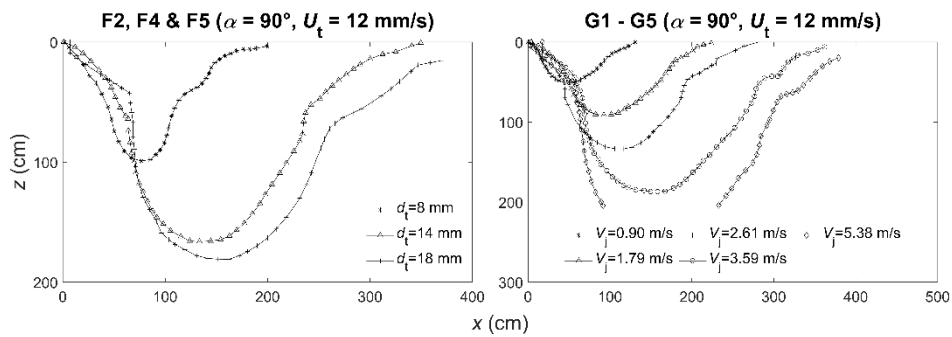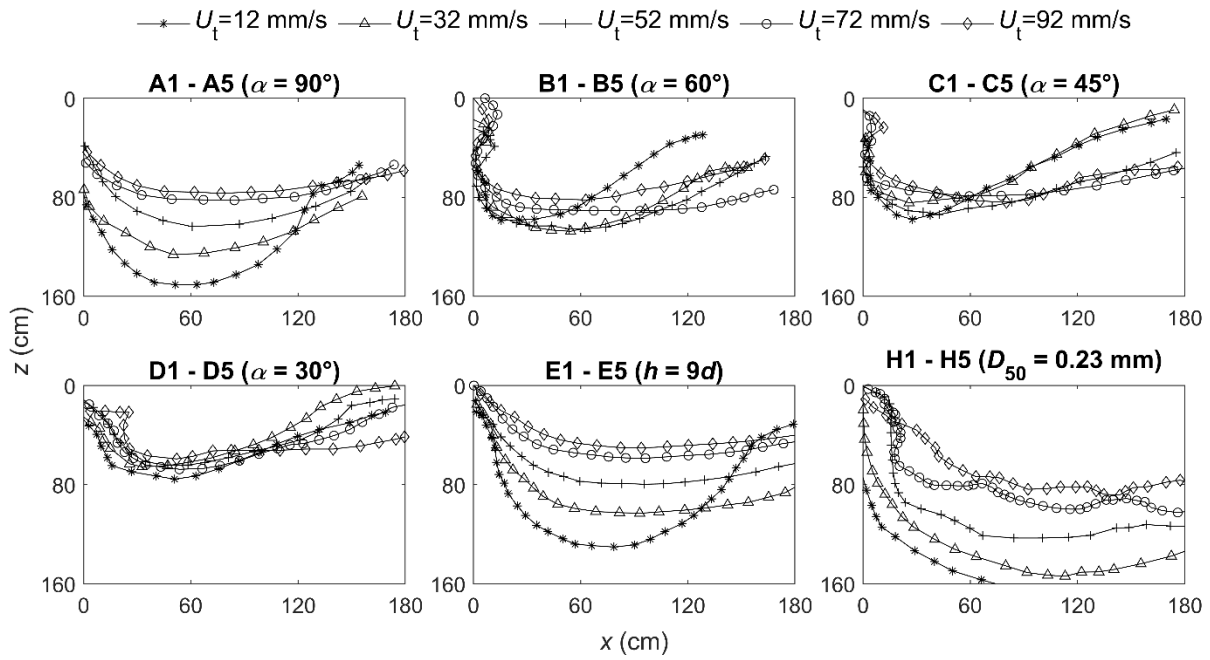
Figure 4.4: Dynamic scour profiles at the direction of jet travel for (a) 12 mm/s ≤ U_t ≤ 92 mm/s and 90° ≤ α ≤ 60°; and (b) 6 mm ≤ d_t ≤ 18 mm (F series), and 0.90 m/s ≤ V_j ≤ 3.59 m/s (G series). The jet is translating to the left.
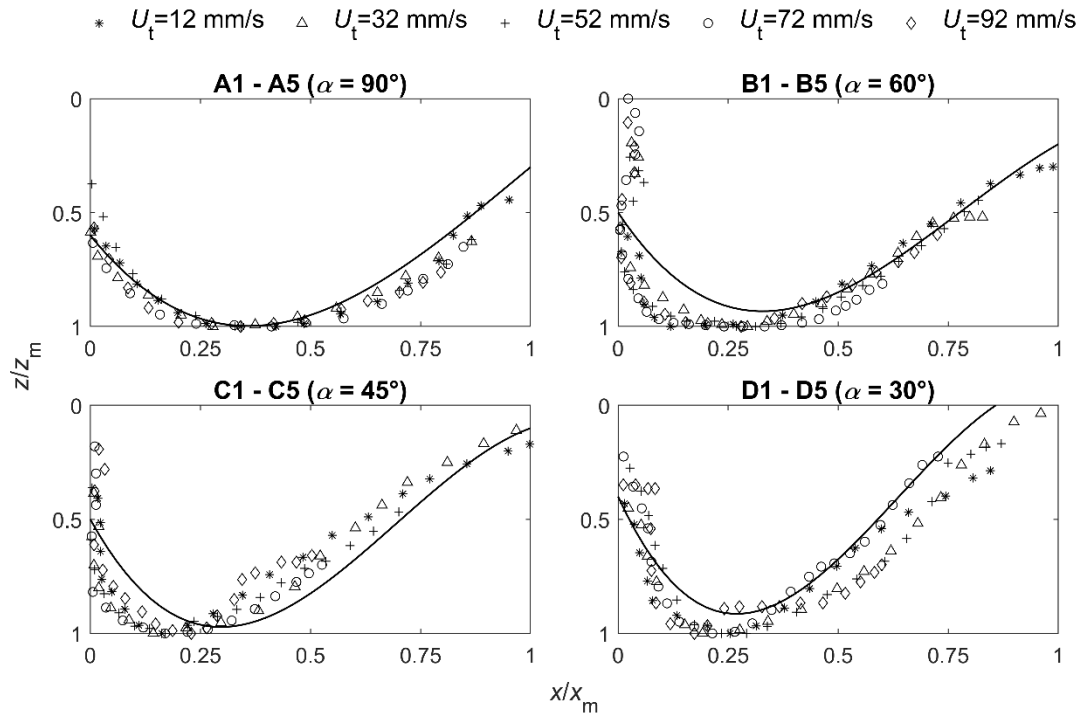
Figure 4.5: Similarity of the fluidized zone boundary in the direction of jet translation for $12 \text{ mm/s} \leq U_t \leq 92 \text{ mm/s}$ and $90° \leq \alpha \leq 60°$. Solid lines and marker symbols indicate Equation 4.1, and observed data, respectively. $z = 0$ represents initial soil surface before jet translation.
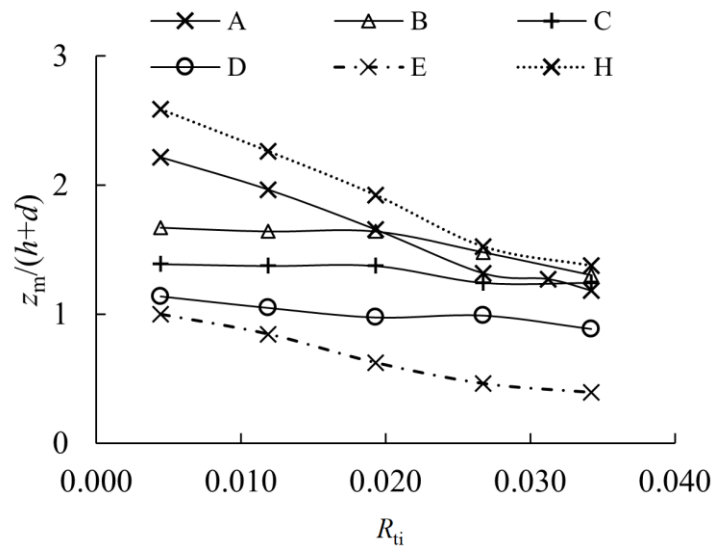
(a)
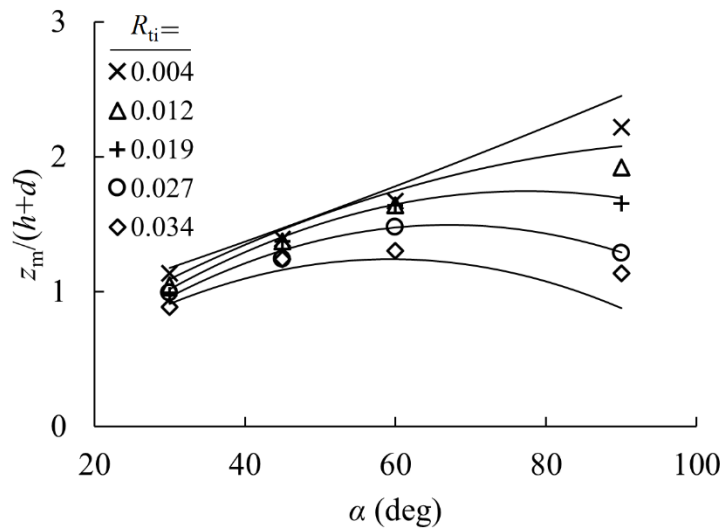
(b)

Figure 4.6: Variation of maximum dynamic scour depth: (a) dimensionless $z_m(R_{tj})$; and (b) dimensionless $z_m(\alpha)$.
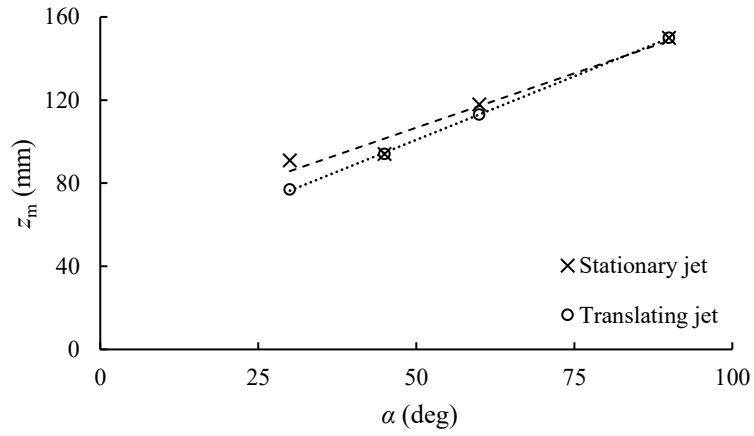
Figure 4.7: Comparison of z_m between stationary and translating jet scouring. For both cases, D_{50} = 0.54 mm, d_t = 12.5 mm, h = 50 mm, and V_j = 2.69 m/s. For stationary jet, time of scouring = 150 s; while for translating jet, U_t = 12 mm/s.
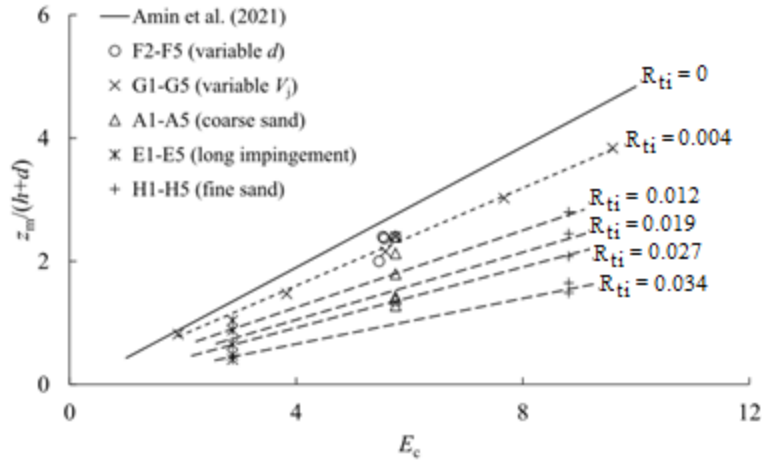
Figure 4.8: Dimensionless z_m as a function of E_c for $\alpha = 90°$ and 0 mm/s $\leq U_t \leq 92$ mm/s.
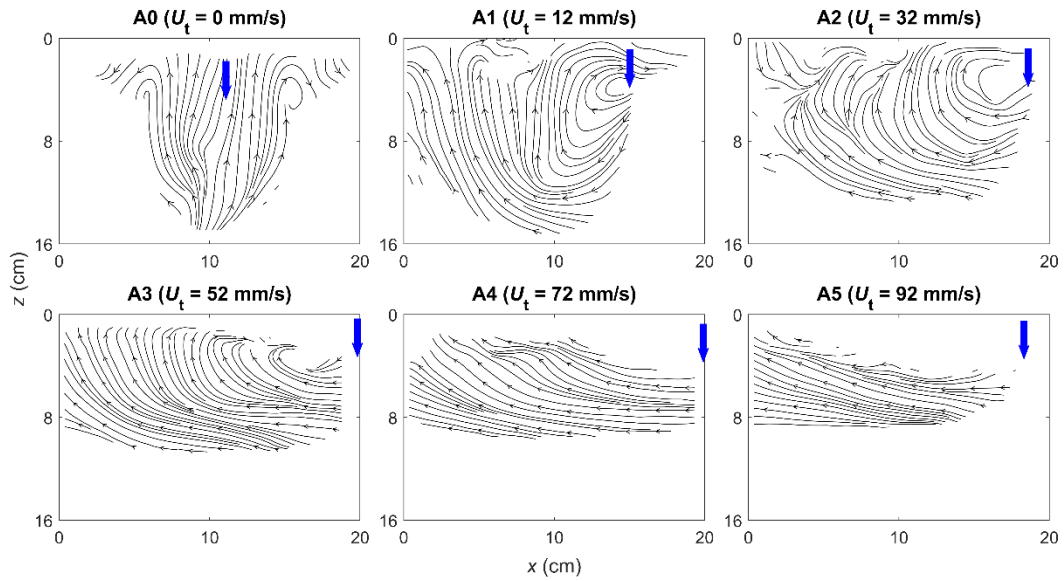
(a)
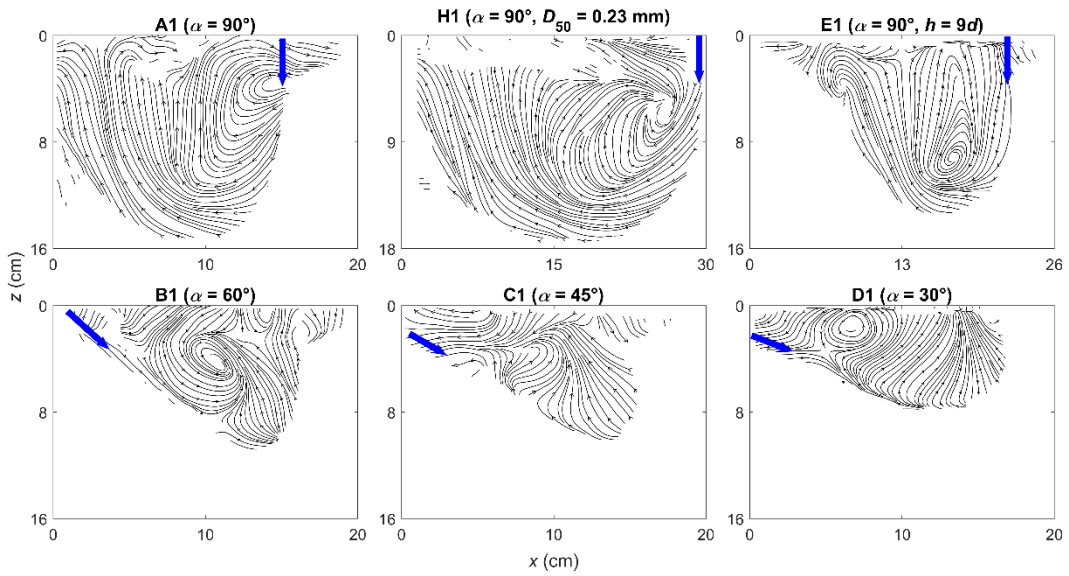
(b)

Figure 4.9: Mean streamlines of sediment motion inside scour hole for (a) 12 mm/s ≤ U_t ≤ 92 mm/s and α = 90°; and (b) 30° ≤ α ≤ 90° and U_t = 12 mm/s. Blue arrow indicates jet position. The jet is translating to the right.
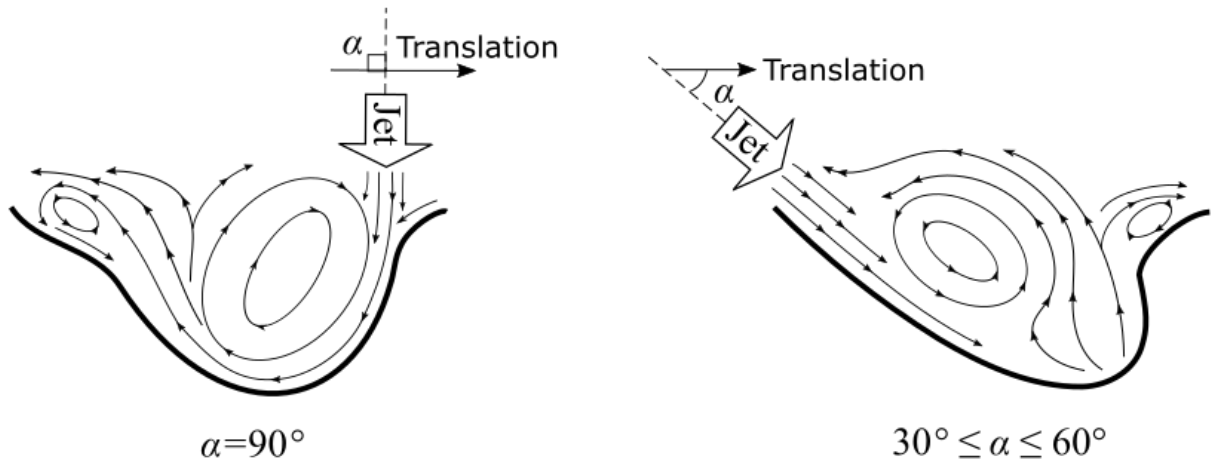
Figure 4.10: Schematics of sediment motion inside the scour hole for $30° \leq \alpha \leq 90°$.
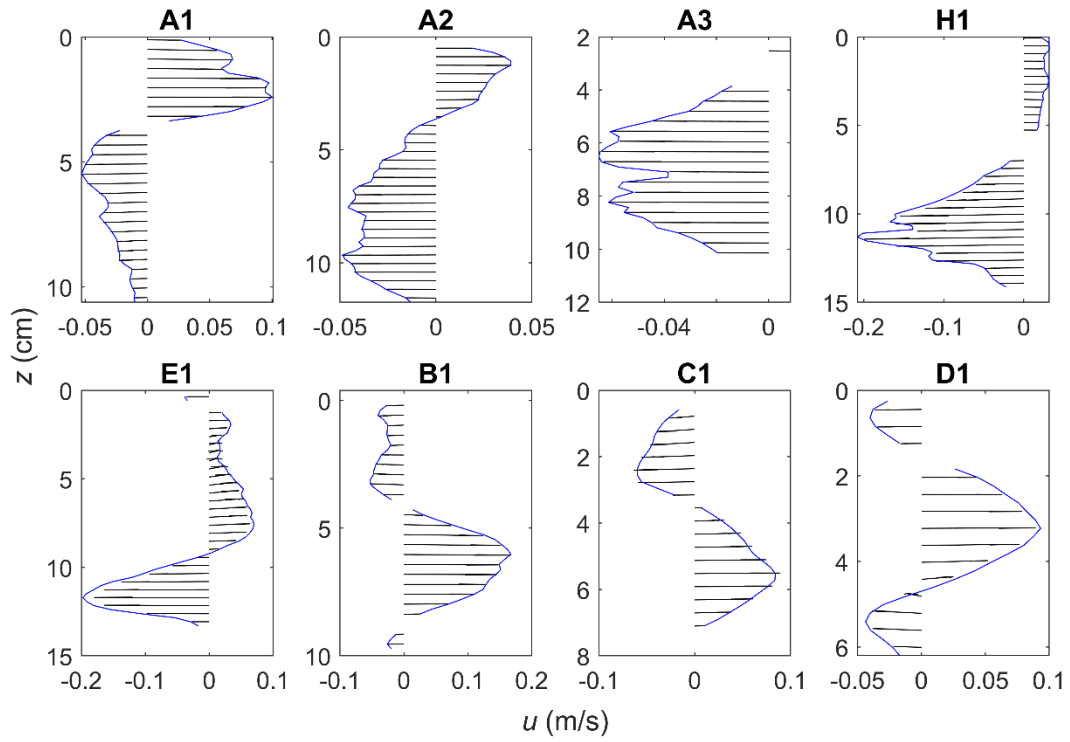
Figure 4.11: Vertical distribution of u through the principal vortex center.
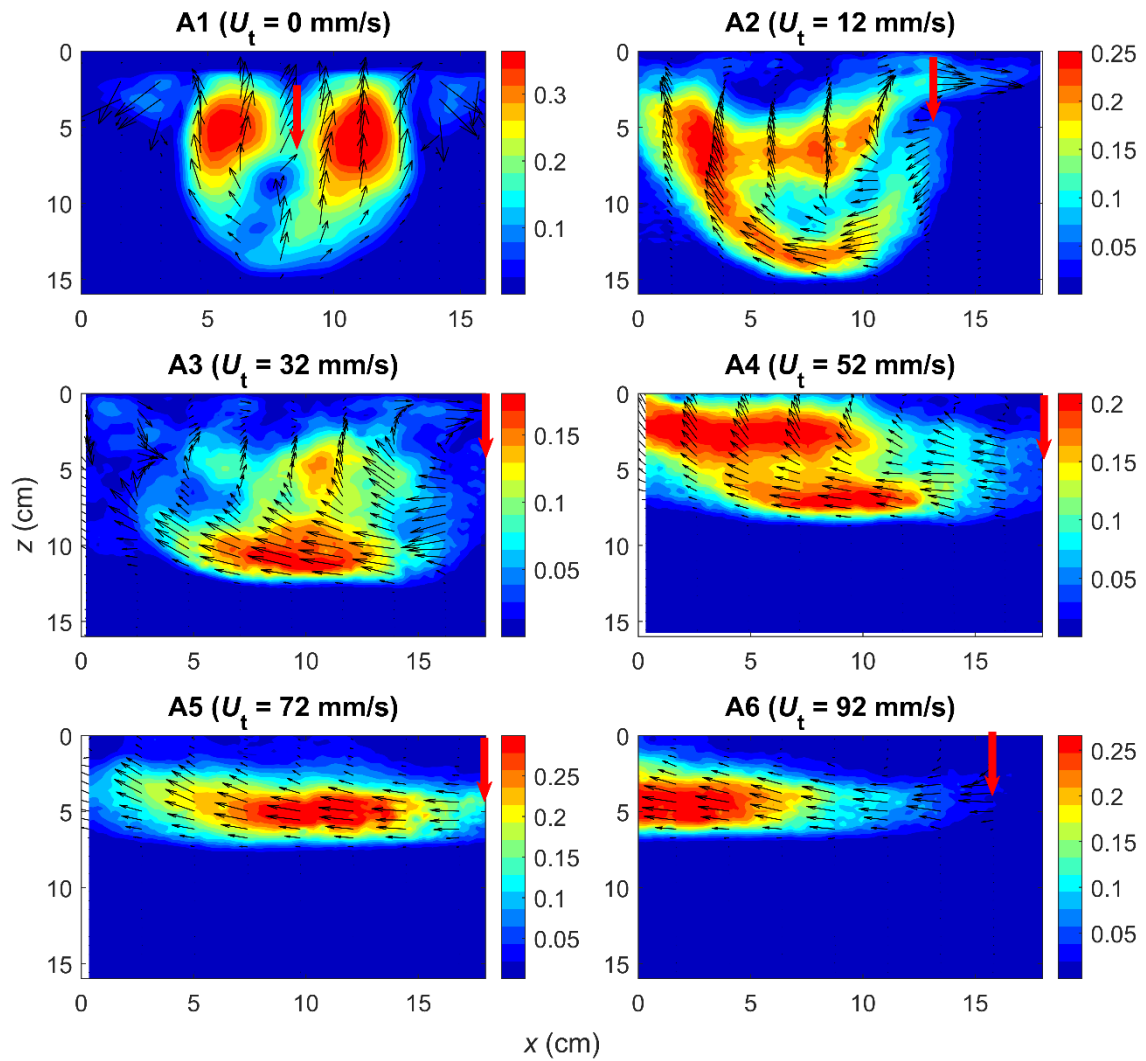
(a)

Figure 4.12: Velocity distribution of sand particles inside the fluidized zone for (a) vertical impingement with 12 mm/s $\leq U_t \leq$ 92 mm/s; and (b) U_t = 12 mm/s and 30° $\leq \alpha \leq$ 90°. Red arrow indicates jet direction. Velocity unit is: m/s. For all plots, V_j = 2.69 m/s and the jet is translating to the right.

(b)
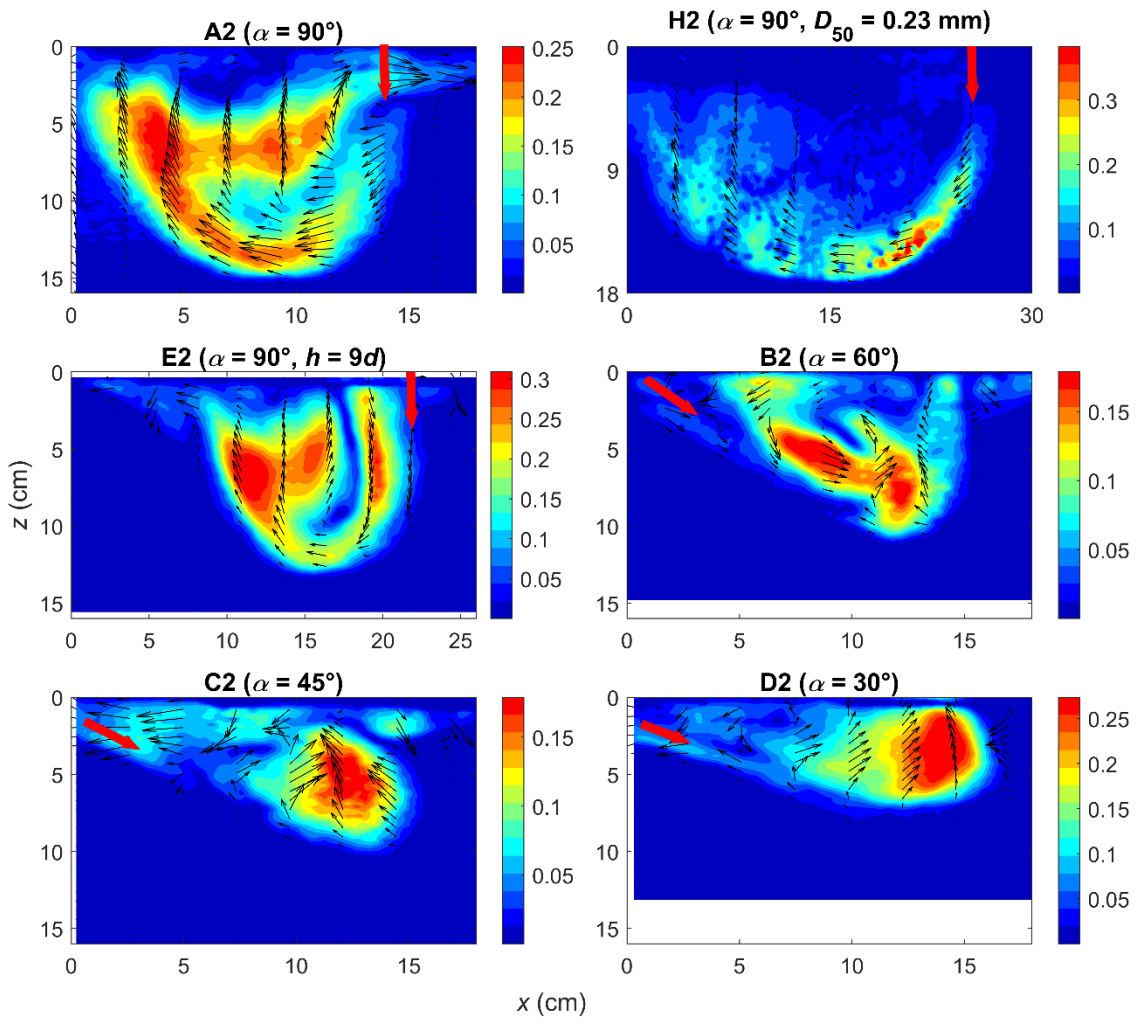
Figure 4.12: Cont'd.
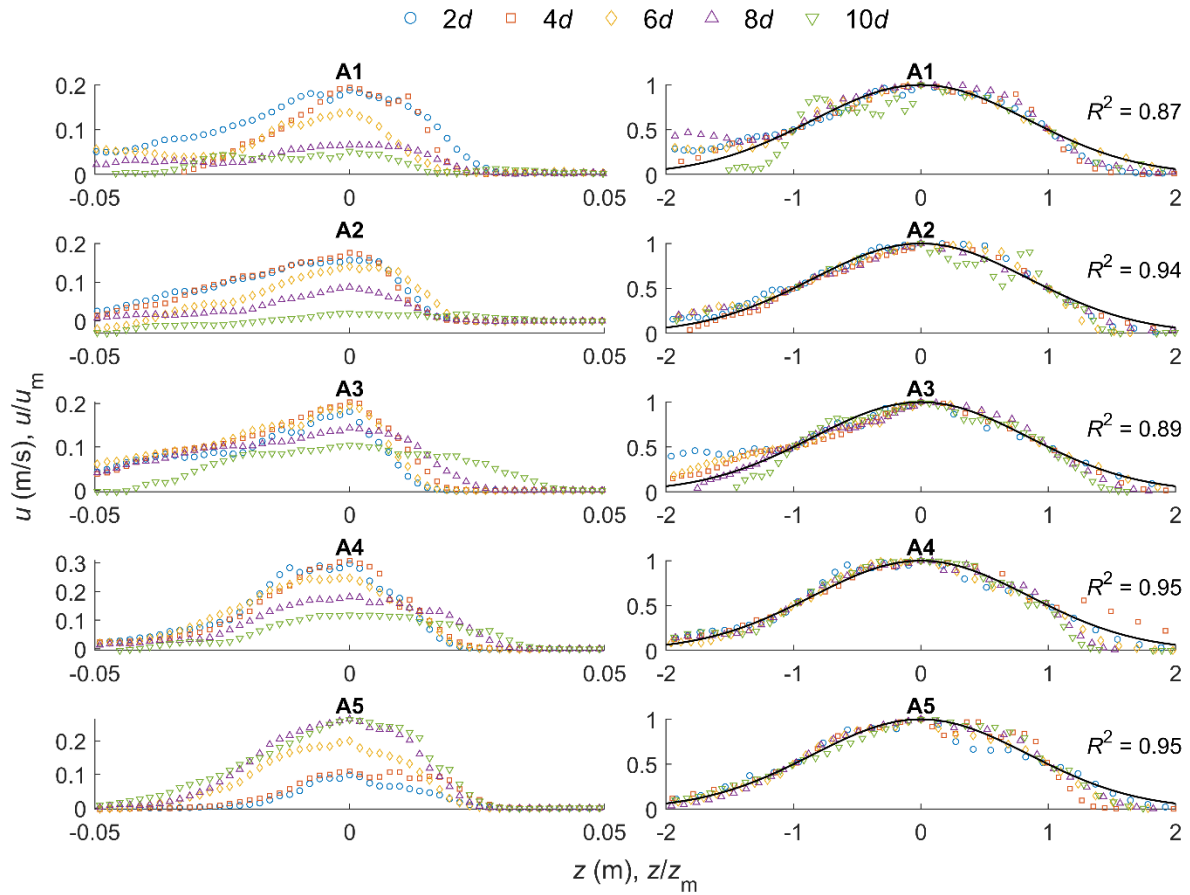
Figure 4.13: *u* - velocity profiles of sand particles at different horizontal distance from the jet nozzle, plotted as a function of the vertical depth for (a) vertical impingement with 12 mm/s $\leq U_t \leq$ 92 mm/s; and (b) U_t = 12 mm/s and 30° $\leq \alpha \leq$ 90°. The right side shows dimensionless profiles. Velocity unit is: m/s.
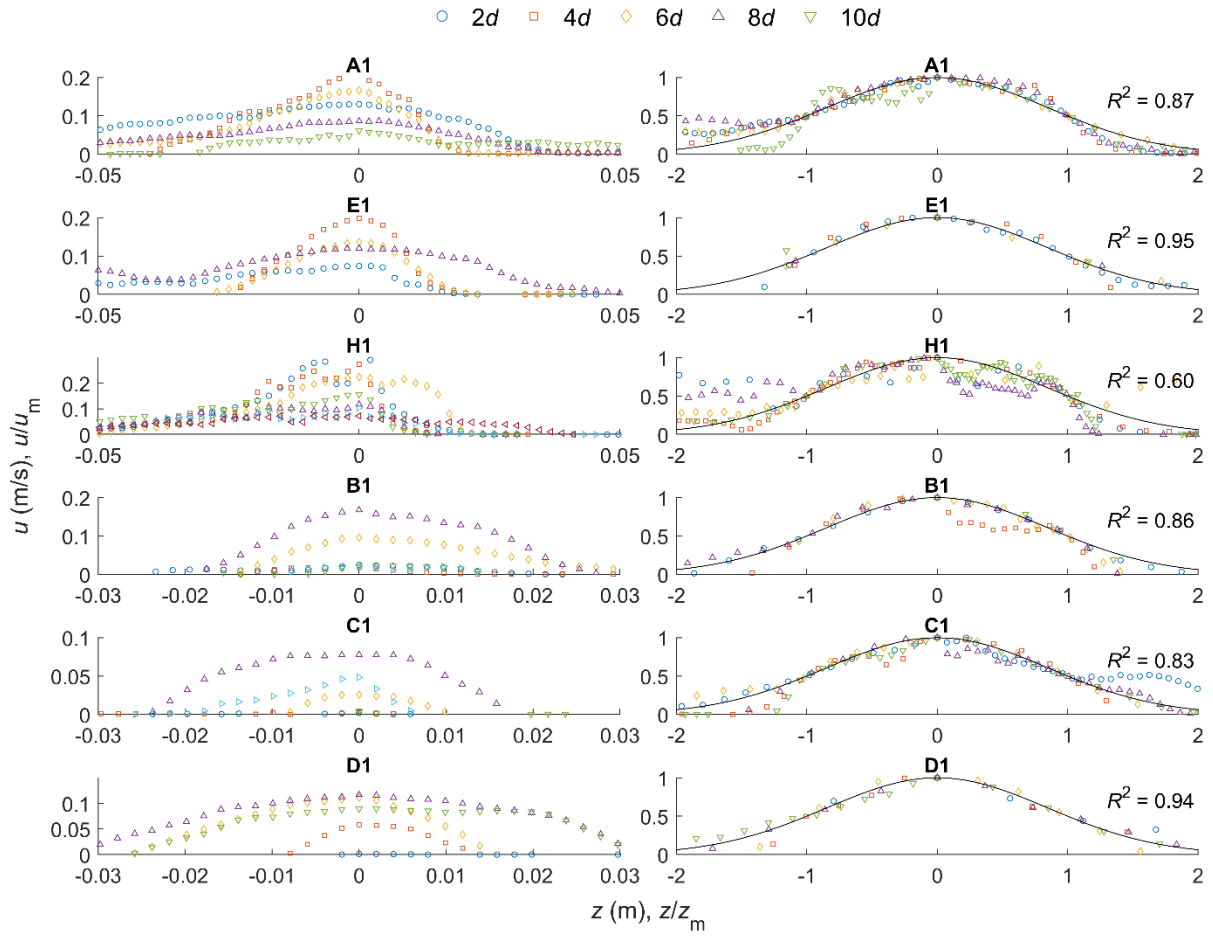
(b)

Figure 4.13: Cont'd.

CHAPTER 5. AIR-BUBBLE ENTRAINMENT IN STAGNANT WATER BY TRANSLATING TURBULENT JETS

5.1 Introduction

Air entrainment by plunging liquid jets is a common phenomenon in nature and it has many industrial applications. When a moving column of liquid passes though a gas medium before impinges into a pool of liquid, it is termed as a plunging jet (Roy et al., 2013). Although the mechanism of air entrainment is very complex, it usually occurs at the periphery of the plunging jet where it impinges on the free liquid surface and forms a depression with an envelop of air surrounding the jet. This mechanism is very efficient since it produces a large air-water interfacial area (Chanson and Manasseh, 2003). Many industrial applications utilize this mechanism since it ensures efficient dissolving of air in gas-liquid reactors. It is very effective for aeration in wastewater treatment (Stenstrom and Gilbert, 1981), and it has many potential applications in chemical fermentation processes. Besides, water jet is useful for oxygenation because of its simplicity in construction and operation (Baylar et al., 2006), efficient mixing (Giger et al., 1991), and minimal energy requirements (Biń, 1993). Apart from the industrial applications, understanding plunging jet air entrainment is important because it plays a significant role in oxygenation of waterbodies. Breaking waves in ocean, two-dimensional jets downstream of spillways, plunging wavefronts formed by moving water vessels are examples of air-entrainment in waterbodies by plunging jets.

A significant number of studies have been conducted on the air entrainment by stationary plunging jets in quiescent waterbodies. Key findings of these studies can be found in the reviews of Biń (1993), Chanson (1996), and Kiger and Duncan (2011). In contrast, studies related to translating plunging jets are rare. The reason could be the complexity in experimental measurements for translating jets. One of the easiest settings for such experiments would be experimenting with a stationary plunging jet in a crossflow (e.g., Jahromi and Khiadani, 2017). However, there are several drawbacks of conducting experiments in crossflows rather than with translating jets. Firstly, the translating jet is subject to air drag before it plunges into the waterbody, which increases surface disturbance and enhances air entrainment in jet surface. Secondly, the vertical velocity distribution of the crossflow is not usually uniform in the experimental setup, whereas a translating

jet can be moved at a uniform velocity. Despite scarcity of the studies of air entrainment by translating jets, it is important in many practical problems, like plunging breaking waves (Chanson and Lee, 1997), and plunging bow waves of hydraulic vessels at high speed (Gómez-Ledesma et al., 2011).

Contemporary knowledge on stationary plunging jets is inadequate to explain the characteristics of air entrainment by translating plunging jets. Chirichella *et al.*, (2002) conducted laboratory experiments with translating plunging laminar jets to study the air entrainment mechanism and determined the boundary between different entrainment regimes. They started experiments with stationary jets with no air-entrainment. As the jets started moving horizontally, air entrainment commenced at a certain flow condition. However, for turbulent stationary jets, it is usually common to observe air entrainment even at very low jet velocity, since air entrainment is a function of the relative turbulence of the jet at the nozzle (Ervine et al., 1980; Oğuz, 1998). Therefore, the incorporation of translating velocity to a turbulent plunging jet may increase air entrainment, and the mechanism could be different from a laminar translating jet.

Another aspect of the translating jet is that its trajectory bends over to the opposite direction of jet translation, similar to a jet in crossflow. It is known that a jet in crossflow bends over and produces a counter rotating vortex pair (Rajaratnam and Gangadharaiah, 1983). It is unknown yet, but will be interesting to know whether and how the bubble swarm produced by a translating jet is affected by the vortices. Further, self-similarity of the bubble characteristics (i.e., bubble frequency, void fraction, bubble velocity, etc.) was observed for stationary plunging jets (e.g., Chanson and Manasseh, 2003). Study on the self-similarity for bubbles produced by translating jets is required as well.

With respect to the bubble size in an air-water system, the general consensus is that the Sauter mean diameter, D_{32} ($D_{32} = \sum D_b^3 / \sum D_b^2$, where D_b is bubble diameter) of the rising bubbles is independent of the jet velocity and diameter (Biń, 1993). The distribution of bubble sizes can be typically represented by a log-normal distribution, skewed to the smaller bubble diameters (Evans, Jameson and Atkinson, 1992). The Sauter mean diameter and the distribution of bubble sizes for the case of translating plunging jets are not well-understood. Moreover, Maxworthy et al. (1996) reported that the rising velocity of a bubble is a function of the bubble diameter, considering the

properties of the inter-acting fluids remain constant. However, the change of the mean rising velocity of a bubble swarm is practically insignificant for stagnant water and typically considered as constant; whereas in crossflow, this velocity is considerably lower (Barczewski et al., 1975). Therefore, it is necessary to study the effect of the translating velocity on the mean rising velocity of bubble swarm produced by a translating jet.

For the maximum penetration depth of bubbles entrained by stationary plunging jets, comprehensive studies were conducted previously, and theoretical development was done based on the assumption that at the maximum penetration depth, the local velocity of the submerged jet is equal to the free rising velocity of the bubble (Ervine and Falvey, 1987; Guyot et al., 2019). Due to the bending over of the translating jet, the local jet velocity is expected to equalize with the bubble rising velocity at a smaller depth. Further, as stated before, the mean rising velocity of the bubble swarm gets affected by the crossflow, and probably by the translating velocity of the jet as well. Therefore, a hypothesis for translating plunging jet is that the maximum penetration depth is smaller than the case of stationary jet, providing that other hydraulic conditions and fluid properties remain the same.

This study is probably the first experimental work on air entrainment by translating turbulent plunging jets. The mechanism of air entrainment, bubble size distribution, rising velocity, maximum penetration depth of bubbles, trajectory of the bubble swarm, and void fraction are analyzed using a high-speed camera, and the results are compared with the literature on stationary plunging jets. This study improves the understanding of the characteristics of bubbles entrained by translating turbulent jets, and helps building computational fluid dynamics models for further investigation on this topic.

5.2 Experiments

5.2.1 Experimental Setup

The experiments were carried out in the T. Blench Hydraulics Laboratory of the University of Alberta in Canada. Figure 5.1 shows the sketch of the experimental setup. The experiments were conducted inside a 10 m × 0.8 m × 0.8 m towing tank with plexiglass walls for visualization. The tank is equipped with a carriage on top, which moves along the length of the tank. The carriage is

computer-controlled and translates horizontally at a maximum velocity of 0.84 m/s. A 1 m long and 25 mm diameter PVC pipe is attached to the carriage vertically with a circular nozzle at the bottom end and a flexible hose at the top end of the pipe. A centrifugal pump is attached to the flexible hose and the towing tank. It pumps out water from the towing tank and injects through the nozzle, thus recirculates the same water during experiments. A valve attached to the pump controls the flowrate at the nozzle, which can be measured using a magnetic flowmeter. Water depth in the towing tank was kept at a constant depth of 0.5 m for all experiments. A high-speed camera (Phantom v211, Vision Research, Wayne, New Jersey) was attached to the carriage at one side of the tank which moved with the jet at the same translating velocity. The camera was equipped with a Nikon lens (Nikon AF Micro NIKKOR 60 mm f/2.8D). A fixed light source is used on the other side of the tank for back-lighting. The camera takes images of the jet impingement and entrainment of air bubbles using shadowgraph technique (Settles and Hargather, 2017). It was set to take images of resolution 1280×800 pixels, with a sample rate of 2000 frames per second at an exposure time of 150 μs.

Table 5.1 summarizes the flow conditions of the experiments. The selection of the range of the experimental parameters were based on the limitations of the experimental setup. Three different circular nozzles with diameters, d = 6.3, 7.9, and 12 mm; impinging height, h = 20 to 360 mm; jet velocity at nozzle, V_j = 3.21 to 9.62 m/s; and translating velocity of the jet, U_t = 0.16 to 0.84 m/s were used in the experiments. Considering free fall, the jet velocity at the impact with the water surface can be measured as follows,

$$V_i = \sqrt{V_j^2 + 2gh}$$

(5.1)

where g is acceleration by gravity. Based on Equation 5.1, V_i in the experiments ranged from 3.27 to 9.64 m/s. Note that V_j and V_i do not vary much for smaller h, wherease they are quite different for a large h. For example, for h = 360 mm, V_j and V_i are 3.21 and 4.17 m/s, respectively. The ratio of jet impact velocity to translating velocity R_{it} ranged from 4 to 40 in different experiments. In test series A to E, U_t was varied within each series. Test series A to C have same d and different Q, while test series D and E have different d. Test series F was conducted to study the effect of Q for a constant U_t. Lastly, test series G was carried out to study the effect of h for a constant U_t.

5.2.2 Measurement Techniques

For the experiment with $D = 6.3$ mm, $h = 20$ mm, $V_i = 3.27$ m/s, and $U_t = 0.42$ m/s, two images captured on two different times were compared to see if there is any difference in bubble size distribution. It was found that the bubble size distributions from different images of the same experiments were similar. Therefore, A single image was used from each experiment to measure the bubble size. ImageJ software (Schneider et al., 2012) with "Analyze Particles" tool was used to measure the bubble size automatically for experiments with a small number of bubbles in the image, i.e., experiments with translational velocities 0.16 and 0.27 m/s. However, for higher translational velocities like 0.42, 0.58, and 0.84 m/s, automatic particle detection does not work well because a large number of bubbles overlaps in the field of view. Therefore, for those cases, ImageJ "Line" tool was used to manually measure the bubble diameter. Nevertheless, for both automatic and manual bubble measurement techniques, more than 200 bubbles were measured in each case to get a reliable and representative frequency distribution histogram of bubble diameter.

For the measurement of spatial distribution of bubbles, 1000 images were used for each experiment. First, the images were converted into binary images using a code written in Matlab. The bubbles could be easily identified in the binary images. Then another code was written to invert the colors of water and air bubbles and to average the intensity of 1000 images. The resulting averaged image represents the distribution of the bubbles in the scale of 0 to 1, where 0 and 1 represent 100% water and 100% air, respectively. Figure 5.2 shows the processed images at different steps of this method for an experiment of test series A with $U_t = 0.42$ m/s. It should be noted that this spatial distribution is also a measure of the probability of bubble occupancy in the bubble swarm image. Although it does not provide the actual void fraction along a section, but it can be regarded as an indirect measurement of void fraction obtained from shadowgraph images.

The trajectories of the bubble swarm are measured using the intensity-averaged image for bubble distribution (Figure 5.2c). The line connecting the pixels with peak intensities in the central region of the bubble swarm is identified as the axis of the bubble plume. The bubble penetration depth of the plume is identified as the vertical distance from the water surface to the lowest point of the of the bubble plume boundary, while the longitudinal length of the plume is defined as the horizontal distance from the jet impingement point to the upstream location of the water surface where the most distant water bubble rises.

Initially, the measurements of the velocity field of the bubble swarm was conducted using the particle image velocimetry (PIV) technique. A continuous 6W Argon-ion laser with a wavelength of 488 nm (Stabilite 2017, Spectra Physics) was used with optics (OZ optics) to generate a light sheet. The flow field was illuminated with the laser sheet and the images were captured with the high-speed camera. However, PIV did not work well because of the scattering of the laser sheet by the air bubbles. Further, applying the particle tracking velocimetry (PTV) technique on the shadowgraph images is not practical since the bubble density is higher for higher jet translating velocities and it is difficult to optically identify individual bubbles. Therefore, the bubble image velocimetry (BIV) technique introduced by Ryu et al. (2005) for highly aerated bubbly flow is used in this study with the shadowgraph images obtained using backlight. This technique has been used in many air-water flow problems for the measurements of velocity fields including studies on the plunging breaking waves (Lim et al., 2015) and jet bubbling reactor (Shuai et al., 2019)). In BIV, bubbles are used as tracers and the texture of the images gives the correlation for velocity measurements. The images are analyzed using with an open-source software, PIVlab (Thielicke and Sonntag, 2021). Figure 5.2d shows a typical velocity field of bubble swarm using BIV technique.

5.3 Results and Discussions

5.3.1 General Observations

Figure 5.3 shows the bubble swarm at different translating velocities for test series A. The jet forms a cavity at the point of impact, and the cavity grows in size with the increase of translational velocity. Eventually parts of the cavity detach and generate air bubbles due to the turbulence induced by the translating jet. As the translational velocity increases, the number of bubbles was observed to increase until $U_t = 0.58$ m/s. However, at the maximum translational velocity of $U_t = 0.84$ m/s, number of bubbles was seen to decrease from $U_t = 0.58$ m/s. With the increment of the translational velocity, the bubble swarm elongates longitudinally, and the depth of penetration of bubbles reduces. The bubble size also appears to grow bigger with translational velocity. Further, at higher translational velocities, the bubbles are seen to move in lumps, rather than moving individually. These characteristics will be discussed in details in the following sections.

72

5.3.2 Mechanism of Air Entrainment

Figure 5.4 shows the impingement of the jet at different translating velocities for test series A. At translational velocities U_t = 0.16, 0.27, and 0.42 m/s, capillary waves are observed downstream of the jet with measured wavelengths of 6.7, 5.9, and 1.8 mm, respectively. As the translational velocity increases, the wavelength decreases. At higher translation velocities, i.e., U_t = 0.58 and 0.84 m/s, the capillary waves become too small to measure from images. A surface depression or cavity, followed by a wake region and gravity-capillary wavetrain can be seen upstream of the jet, similar to the observation made by Chirichella et al. (2002) for laminar translating jets. This gravity-capillary wavetrain in the wake region moves closer to the jet as the translational velocity increases.

To understand the air entrainment process of a translating turbulent jet, observations were made on the same jet at stationary condition first, and later at different translating velocities (Figure 5.3 and 4). For the stationary jet at an impact velocity V_i = 3.27 m/s and Weber number We = 935, the jet is a weakly disturbed jet with visibly rough surface. Due to the perturbations on the jet surface, the meniscus of the water surface surrounding the jet is observed to go below the initial undisturbed water surface. It forms an annular ventilated cavity surrounding the jet, similar to the observations of Cummings and Chanson (1997). This annular cavity frequently expands in the form of fingers or stems and transiently entrains air bubbles. Although it may seem that the air cavity surrounding the jet causes air entrainment, Kiger and Duncan (2011) suggested that the instability of the jet surface may be responsible for this. Oğuz (1998) also reported that the jet surface disturbance is the principle factor of such air entrainment.

For U_t = 0.16 and 0.27 m/s, and velocity ratios R_{it} = 20 and 12, the upstream meniscus remains under initial water surface, similar to a stationary jet. This facilitates air entrainment in both upstream and downstream direction of the jet. Subsurface images shows that air entrainment occurs continuously from the cusp of the downstream cavity and upstream meniscus of the jet (Figure 5.3).

For higher translational velocities U_t = 0.42, 0.58, and 0.84 m/s, and velocity ratios R_{it} = 8, 6, and 4, respectively, the meniscus at the upstream of the jet forms above the initial water surface. The radius of curvature of the meniscus decreases as the translational velocity increases. Since the

upstream meniscus is above the initial water surface at higher U_t, no entrapped air can be seen between the jet and the meniscus. The cavity is continuously forming a vortex with the translating jet inside, and air entrains continuously by the vortex of the cavity.

Depending on the translating velocity and the characteristics of the upstream meniscus, air entrainment for a translating turbulent jet can occur either in the cusp of the cavity or both in the cusp and meniscus. However, (Chirichella *et al.*, 2002) observed that for a laminar translating jet with $d = 6$ mm, $V_i = 3.03$ m/s, and $U_t = 0.32$ to 0.44 m/s, air entrainment occurs at the cusp only, since the upstream meniscus is formed above the initial water surface.

The air entrainment in the upstream inverted meniscus can be either due to the low pressure resulted from the entrainment of the surrounding fluid into the submerged jet, or entrained air in the boundary layer of the jet itself before it impinges in the pool (Biń, 1993). The former was likely to be the case in this study since the jet is only weakly disturbed. The mechanism of air entrainment in the cavity can be explained by the *intermittent vortex* mechanism- described by McKeogh and Ervine (1981), which explained air entrainment by a stationary jet when the jet is in transition between the laminar and turbulent conditions. As the translating jet impinges into the pool, an axial vortex formed surrounding the jet, and the combined effects of low pressure in the vortex core and jet entrainment creates a deep cavity. Due to the translation of the jet, the cavity moves to the downstream wake region and air bubbles continuously emanate from the cusp of the cavity.

5.3.3 Vortex Shedding by the Translating Jet

Figure 5.5 shows the instantaneous unsteady behavior of the bubble swarm. At the windward side of the cavity, shear-layer vortices are observed. These are similar to Kelvin-Helmholtz rollers observed in regular jets in crossflow (Mahesh, 2013), and highly unsteady in nature. At the leeward side, regular coherent structure of the bubble swarm is observed, especially for $U_t = 0.42$ m/s. Considering the distance between two consecutive structures represents the wavelength of the vortex shedding (λ), the frequency of the shedding can be calculated by

$$f = \frac{U_t}{\lambda} \tag{5.2}$$

The characteristics of the vortex shedding can be represented by a dimensionless parameter,

Strouhal number

$$S_{tr} = \frac{f D_j}{U_t} \qquad (5.3)$$

For d = 6.3 mm, V_i = 3.27 ms^{-1}, and h = 20 mm, the calculated Strouhal numbers for U_t = 0.42, 0.58, and 0.84 m/s are 0.27, 0.22, and 0.25, respectively. Since the impinging height is relatively small (h/Dj ≈ 3), the jet diameter doesnot change much before it impacts on the water surface. For circular cylinders in crossflow, the Strouhal number typically ranged between 0.2 to 0.3 (White, 2011). Therefore, S_{tr} for translating jets found comparable to the case of circular cylinder in crossflow.

5.3.4 Bubble Diameter

For bubble entrainment by a plunging liquid jet in a quiescent pool, two distinct regions are identified (Biń 1993). The first region consists of fine bubbles with diameters less than 1 mm forming a biphasic conical region, and the second region consists of rising bubbles of bigger diameters surrounding the first region. For translating plunging jets, it is difficult to observe these two regions distinctively. Due to the translation of the jet, these regions become skewed to the opposite direction of jet translation. The longitudinal spread of these regions depends on the translating velocity of the jet. Coalescence of smaller bubbles to bigger bubbles occurs in the transition zones of first to second regions.

Fig.6 shows the entrained air bubbles for the same plunging jet with U_t = 0.16 to 0.84 m/s (test series A). All the image slices are in the same scale and show the same location inside the towing tank. This figure shows that the bubble shape varies from the regular spherical or ellipsoidal shape as the translating velocity increases. Further, the average size of the bubble can be seen to increase with U_t as well. To understand the distribution of bubble size, the probability density distributions of bubbles are analyzed for different jet impact and translating velocities. Similar to the observations of Chanson (1997), a log-normal distribution is found to be the best fit for bubble size distribution, skewed towards the smaller diameters. Equation 5.4 gives the probability density distribution of the bubble sizes,

$$P_D = \frac{1}{D_b \sigma \sqrt{2\pi}} \exp\left\{\frac{-(\ln D_b - \mu_b)^2}{2\sigma_b{}^2}\right\} \tag{5.4}$$

where D_b is the bubble diameter, and σ_b and μ_b denote the log standard deviation, and logarithmic mean of the bubble diameters, respectively. For the bin width of the distribution, the Freedman-Diaconis rule (Freedman and Diaconis, 1981) is used,

$$\text{Bin width} = 2\left(\frac{IQR(D_b)}{\sqrt[3]{n}}\right) \tag{5.5}$$

where $IQR(D_b)$ is the interquartile range of D_b, i.e., the spread of the middle-half of the distribution; and n is the number of measurements of D_b.

The probability density distributions of the bubble size for test series A (V_i=3.27 m/s), B (V_i=4.85 m/s), and C (V_i=6.45 m/s) are shown in Figure 5.7. The diameters of the bubbles range from 0 to 9 mm, with the peaks between 0.5 to 1.5 mm. However, for comparison purpose, bubble sizes in Figure 5.7 are shown in the range of 0 to 5 mm.

For any jet impact velocity, the peaks of the distributions show a similar trend, slowly increasing with the increase of the translating velocity from $U_t = 0.16$ to 0.58 m/s, and then decreasing as U_t is approaching 0.84 m/s. At $U_t = 0.84$ m/s, some of the bigger bubbles break down to smaller bubbles due to the turbulence induced by the jet translation. Evans et al. (1992) reported that the size of the bubble is a consequence of the balance of forces induced by the turbulence and surface tension of the liquid, and assumed that the bubble splits at a critical ratio of these quantities, i.e., the Weber number. This explains why the bubbles get smaller from $U_t = 0.58$ to 0.84 m/s. Further, the distributions are narrower for $U_t = 0.16$ and 0.27 m/s, while wider for $U_t = 0.42$ to 0.84 m/s. This indicates that the smaller translating velocities of the jet produce more uniform bubble sizes compared to the bigger ones.

Figure 5.8 shows that the Sauter mean diameter of the bubble changes with the translating velocity of the jet as well. D_{32} reduces from 3.8 to 1.8 mm for $R_{it} = 8$ to 21. However, for stationary jets, D_{32} ranged between 3 to 4 mm, irrespective of the jet velocity and nozzle diameter (Biń, 1993). For translating jets, the change of the Sauter mean diameter for different impact velocities becomes significant for $R_{it} \leq 11$. For aerated bubbly jets in a crossflow Zhang and Zhu (2013) also reported that D_{32} reduces with increasing R_{it}. However, they have only used one crossflow velocity of 0.20

m/s, and as such the effect of the crossflow velocity was not investigated. For R_{it} = 15 to 25, D_{32} in their experiments varied between 1.77 and 2.79, which are comparable to the observations of this study. Interestingly, in the study of Zhang and Zhu (2013), the bubble sizes drastically got bigger for R_{it} < 15, similar to this study.

5.3.5 Maximum Penetration Depth and Trajectory of the Bubble Plume

We hypothesize that the maximum penetration depth for a translating jet depends on the usual parameters of the case of a stationary jet, in addition to the jet translating velocity. Therefore, for the maximum penetration depth, one can write

$$H = f_1\{H_0, U_t\} \tag{5.6}$$

$$\text{where } H_0 = f_2\{D_j, g, \rho_w, \mu_w, \sigma_w, V_i\} \tag{5.7}$$

In Equation 5.7, H_0 is maximum penetration depth jet at stationary condition. The effect of air properties, i.e., density, and viscosity are neglected in this analysis. The jet plunging height h is not considered since the impact velocity V_i is a function of h, and V_i is already included in Equation 5.7. Further, it was made sure that for the experimental range of h in this study, the jet does not breakup before plunging on the water surface. Numerous non-dimensional relations can be derived from Equation 5.6 and 5.7. To understand which dimensionless parameters are relevant to this problem, first the functional relations between H and d, H and V_i, and H and U_t are explored using plots of the corresponding variables.

Considering the translating velocity (U_t) remains constant, Figure 5.9a shows that the maximum penetration depth of bubbles (H) increases linearly with the increase of the jet diameter (d). Similarly, Figure 5.9b shows that H increases linearly with the increase of the impact velocity (V_i), for the same translating velocity (U_t). However, H decreases with the increment of the translating velocity for the same V_i and d, but the relation is non-linear. Figure 5.9c shows that H increases linearly with the increase of $1/\sqrt{U_t}$. This is because at higher translating velocity, the trajectory of the jet moves closer to the water surface – a phenomenon similar to jets in crossflow, where the jet trajectory moves closer to the jet-issuing boundary (Morton and Ibbetson, 1996).

Now, from Equation 5.6 the following dimensionless expressions can be derived based on the plots at Figure 5.9a, 9b and 9c,

$$\frac{H}{H_0} = C_1 \sqrt{R_{it}} \tag{5.8}$$

$$\frac{H}{D_j} = C_2 \sqrt{R_{it} Ca} \tag{5.9}$$

where C_1, and C_2 are empirical coefficients. C_1 depends on the nozzle characteristics. For $d = 6.3$ mm, value of C_1 is estimated as 0.116. C_2 depends on the liquid property and estimated as 33.3. Lastly, $Ca = \mu_w V_i / \sigma_w = We/Re$, is the Capillary number of the air-water interface for the corresponding jet impact velocity. Kiger and Duncan (2011) reported that the Capillary number influences the onset of air entrainment in both viscous and low-viscosity (air-water) system. Therefore, it makes sense that the Capillary number also impacts the maximum air bubble penetration depth. Equation 5.9 reveals that the maximum penetration depth of bubbles for a translating plunging jet depends on the relative jet velocity as well as the inter-action between the viscous drag force and surface tension of the gas-liquid interface.

Fig 10a shows the trajectory of the plume axis for different impinging and translating velocities for $d = 6.3$ mm and $h = 20$ mm. It can be observed that for any impact velocity, the maximum depth of the trajectory increases with translating velocity. This has been discussed previously for bubble penetration depth. However, the longitudinal length of the trajectory does not follow similar trend. Rather the length of the longitudinal trajectory follows this order for different translating velocities: $U_t = 0.84, 0.27, 0.16, 0.58,$ and 0.42 m/s. A general equation of the trajectory is developed by scaling the x distances with the horizontal length of the trajectory x_m, and y distances with the maximum vertical depth of the trajectory y_m (Figure 5.10b),

$$\frac{y}{y_m} = 2.45 \left(\frac{x}{x_m}\right)^3 - 6.76 \left(\frac{x}{x_m}\right)^2 + 4.08 \left(\frac{x}{x_m}\right) + 0.32 \tag{5.10}$$

Previous researchers, including Zhang and Zhu (2013), reported separation of the bubble plume trajectory from the water-jet due to the rising velocity of the bubble. Therefore, the bubble plume trajectory would be different from the water-jet in a crossflow. A water-jet in crossflow typically can be characterized by a power expression, which is a function of the velocity ratio R_{it} (see Rajaratnam, 1976). However, a polynomial expression is necessary to characterize a bubbly plume in crossflow as the plume bends over and releases to the water surface, unlike a submerged water-

jet in crossflow of water, as it bends over and becomes parallel to the crossflow.

5.3.6 Spatial Distribution of Bubbles

From the intensity-averaged images as the one shown in Figure 5.2c, several sections perpendicular to the axis are extracted. η is the transverse distance from the plume axis. These sections give the profiles of the probability of bubble occupancy (α_b) at 9d, 14d, 19d, and 24d distances along the axis of the bubble plume for d =6.3 mm, h = 20 mm, V_i = 3.27 m/s and U_t = 0.27 to 0.84 m/s (Figure 5.11a). The maximum probability of bubble occupancy in the distribution is defined as α_{bm}. Figure 5.11a shows that along the plume axis α_{bm} decreases as the distance from the jet impact increases. In Figure 5.11b, α is scaled with α_{bm}, and η is scaled with η_{50}, where η_{50} is the value of η where $\alpha_b = 0.50\ \alpha_{bm}$. The dimensionless profiles collapse into a single dimensionless profile, and can be expressed as a Gaussian distribution,

$$\frac{\alpha_b}{\alpha_{bm}} = \exp\left\{-0.693\left(\frac{\eta}{\eta_{50}}\right)^2\right\} \tag{5.11}$$

Equation 5.11 fits the spatial distribution of bubbles well, except for $U_t = 0.27$ m/s. This is because the number of bubbles in this case is sparse (see Figure 5.3), which makes it difficult to assess spatial distribution reliably for lower translating velocities. Nevertheless, Equation 5.11 is similar to the expression for void fraction reported for bubbly jets in crossflow (Zhang and Zhu, 2013), for bubbly jets in stagnant water (Neto et al., 2008a), and for horizontal bubbly jets in a quiescent water tank (Neto et al., 2008b). Therefore, no obvious effect of the jet translation can be realized on the spatial distribution of bubbles along sections perpendicular to the bubble plume.

5.3.7 Kinematics of the Bubble Swarm

For the BIV analysis, ensemble correlation technique is used with 400 images for each analysis. This is because the regular PIV algorithm often fails to detect the correct displacement and averaging the displacement for multiple image pairs may not enhance the robaustness of the analysis (Thielicke and Sonntag, 2021). Fig 12a shows the results of the BIV analysis for $U_t = 0.42$ m/s. The correlation matrix for most of the bubble swarm region is significant, especially in the region after the bubble pinches off from the cavity formed by the translating jet. This indicates the velocity field in this region can be obtained reliably. The vortex locator plot does not show much active vortices in the projection plane, except few near the edge of the bubble plume and around

the air cavity. This is consistent with the observation of the high-speed camera video.

The u-velocity plot shows that for most the bubble swarm region, the u-velocity component varies between 0.40 and 0.45 m/s, which is expected because the frame of reference is moving with the jet carriage at 0.42 m/s. The bigger u-velocity region near the bottom edge of the bubble swarm has some uncertainty due to small correlation. Nevertheless, this region indicates the effect of the jet velocity on the bubble motion. As observed in previous studies (Zhang and Zhu, 2013), the submerged jet trajetory detaches from the bubble plume trajectory after some distance in the crossflow. Before and after a short distance of the detachment location, the bubble plume is affected by the jet velocity, and hence the u-velocity component is bigger there.

The v-velocity component is initially downward as the bubbles travel with the jet. Later the bubbles move upwards due to buoyancy and v-velocity component becomes upward. Near the water surface the v-velocity component is between 0.20 to 0.35 m/s. Maxworthy et al., (1996) reported that the terminal rising velocity of individual bubbles depends on the Morton number (Mo = $g\mu_w^4\rho_w^{-1}\sigma_w^{-3}$), and bubble diameter. They found that for any Morton number, the rising velocity increase from 0.22 to 0.36 m/s for a decrease of bubble diameter from 7 to 1.4 mm. Therefore, the v-velocity range obtained using the BIV analysis shows no obvious effect of the jet translation on the bubble rising velocity. The velocity magnitude plot in Figure 5.12a shows the combined effect of the u and v-velocity components. The higher velocity zone near the bottom of the bubble plume indicates the trajectory of the jet and detachment from the bubble plume.

Figure 5.12b shows the velocity field of the bubble plume at different translating velocities. As U_t increases from 0.16 to 0.84 m/s, the trajectory of the high velocity zone (water jet trajectory), along with the bubble plume trajectory become flatter. The magnitude of the velocity fields is observed to be the function of the translating velocity of the jet.

5.4 Summary and Conclusions

This paper presents an experimental study of air-bubble entrainment in stagnant water by translating turbulent circular jets. Jet diameters from 6.3 to 12 mm, jet plunging height from 20 to 360 mm, jet impact velocities from 1.72 to 9.64 m/s, and jet translating velocities from 0.16 to 0.84 m/s were considered to study the entrained bubble characteristics. The main conclusions of

this study are as follows:

1. Air-bubble entrainment by the translating turbulent jets occurs from the cavity formed by the jet impact. During the jet translation, the cavity continuously generates a rotating vortex with the translating jet inside. For translating velocities less than 0.27 m/s, air-bubble entrainment occurs at the cusp of the cavity and meniscus at the upstream contact location of the jet and water surface. For translating velocities greater than 0.42 m/s, air-bubble entrainment occurs at the cusp of the cavity only. Translating velocity between 0.27 to 0.42 m/s is characterized by the transition zone of air-entrainment mechanism.

2. At the windward side of the jet impact cavity, highly unsteady shear-layer vortices can be observed; while at the leeward side regular coherent structure of the bubble swarm can be observed. This coherent structure or vortex shedding is prominent for translating velocities 0.42 to 0.84 m/s, with Strouhal number ranged between 0.22 to 0.27. This is comparable with vortex shedding by circular cylinder in crossflow.

3. The probability distribution of the bubble size exhibits that the bubbles get bigger with the translating velocity up to 0.58 m/s, then the bigger bubbles start to break down due to the turbulence at the wake region of the jet. The peak of the bubble size distribution ranged between 0.5 to 1.5 mm. The Sauter mean diameter of the bubbles varies between 1.8 and 3.8 mm. This variation becomes significant for velocity ratio greater than 11.

4. The maximum penetration depth of bubbles for a translating jet depends on the velocity ratio and interaction between the viscous drag force and surface tension of the gas-liquid interface. Hence, this depth is a function of the velocity ratio and Capillary number. Further, the penetration depth for the translating jet can be expressed as a function of the velocity ratio and penetration depth for the stationary jet.

5. The trajectory of the bubble plume becomes flatter with the increase of the translating velocity. The dimensionless trajectories at different impact and translating velocities can be expressed with a general equation.

6. The spatial distribution of bubbles in the sections perpendicular to the bubble plume axis follows a Gaussian distribution. This is comparable to the void fraction of bubbly jets in crossflow.

7. For the reference frame moving with the jet carriage, the BIV technique reveals that the u-velocity component is mainly in the order of the jet translating velocity. Near of the bottom of the jet plume, both the u and v-velocity components are affected by the momentum of the water jet. The terminal rising velocity of the bubbles are between 0.20 and 0.35 m/s for the jet translating at 0.42 m/s, which is comparable to a jet at stationary condition. Therefore, no obvious effects of the jet translation can be realized on the terminal rising velocity.

The present study improves the understanding of air-bubble entrainment mechanism, characteristics and kinematics by translating turbulent jets. Further, it provides the first-of-its-kind valuable data for computational modeling of multiphase flow.

Table 5.1: Experimental flow conditions.

Test series	Q (L/s)	d (mm)	h (mm)	V_j (m/s)	V_i (m/s)	U_t (m/s)	R_{it} (-)	Re (-) × 10⁴	We (-) × 10³
A	0.1	6.3	20	3.21	3.27	0.16, 0.27, 0.42, 0.58, and 0.84	4 to 20	2.06	0.93
B	0.15	6.3		4.81	4.85			3.06	2.06
C	0.2	6.3		6.42	6.45			4.06	3.06
D	0.16	7.9		3.26	3.32			2.63	1.21
E	0.36	12		3.18	3.24			3.89	1.75
F	0.05, 0.1, 0.15, 0.20, 0.25, and 0.3	6.3	20	1.60 to 9.62	1.72 to 9.64	0.42	4 to 23	1.08 to 6.08	0.26 to 8.14
G	0.1	6.3	20, 75, 145, 280, and 360	3.21	3.27 to 4.17	0.42	8	2.06 to 2.62	0.93 to 1.52

Notes: Q: flow rate; d: jet diameter at nozzle; h: jet impinging height; V_j: jet velocity at nozzle; V_i: jet impact velocity; U_t: jet translating velocity; R: velocity ratio, $R_{it} = V_i/U_t$; Re = Reynolds number, Re = $\rho_w V_i d/\mu_w$, ρ_w is density of water, μ_w is dynamic viscosity of water; We: Weber number, We = $\rho_w V_i^2 d/\sigma_w$, σ_w is surface tension of water.
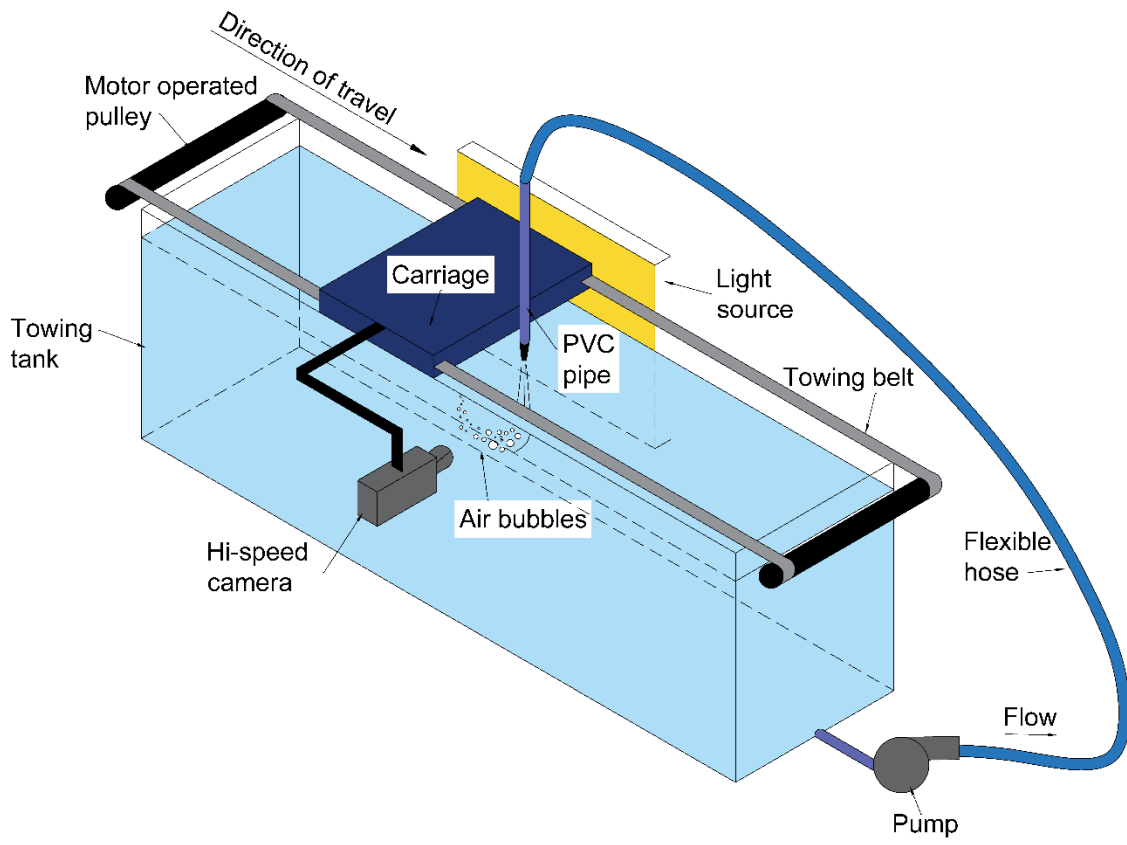
Figure 5.1: Schematic view of the experimental setup

(a)   (b)

(c)   (d)
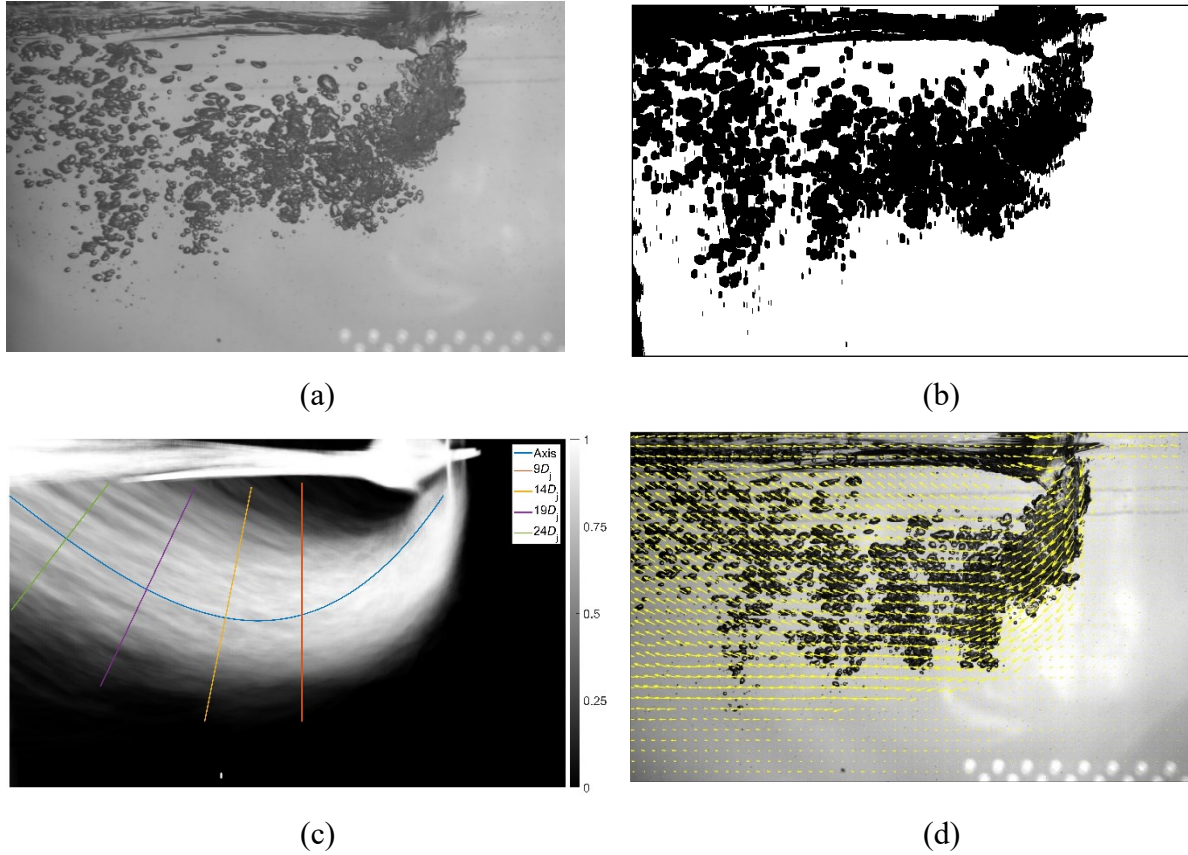
Figure 5.2: Image processing for spatial distribution of bubbles, swarm trajectory, and velocity field (a) original shadowgraph image, (b) binary image, (c) intensity-averaged image showing bubble distribution, plume axis, and sections at different distances ($9d$, $14d$, $19d$, and $24d$) from jet impact, and (d) velocity field of bubble swarm using BIV technique and ensemble analysis. For all the images, $d = 6.3$ mm, $h = 20$ mm, $V_i = 3.27$ m/s, and $U_t = 0.42$ m/s.
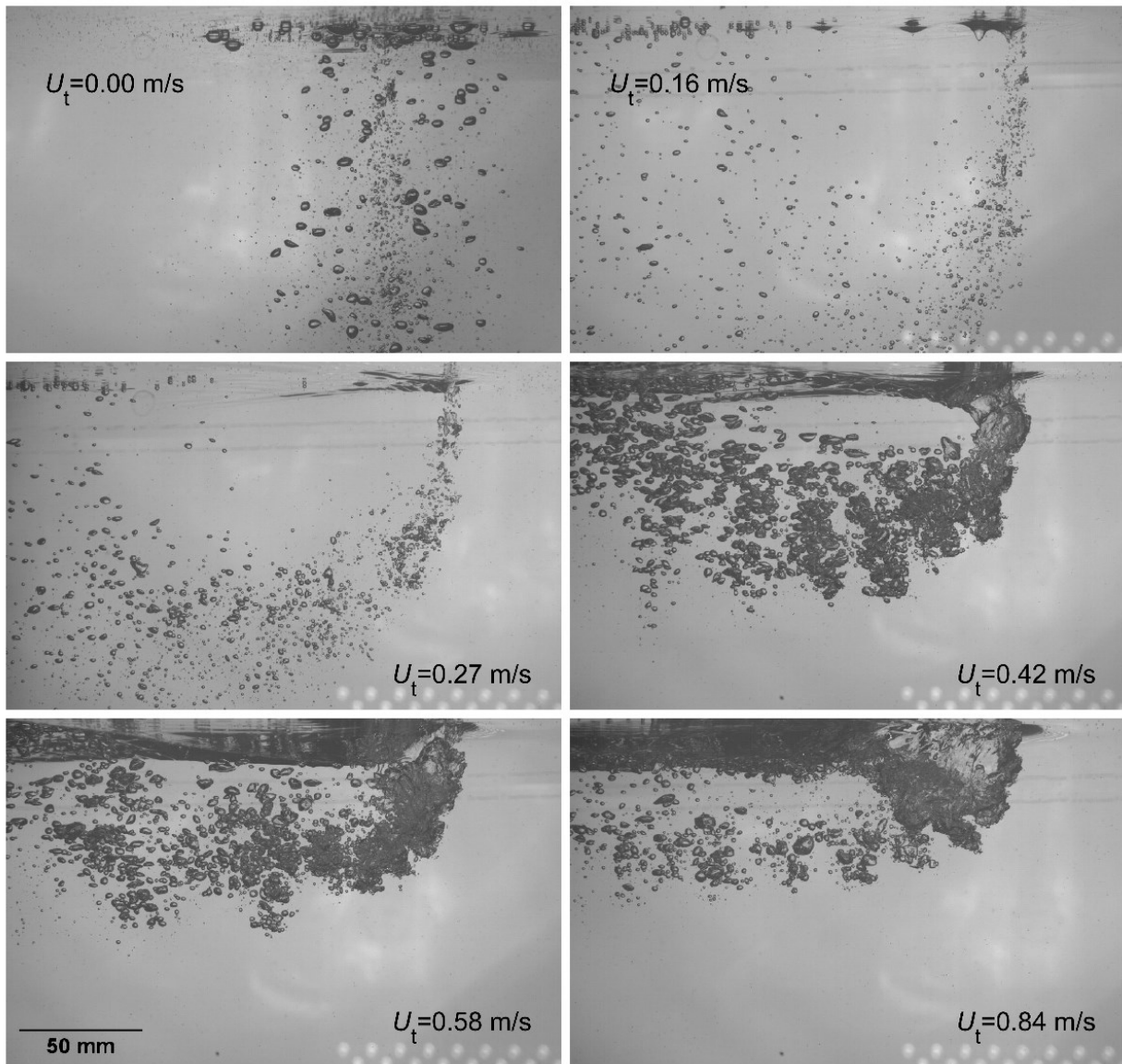
Figure 5.3: Shadowgraph images of bubble swarm at different jet translational velocities for $d = $ 6.3 mm, $V_i = 3.27$ m/s, and $h = 20$ mm. The jet is translating to the right.

Labels in figure:
U_t=0 m/s
U_t=0.16 m/s
U_t=0.27 m/s
U_t=0.42 m/s
U_t=0.58 m/s
U_t=0.84 m/s

Free-surface vortices
Capillary waves
Cavity
Gravity-capillary wavetrain
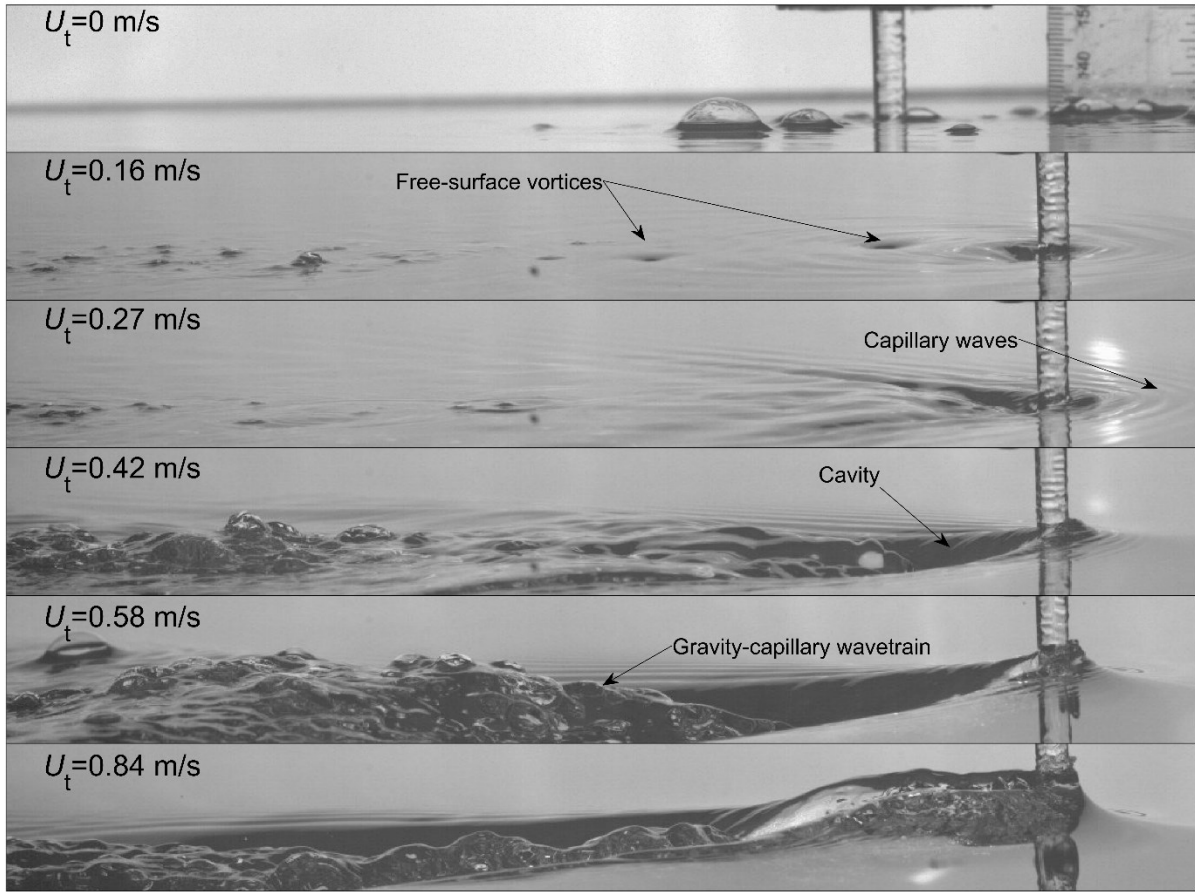
(a)

Figure 5.4: Water surface characteristics at the impact of the jet at different translational velocities, d = 6.3 mm, V_i = 3.27 m/s, and h = 20 mm; (a) side view with the jet translating to the right; (b) top view with the jet translating upwards.

U_t=0.16 m/s U_t=0.27 m/s U_t=0.42 m/s

Free-surface vortex

Jet edge

U_t=0.58 m/s U_t=0.84 m/s
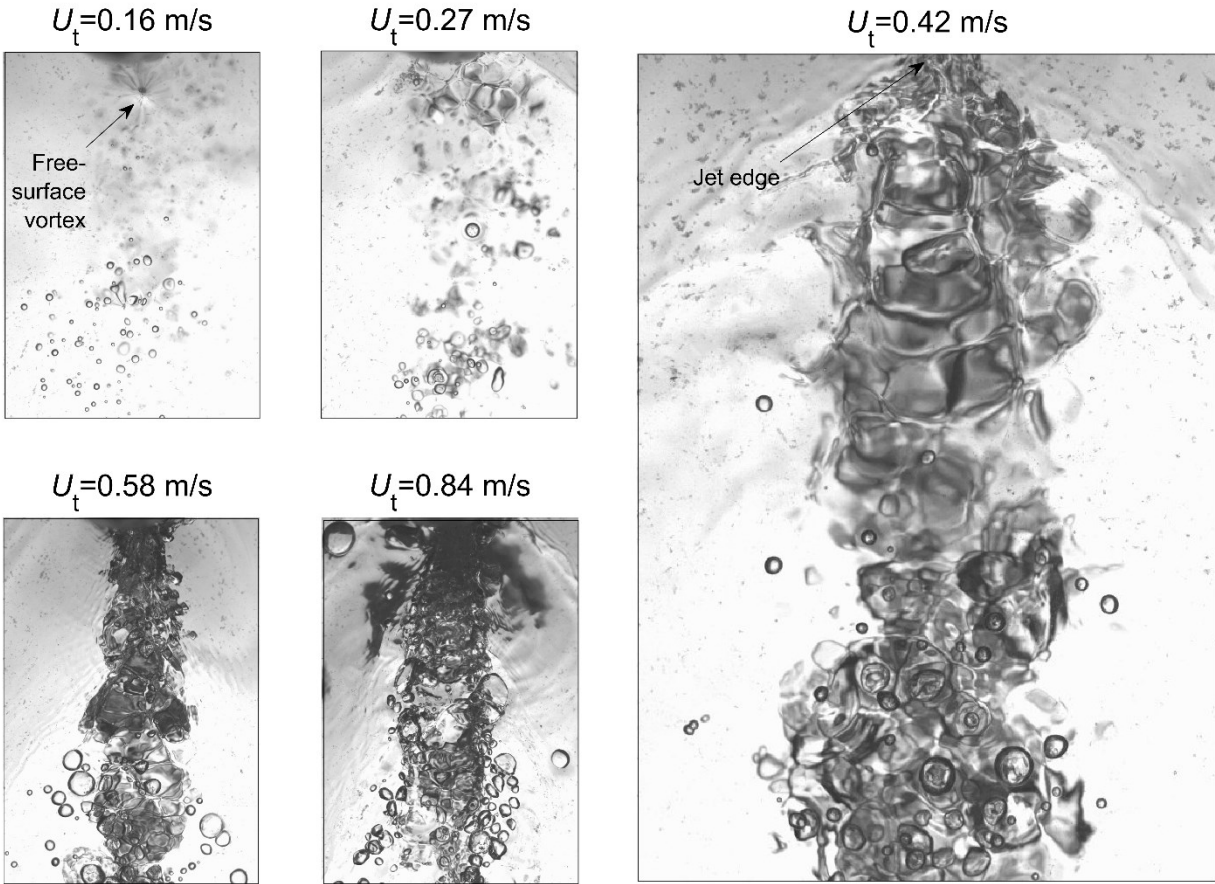
(b)

Figure 5.4: Cont'd.
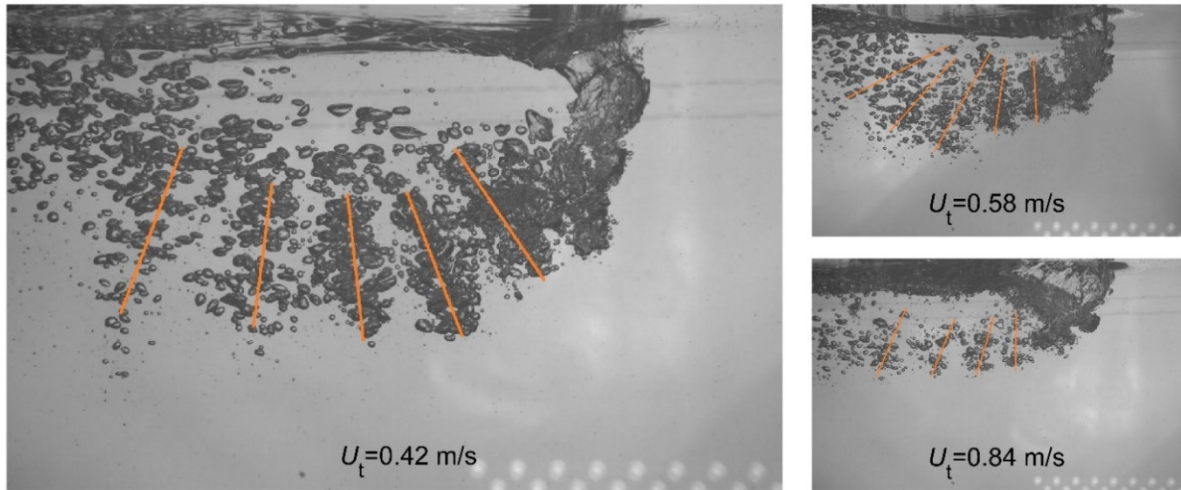
Figure 5.5: Three-dimensional vortex shedding in bubble swarm. $d = 6.3$ mm, $V_i = 3.27$ m/s, and $h = 20$ mm. The jet is translating to the right.
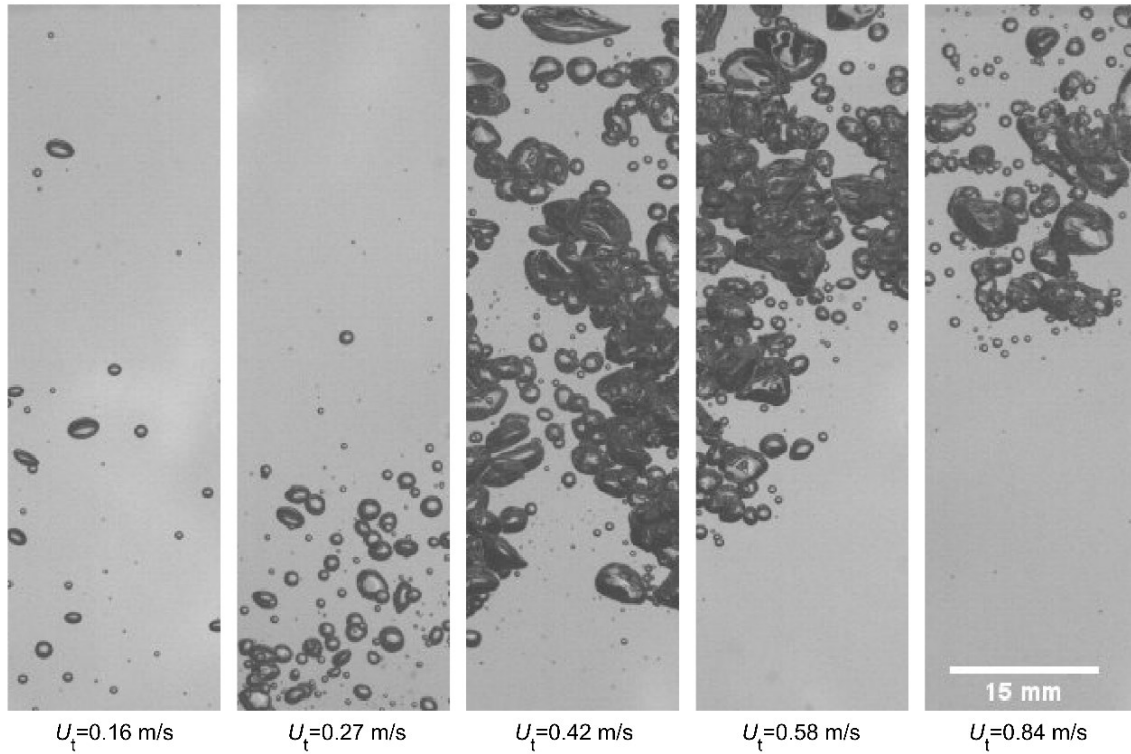
Figure 5.6: Entrained air bubbles at different translational velocities for the same jet ($d = 6.3$ mm, $V_i = 3.27$ m/s, and $h = 20$ mm). Image centers are located at $12d$ depth below the water surface and $10d$ distance upstream of the jet nozzle. Each image slice is 21 mm by 70 mm.
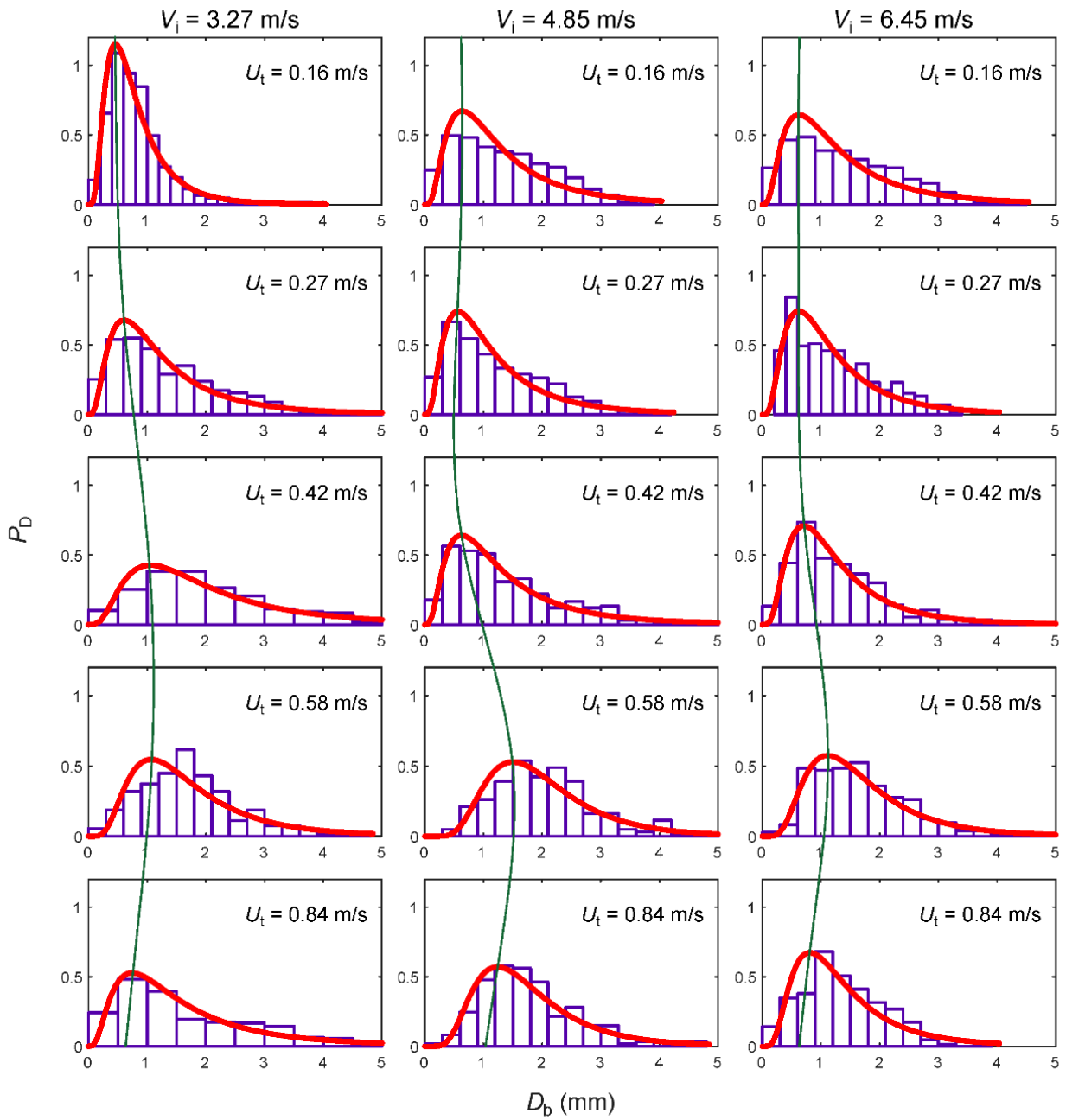
Figure 5.7: Bubble size distribution for different jet impact and translating velocities. $d = 6.3$ mm, and $h = 20$ mm. Green lines represents the trend of the peak of the distribution.
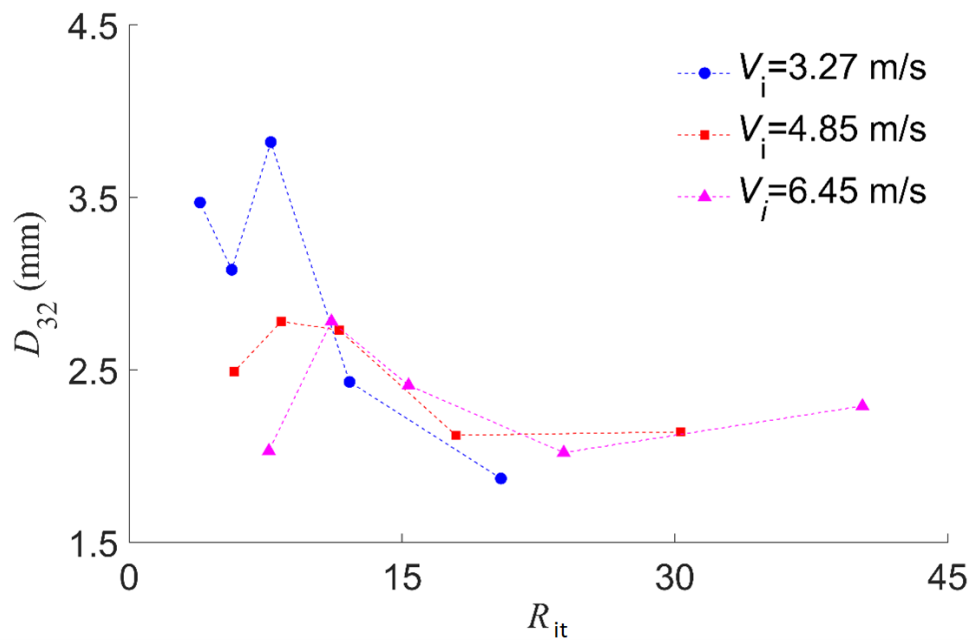
Figure 5.8: Sauter mean diameter of the bubbles as a function of jet translating velocity. $d = 6.3$ mm, $h = 20$ mm. Variation in D_{32} becomes significant for $R_{it} \leq 11$.
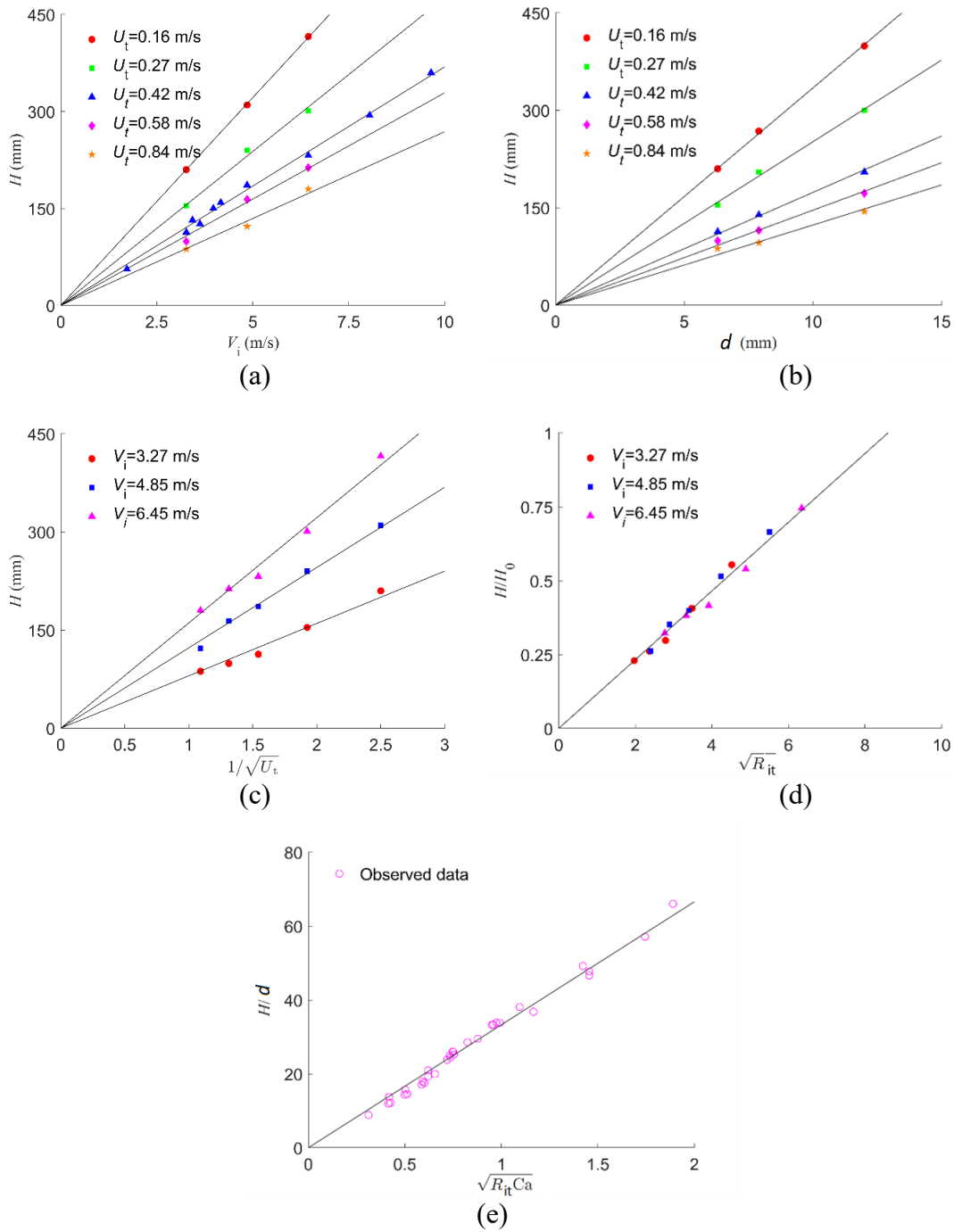
Figure 5.9: Maximum penetration depth of bubble swarm by translating jet (a) H as a function V_i for $U_t = 0.16$ to 0.84 m/s, $d = 6.3$ mm; (b) H as a function of d, for $U_t = 0.16$ to 0.84 m/s, $V_i = 3.27$ m/s; (c) H as a function of U_t for $V_i = 3.27$ to 6.45 m/s, $d = 6.3$ mm; (d) H as a function of H_0 and R_{it}, $d = 6.3$ mm; (e) H as a function of d, R_{it}, and Ca. Solid lines represent fitted equations.
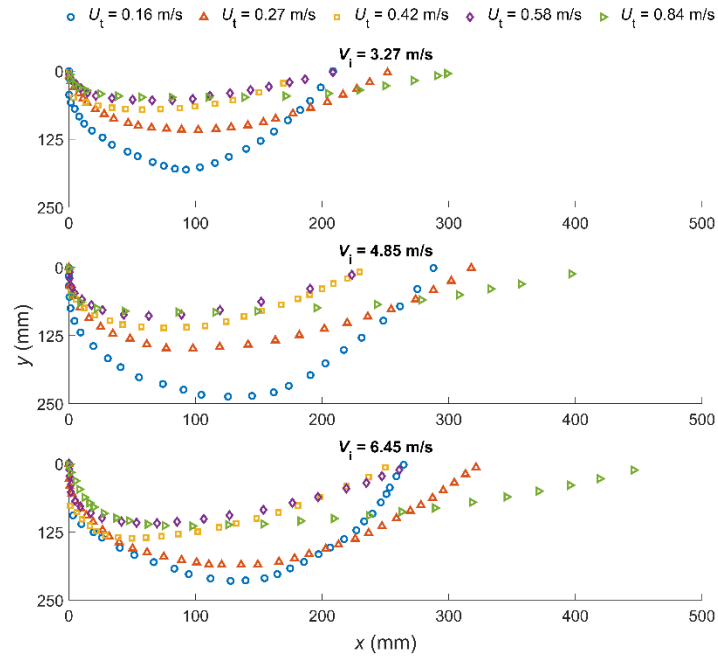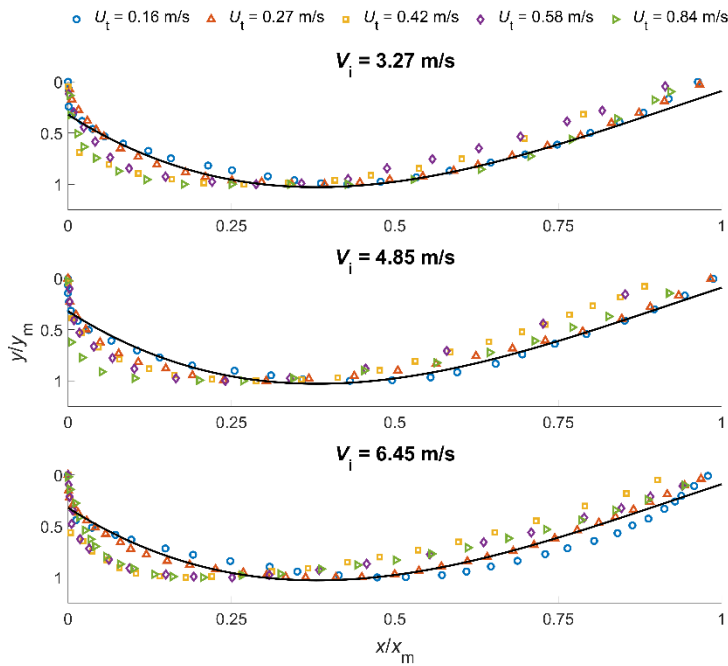
Figure 5.10: Trajectory of the bubble plume at different jet impact and translating velocities (a) Plume axis trajectory with actual dimensions (b) Dimensionless trajectory. d = 6.3 mm, and h = 20 mm. Solid line represents Equation 5.10. The jet nozzle is located at (0, 0), and the jet is translating to the left.
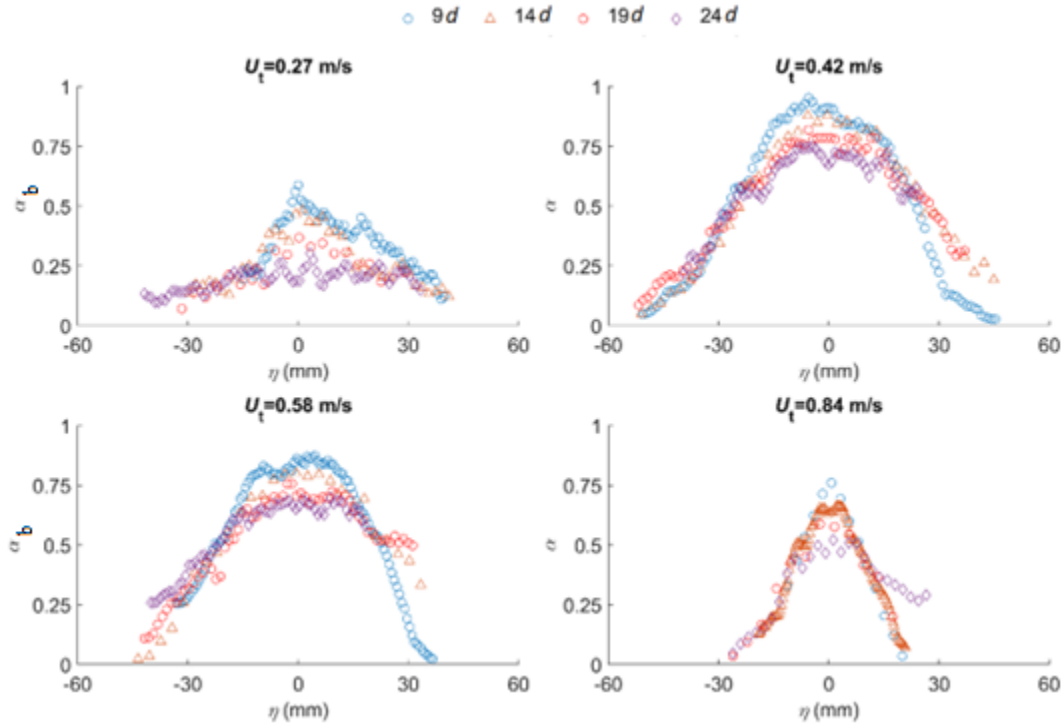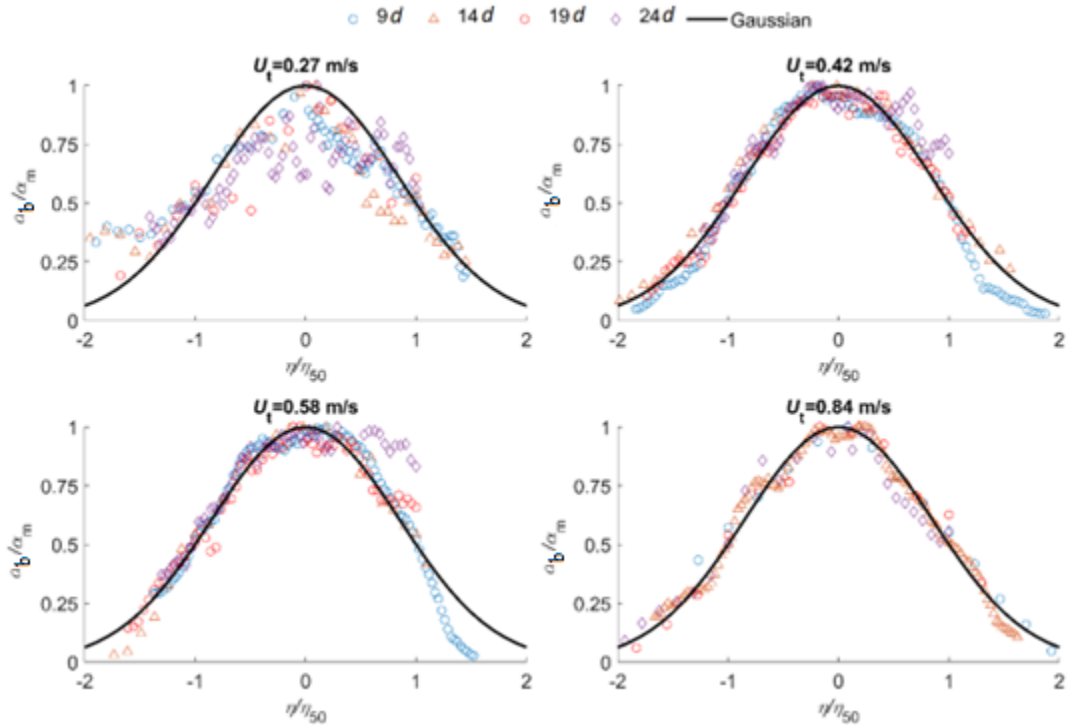
Figure 5.11: Spatial distribution of bubbles from shadowgraph images; (a) α_b at different axial distances, (b) normalized distribution. For all the profiles, $d = 6.3$ mm, $V_i = 3.27$ m/s, and $h = 20$ mm.
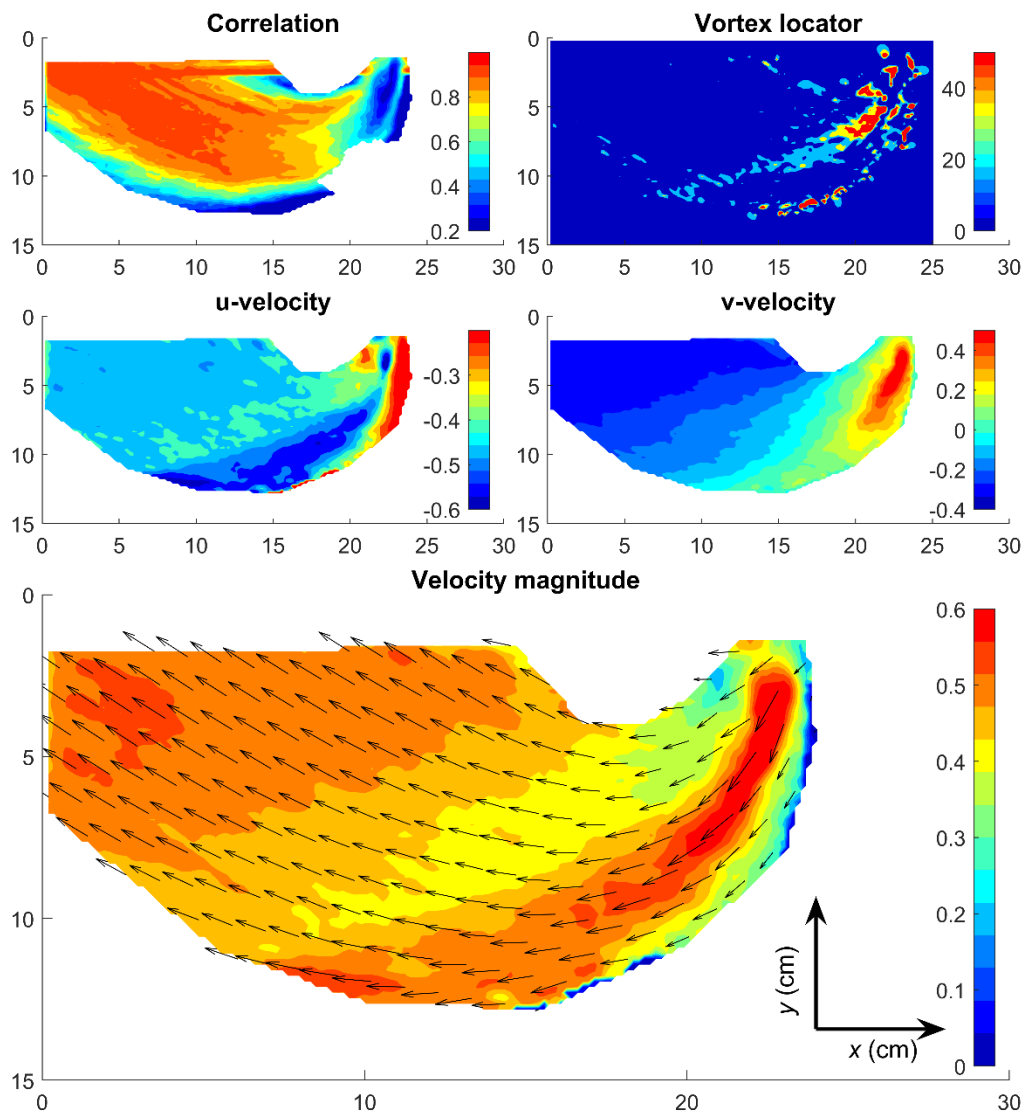
(a)

Figure 5.12: Bubble image velocimetry (BIV) results of the bubble plume using ensemble correlation technique (a) Contours of correlation, velocity components, and velocity magnitude with vectors for U_t = 0.42 m/s, (b) Velocity contours with vectors for U_t = 0.16 to 0.84 m/s. For all the cases, d = 6.3 mm, h = 20 mm, and V_i = 3.27 m/s. The reference frame is moving with the jet to the right.
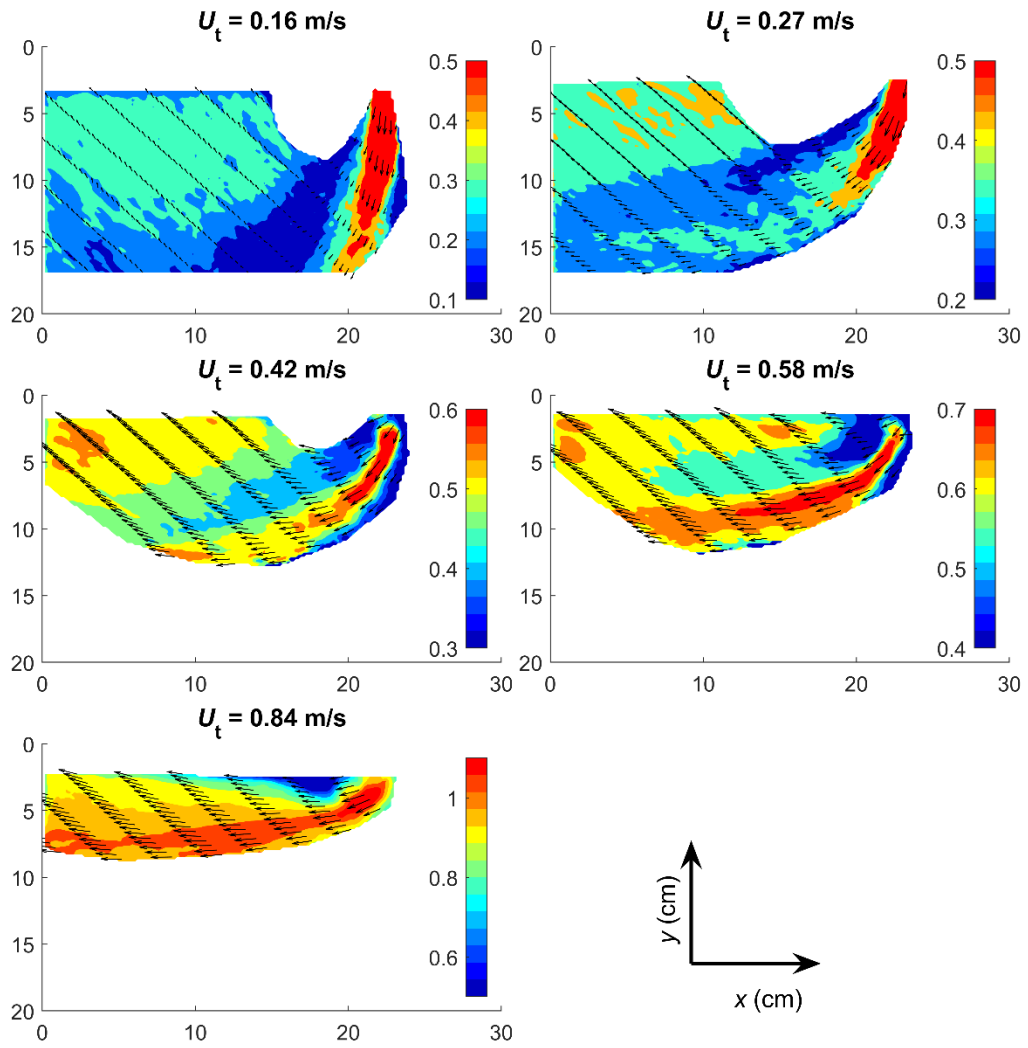
(b)

Figure 5.12: Cont'd.

CHAPTER 6. IMPINGEMENT OF A TRANSLATING CIRCULAR JET ON A FLAT WALL

6.1 Introduction

The Impingement of circular turbulent jets on solid surfaces got considerable research attention due to the extensive applications in practical engineering problems, including cooling turbine blades, drying textiles, annealing metal sheets, jet issuing from hydraulic outlets, and vertical takeoff of aircraft. Mainly, the perpendicular impingement of circular turbulent jets on a flat wall has been studied extensively because of the simplicity of the problem (e.g., Hassan et al., 2013; Fairweather and Hargrave, 2002; Giralt et al., 1977; Guerra et al., 2005; Looney and Walsh, 1984, and others). Previous studies also considered different types of jet impingement on a flat wall for turbulent axisymmetric jets. For example, the impingement of fully-developed or long jets (Beltaos and Rajaratnam, 1974), developing or short jets (Beltaos and Rajaratnam, 1977), and oblique jets (Beltaos, 1976; Jalil and Rajaratnam, 2006). Some studies have been conducted using a non-flat impingement surface, such as a convex semi-cylindrical surface (Cornaro et al., 2001), concave semi-cylindrical surface (Fenot et al., 2008), convex semi-spherical (Zhang et al., 2013), and concave semi-spherical surface (Xie et al., 2013). However, due to the complexity of the experimental setup, there is a research gap in the study of jet impingement on a solid surface involving either a translating impinging jet, or a moving impingement surface. The objective of this work is to study the impingement of a translating axisymmetric developing jet on a flat wall to understand the resulting flow field, pressure and wall shear stress.

From earlier studies, it is known that the vertical impingement of an axisymmetric jet on a flat wall results in three distinct flow regions: the free jet region, impingement region, and wall jet region. Typically, the free jet region spans from the jet issuing point to some distance before the impact on the wall. In this region, the static pressure rise at the impingement location does not affect the jet; practically, the jet behaves like a free jet. In the impingement region, the static pressure exceeds the ambient pressure, and the significant pressure gradient causes the flow to turn and run almost parallel to the wall. After the flow entirely becomes parallel to the wall, and the static pressure drops to ambient pressure, the wall jet region begins. The flow structure in the wall jet region is similar to a radial wall jet. Because the jet is circular, axial symmetry of the mean flow

characteristics remains a significant feature in all these flow regions. However, for the oblique impingement of a fully-developed jet, Beltaos (1976) showed that the axial symmetry is observed only in the free jet region. The impingement and wall jet regions show symmetry in the plane of the jet inclination. For the normal impingement of a translating jet on a flat wall, the flow regime can be modeled as a stationary jet in a crossflow, which impinges on a moving surface of the same velocity as the crossflow. Based on the observations of Beltaos (1976) on oblique jet impingement, An hypothesis can be drawn for the translating jet impingement is that the symmetry in the mean flow characteristics can be observed about the plane of the jet translation only. It is expected that the axial symmetry will not be present in any of the flow regions. Even the free jet region will not exhibit axial symmetry because this region will behave as a free jet in a crossflow.

The behavior of a circular jet injected flush into the crossflow of the same liquid depends on the relative jet translating velocity, i.e., the ratio of the crossflow velocity to the jet velocity at the nozzle (Mahesh, 2013). Due to the interaction with the crossflow, the jet's trajectory bends to the jet's leeward direction, and the jet's cross-section forms a characteristic kidney shape, resulting from the turbulent mixing with the ambient fluid at the jet's outer layer (Rajaratnam, 1976). Typically, the jet flow is divided into three regions – the potential core region, the maximum deflection region, and the vortex region. Depending on the relative jet translating velocity, the end of the potential core may remain close to the central axis of the jet nozzle. A counter-rotating vortex pair (CVP) forms in the maximum deflection region, and is responsible for the characteristic kidney shape of the jet cross-section.

Based on the above discussion on the axisymmetric jet impingement and jet in a crossflow, the flow field for a translating short jet (TSJ) impingement on a flat wall is expected to have several complex phenomena. Firstly, similar to a jet in crossflow, velocity decay for TSJ will be rapid with a short potential core. The cross-section of the TSJ will take a kidney shape depending on the translating velocity, and CVP will form at some axial distance. Secondly, although the jet is normal to the impingement wall, the impingement will be oblique due to the translating velocity. Therefore, the flow field will exhibit planar symmetry with respect to the plane of the jet translation. Furthermore, the location of the point of impingement, maximum shear stress, stagnation pressure, and other characteristic flow features will depend on the relative jet translating velocity. Lastly, similar to a cylinder in crossflow, the translating jet at the impingement location

behaves as an obstacle column to the crossflow. Therefore, vortex shedding in the wake of the deflected jet and horseshoe vortex formation on the windward side of the jet is likely to be observed for the translating jet. Moreover, at bigger relative translating velocities, the wall jet region of the impinging jet on the windward side may completely diminish, and even on the leeward side, the wall jet region may get affected due to the formation of the CVP. These interesting flow features and many engineering applications motivate this work to study the impingement of a short translating jet on a flat wall.

6.2 Experimental Setup

The PIV experiments were conducted in the T. Blench Hydraulics Laboratory of the University of Alberta. Figure 6.1 shows the schematics of the experimental setup. A towing tank of dimensions 10 m long by 0.8 m wide by 0.8 m depth was used for the experiments. The walls and the tank floor are made of plexiglass for flow visualization. A computer-controlled carriage system, operated using LabVIEW software, is mounted on the top of the tank to carry instruments. A 1 m long and 25 mm diameter PVC pipe with a 19 mm nozzle was used to produce the impinging jet. The pipe was mounted vertically to the carriage to translate horizontally. Water was supplied to the pipe using a centrifugal pump through a flexible hose. The pump recirculates water between the towing tank and the pipe. Several Valves and a magnetic flowmeter were used for flow control and measurement, respectively.

The PIV instrumentation comprised a high-speed camera (Phantom v211, Vision Research, Wayne, New Jersey) and a continuous 6W Argon-ion laser with a wavelength of 488 nm (Stabilite 2017, Spectra Physics). A Nikon lens (Nikon AF Micro NIKKOR 60 mm f/2.8D) was used with the camera to focus on the location of interest. The camera was mounted to the side of the carriage so it could translate with the jet and capture images from the side of the towing tank. The laser was equipped with an optics (OZ optics) to generate a laser sheet from the laser beam. The optics was placed under the towing tank so that the laser sheet remained perpendicular to the towing tank floor. Further, the laser sheet was aligned with the jet translating plane.

For PIV analysis, images were captured at a frequency of 1000 frames per second and preprocessed in MATLAB and ImageJ (Schneider et al., 2012) software. The PIV analysis was conducted using

PIVlab software (Thielicke and Sonntag, 2021). A 32 by 32 pixel interrogation window was selected for the analysis, where 1 pixel $= 6 \times 10^{-5}$ m.

Table 6.1 shows the experimental conditions for the PIV experiments. Experiments were conducted for four translating velocities, U_t = 0.03, 0.05, 0.07, and 0.09 m/s, while the jet properties (i.e., d, V_j, and h) were kept the same. Note that the continuous 6W laser was not strong enough to conduct PIV experiments with V_j and U_t bigger than the selected range. Nonetheless, the jet was turbulent since the Reynolds number was bigger than 3000 (Rajaratnam and Flint-Petersen, 1989). Velocity ratio R for the experiments varied between 0.17 to 0.51 m/s.

6.3 Numerical Model

6.3.1 Model Geometry and Boundary Conditions

Figure 6.2 shows the schematic diagram of the model domain. To reduce computational effort, a plane of symmetry was considered along the plane of the jet translation, and a smaller model was used compared to the towing tank. The model was 0.8 m long, 0.2 m wide, and 0.1 m deep. The jet was modeled with a 50 mm long and 19 mm diameter smooth pipe. Since the jet bends as it translates, the model had a longer dimension (0.5 m) in the opposite direction of jet translation.

Typically, the mesh has to be finer at the impingement region, then gradually coarser in the radial direction going far from the point of impingement. Simulating a translating jet is not practical considering a finite domain and optimized meshing criteria. Therefore, a stationary jet with no-slip translating floor and a uniform cross-stream velocity equal to the jet translating velocity was considered to simulate the problem. In this way, the relative translation of the jet simulates the laboratory flow condition. Fig. 7.2a Shows the model geometry and boundary conditions. The description of the boundary conditions is as follows:

(a)   Inlet boundary: Two velocity inlets were used. One is the jet inlet with a uniform velocity of 0.176 m/s. Another one with a uniform cross-stream flow of velocity equal to the jet translating velocity through the vertical wall at the windward side of the jet.

(b)   Outlet boundary: A pressure outlet boundary condition was used at the vertical wall on the leeward side of the jet.

(c)   Symmetry boundary: Considering the symmetry of the velocity field of the jet, and cross-stream velocity, a half-jet model was used with a vertical symmetry wall along the jet axis and parallel to the cross-stream flow.

(d)   Wall boundary: To account for the drag and development of boundary layers, the floor was modelled as a moving no-slip wall. Since the top surface and the vertical wall opposite the symmetry wall were located far from the impingement region, the flow was assumed to become parallel to these walls. Therefore, these walls were modelled as slip boundaries to ensure no flow through these walls and no boundary layers development. This simplification also reduced computational effort in the simulations and resulted in better convergence.

6.3.2 Mesh Generation and Grid Independence

A structured grid with hexahedral mesh elements was developed in the open-source software SALOME (see Figure 6.2b-7.2e). Although creating a structured mesh for complex geometries is difficult and time-consuming, it is less susceptible to artificial diffusion and more efficient to converge than an unstructured mesh. To generate the structured mesh, the geometry of the towing tank with the jet nozzle inside was modeled in SALOME GEOM module. After that, the geometry was segmented into smaller volumes using the partition tool, so each contained eight vertices – a criterion to generate hexahedral mesh elements inside any volume. Because of the bigger velocity and pressure gradient in the impingement region, the mesh size should be smaller near the jet nozzle and the impingement region on the floor and gradually bigger as the distance from the nozzle and floor increases. This was ensured by systematic segmentation of the original geometry into smaller volumes. Finally, SALOME MESH module was used to generate hexahedrons inside these segments.

The automatic meshing algorithm for hexahedrons was used to generate the mesh. This algorithm divides the dimensions of the geometric volumes into a user-provided number of segments. At first, a coarse mesh with 15 segments (15 cells or 16 nodes) inside each geometric volumes was generated. Then the number of segments was gradually increased until a mesh-independent solution was obtained. It should be noted that the numerical solution asymptotically approaches the exact solution with the increment of the number of cells. However, it is computationally very resource-intensive to simulate with a large number of cells, and the relative improvement of the

solution in the asymptotic convergence zone is relatively insignificant.

The v-velocity component near the floor is critical due to the high gradient of v in this region and was tested for grid independence. Figure 6.3a shows that the profiles for v-component do not vary much for the increment of volume segmentation from 35 to 40. Further, Figure 6.3b shows that the variation of point velocity is in the order of 10^{-4} for incrementing the number of cells from 7 to 11 million. Therefore, considering the solution accuracy and computational resource utilization, the selected mesh for this study has 40 segments in each small geometric volume and about 11 million cells.

6.3.3 Flow Condition and Solver Setup

A steady-state simulation was conducted in OpenFOAM using the SimpleFoam solver since the fluid was incompressible. A second-order scheme, the Bounded Gauss Upwind algorithm, was used for discretization. The Reynolds Averaged Navier-Stokes (RANS) equations were solved for turbulence modelling. For this purpose, the k-w model with Shear Stress Transport (SST) was selected because it is ideal for wall-bound flows. The turbulence intensity at the jet nozzle was set as 0.01. The residual values for all parameters in consecutive iterations were set as 10^{-6} or less as the criterion for simulation convergence.

6.4 Results and Discussion

6.4.1 Mean Flow Characteristics from PIV and CFD

Figure 6.4 shows the effect of the translating velocity of the jet on the flow characteristics for PIV experimental results and OpenFOAM simulations. Entrainment of the surrounding fluid into the jet flow is identified as high-vorticity regions. The translating jet's windward and leeward sides show opposite signs for vorticity. As R increases from 0.17 to 0.51, the translating jet bends more to the leeward direction of travel, similar to a jet in crossflow (Margason, 1993). At $R = 0.17$, a vortex of size comparable to the jet diameter d is formed at the windward side of the jet. As the relative translating velocity increases to $R = 0.28$, the vortex size decreases to about $1/3d$. Finally, the vortex completely diminishes at bigger relative translating velocity ($R = 0.40$ and 0.51).

The velocity contours with streamlines in Figure 6.4(b) reveals further details of the flow

characteristics. At smaller relative translating velocities (i.e., $R = 0.17$ and 0.28), the impingement is strong, with a visible stagnation point at the intersection of the jet axis and the floor. Although the jet is a short jet with $h = 2.6d$, the jet velocity is expected to decay faster than a free jet due to the impingement. Significant velocity gradients are observed near the impingement and jet boundary. At the windward side, the streamlines are typically parallel to the floor except for certain proximity to the jet, especially at bigger R. On the windward side, the streamlines bend to the direction of the jet due to the surrounding fluid entrainment. In all cases, the deflected jet to the leeward side after impingement is comparable to a wall jet, similar to a vertical jet impingement on a flat wall (Beltaos and Rajaratnam, 1974). However, transverse sections of the deflected jet has to be studied to confirm the similarity with a wall jet. Further, the streamlines in the windward side do not show any resemblance to a wall jet for big relative translating velocities.

For all the translating jet cases, the vorticity and velocity contours with streamlines show good similarity between the PIV experimental results and CFD simulations in OpenFOAM. Therefore, it is appropriate to use the developed CFD models for detailed analysis of the flow field.

6.4.2 Mean Velocity Distribution

Figure 6.5 shows the velocity fields of the impinging jet. Since the impingement height H is only $2.6D$, the jet is in the developing jet regime (Nallamuthu Rajaratnam, 1976). Velocity vectors in Figures 7.5a and 5b show a core with a uniform velocity of $U = V_j$ for some distance from the nozzle, termed the potential core. The potential core is surrounded by an annular shear layer. For a relatively slower translating jet with $U_t = 0.03$ m/s and $R = 0.17$, the velocity distribution is quite similar to a stationary circular jet as depicted in the literature (e.g., Rajaratnam and Beltaos, 1977). With the increase of U_t, the velocity vectors align with a curvilinear trajectory as the jet sways to the leeward direction of travel. Considering the transverse plane of the jet translation (i.e., y-z plane), the velocity vectors show faster jet velocity decay as the translating velocity increases. However, the velocity distribution is symmetric about the nozzle centerline since there is no resultant crossflow in the transverse direction.

The jet flows along the wall after impingement in the impingement region (Figure 6.5c and 5d). Figure 6.5c shows that for a small translating velocity with $R = 0.17$, the deflected jet flows in both the windward and leeward directions. However, after a short distance of $x/d = 2$, the deflected jet

in the windward direction folds back and creates a vortex. For bigger translating velocities with $R \geq 0.28$, the deflected jet only flows to the leeward direction. For $R = 0.17$, the velocity profiles in the leeward direction resemble a wall jet, characterized by decaying and spreading velocity vectors as the deflected jet travels far from the impinging jet. Eventually, the velocity vectors match the jet's translating velocity at about $x/d = -6.1$. Interestingly, for $R \geq 0.28$, the velocity vectors decay with distance from the impinging jet, due to bigger U_t. However, in Figure 6.5d, the similarity of the flow to a wall jet is observed in the transverse direction (y-z plane) for all translating velocities. After a distance of $x/d = 4.2$, flow velocity in this direction decays to almost zero, indicating that the model domain size in the y-direction ($x/d = 10.5$) is sufficient to simulate the flow field accurately.

Profiles of the mean velocity component v in Figure 6.6a show that v decays rapidly as R increases. Unlike the velocity profiles of a stationary jet, the near-nozzle profiles of the v component around the jet axis are not horizontal but slanted due to the jet's translation. The peaks of the profiles also shift to the leeward direction of translation. In Figure 6.6b, profiles of the u component for $R = 0.17$ and 0.28 show similarity with a wall jet. However, as the translating velocity increases, profiles in the windward direction deviate from the wall jet profiles first. Then the profiles in the leeward direction slowly differ from a wall jet. Instead, the profiles show uniform freestream velocity distribution as observed for $R = 0.51$.

Figure 6.7 shows the potential core length L_p at different translating velocities for $R = 0.17$ to 0.51. As hypothesized, the potential core length decreases with the increase of translating velocity. A linear expression reasonably fits the simulation results for the potential core length.

$$\frac{L_p}{d} = -2.81R + 1.49; \qquad \text{for } h/d = 2.6 \text{ and } \mathrm{Re} = 3344 \tag{6.1}$$

For a stationary impinging jet with $h = 2.6d$, extrapolating Equation 6.1 gives $L_p = 1.5d$. For $h = 2.2d$ to $5.2d$, Beltaos and Rajaratnam (1977) showed that the potential core length does not depend on h but diminishes at about a distance of $1.1d$ from the impingement wall. This also gives $L_p = 2.6d - 1.1d = 1.5d$. This implies that the simple linear relation in Equation 6.1 predicts the potential core length for a translating short jet with good accuracy. It should be noted that apart from the hydraulics of the flow regime, the potential core length also depends on the nozzle

characteristics (Ashforth-Frost and Jambunathan, 1996).

6.4.3 Vortex Structure

Development of the velocity contours of the jet cross sections at increasing x/d gives an overview of the vortex structure of the impinging translating jet in Figure 6.8. For $R = 0.17$ and $x/d = 0$, the velocity contours resemble a stationary circular jet impingement, characterized by a high-velocity axial jet core and a stagnation region at the point of impingement. However, instead of forming radial wall jets along the y-direction, the deflected jet folds back due to the interaction with the relative crossflow in the x-direction. The crossflow eventually diminishes the deflected jet flow in the y-direction after a distance of $y = 8$ cm, as illustrated in Figure 6.5d. At $x/d = 0.5$, the central high-velocity core is observed to separate and start forming two vortices. For $x/d \geq 2$, a fully-developed counter-rotating vortex pair (CVP) with a high-velocity core at the center of the vortices are observed.

For $R = 0.28$ the inner central velocity core shows separation into two vortices at $x/d = 0.5$. However, unlike the case for $R = 0.17$, the axial high-velocity core remains along with the CVPs. This phenomenon is also observed for $R = 0.40$ and $x/d \geq 1$. However, for $R = 0.40$ and $x/d \leq 0.5$, the cross-sections of the jet show an axial high-velocity kidney shape core, similar to a jet in crossflow (Rajaratnam and Gangadharaiah, 1983). This is because the jet's impingement does not influence these sections much. The axial high-velocity core is observed with a weak CVP for $R = 0.51$ and $0 \leq x/d \leq 3.8$. In this case, due to the bigger translating velocity of $U_t = 0.09$ m/s, the jet moves farther leeward, and the impingement becomes weaker compared to other cases ($R = 0.19$ to 0.40).

6.4.4 Pressure Distribution

A dimensionless parameter, the pressure coefficient C_p, is used to assess the effect of the relative pressure in the flow characteristics. Equation 6.2 gives the value of C_p,

$$C_p = \frac{P_s - P_a}{1/2 \left(\rho_w V_j{}^2 \right)} \tag{6.2}$$

where P_s is the static pressure on the impingement wall, P_a is the ambient pressure of the environment, and ρ_w is the density of the jet fluid used.

The distribution of C_p on the impingement wall along the course of the jet for $U_t = 0.03$ to 0.09 m/s is shown in Figure 6.9. The reported pressure has both positive and negative values since it was calculated relative to the outlet boundary. The peak value of C_p indicates the impingement location, typically at the stagnation point. The peak gets bigger as R gets smaller. This is because a strong impingement occurs at a lower translating velocity. As the translating velocity increases, the peak value of C_p shifts towards the leeward direction. For $R = 0.17$, and 0.28, three distinct pressure regions are observed. Region A is the deflected jet region, where the jet changes its course after the impingement and eventually flows parallel to the impingement wall. Region B is the impingement region with peak relative pressure. Lastly, region C is the recirculation region, where the deflected jet folds and recirculates due to the adverse movement of the relative crossflow. For $R = 0.17$ and 0.28, C_p is close to unity due to strong impingement, and the impingement region is well demarcated. Due to the jet translation, the relative crossflow current is quite strong, and distinguishable recirculation regions exist in the windward direction. One of the major characteristics of the impingement region for $R = 0.17$ and 0.28 is the flow separation at the stagnation point. However, for $R = 0.40$ and 0.51, C_p is well below unity as the impingement is weak, and flow separation is not evident (see Figure 6.4). Therefore, the recirculation region does not exist for bigger jet translating velocities. Table 6.2 shows the salient features of these flow regions for the translating jet impingement.

6.4.5 Wall Pressure

Figure 6.10 shows the distribution of wall pressure for $U_t = 0.03$ to 0.09 m/s. At lower translating velocities, the pressure concentrates on a smaller area around the stagnation point. The pressure distribution pattern for $R = 0.17$ to 0.28 changes from a half-circle to a kidney shape. This pattern is consistent with the shape of the jet core in crossflow. With the increasing translating velocity, the maximum wall pressure decreases, but the area of influence of the pressure increases to an elongated area. For vertical impingement of long and short jets, Beltaos and Rajaratnam (1974, 1977) showed that the dimensionless profiles of the wall pressure are similar. However, the impingement of a translating jet may resemble to an oblique stationary jet due to the bending of the jet at the relative crossflow. For oblique jet impingement, Beltaos (1976) showed that the wall pressure distribution is still similar in the transverse direction of the jet inclination plane. The following Gaussian relation was proposed to describe this similarity,

$$\frac{P_s}{P_{sm}} = e^{-0.693\left(\frac{y}{a}\right)^2} \tag{6.3}$$

where P_{sm} is the maximum static pressure, and a is the value of y where $P_s = 0.5P_{sm}$. Dimensionless wall pressure profiles are plotted with Equation 6.3 in Figure 6.11 to investigate the similarity of wall pressure distribution for a translating jet. Figure 6.11a shows that the profiles are not similar for a fixed translating velocity at different longitudinal locations ($x/d = $ -20 to 2). Further, Figure 6.11b shows that for the exact longitudinal location, the profiles for different translating velocities ($R = 0.17$ and 0.51) are also not similar. However, for practical purposes, the pressure distribution in the transverse direction can be roughly similar for the range $0 \leq y/b \leq 1$.

6.4.6 Wall Shear Stress

For the vertical impingement of a stationary jet of long and short impinging height, the wall shear stress contour is typically circular, with zero shear at the center of the contour plot just beneath the nozzle and an annular ring of maximum shear stress at some radial distance from the maximum shear location (Beltaos and Rajaratnam, 1974, 1977). However, for a translating jet, the distribution of wall shear stress will be different due to the translation of the jet. The effect of the jet translating velocities on the wall shear stress is shown in Figure 6.12. At small translating velocities (i.e., $R = 0.17$ and 0.28), the annular ring of the maximum shear stress elongates and forms a crescent shape. With further increments of translating velocities to $R = 0.40$ and 0.51, this shape evolves into a fly-wing shape, characterized by a low shear region on the axis of symmetry.

Fig 13a shows the distributions of the wall shear stress τ_0 in the transverse direction of the jet translation for $R = 0.17$ to 0.51. Locations of the maximum wall shear stress τ_{0m} are different. If y_0 is the y position of τ_{0m}, and b is the y position of the $0.5\tau_{0m}$, then the shear stress distribution for $y \geq y_0$ can be shown by the following relation,

$$\frac{\tau_0}{\tau_{0m}} = \frac{1}{2}\left[1 + \sin\frac{\pi}{2}\left(1 + \frac{y - y_0}{b}\right)\right] \tag{6.4}$$

Figure 6.13b shows that the performance of Equation 6.4 gets better in predicting the shear stress distribution as the translating velocity increases. It also implies a similarity in the distributions of the wall shear stress for $y \geq y_0$.

6.5 Summary and Conclusions

This work shows a combined experimental and numerical study of the impingement of a translating submerged circular turbulent jet on a flat wall using particle image velocimetry (PIV) and computational fluid dynamics (CFD) techniques, respectively. The CFD model, developed in OpenFOAM has been validated against the PIV results. Since the experimental setup for PIV to obtain data from multiple planes was difficult for the translating jet experiment, CFD simulation has provided valuable insight into this three-dimensional problem's flow field. Some of the critical findings include:

1. The structure of the flow field changes with the translating velocity. Streamlines of the flow field demonstrated that at lower jet translating velocity, a vortex forms at the windward side of the translating jet, which reduces in size with increasing translating velocity and ultimately diminishes at bigger translating velocity.

2. Analysis of the mean velocity field showed a reduction of the potential core with translating velocity, and an expression for the length of the potential core has been developed.

3. Depending on the magnitude of the jet translating velocity, a high-velocity jet core and a counter-rotating vortex pair (CVP) can be seen in the cross-sections of the jet. The CVP disrupts the formation of the wall jet at the leeward side after the impingement region.

4. Based on the relative pressure distribution, three flow regions has been identified: the impingement region, the deflected jet region, and the recirculation region. However, at bigger translating velocities, the recirculation region collapses into the impingement region.

5. The magnitude of the maximum wall pressure and shear stress reduces with translating velocity. As the translating velocity increases, the wall shear stress distribution evolves from a crescent shape to a fly-wing shape, with a low shear region at the axis of symmetry.

6. Wall shear stress distribution at the transverse direction of the jet translation is similar, and an expression for the distribution has been developed.

Table 6.1: Experimental parameters of the PIV experiments

Parameters	Value
Nozzle diameter, d (mm)	19
Impingement height, h (mm)	50
Jet velocity at nozzle, V_j (m/s)	0.176
Jet translating velocity, U_t (m/s)	0.03, 0.05, 0.07, and 0.09
Jet Reynolds number, Re = $V_j d/\nu$ (-)	3344
Relative translating velocity, $R = U_t/V_j$ (-)	0.17, 0.28, 0.40, and 0.51

Table 6.2: Features of flow regions for an impinging jet with different translating velocities.

Features	$R = 0.17$	$R = 0.28$	$R = 0.40$	$R = 0.51$
Point of impingement $(= x/d)$	-0.04	-0.46	-1.14	-0.17
Peak pressure coefficient, C_{pm}	1	0.67	0.22	0.08
Boundary of deflected jet and impingement regions $(= x/d)$	-1.26	-1.43	-2.20	-2.4
Boundary of impingement and recirculation regions $(= x/d)$	1	0.12	-	-

Note: Negative x/d indicates leeward side of jet translation.
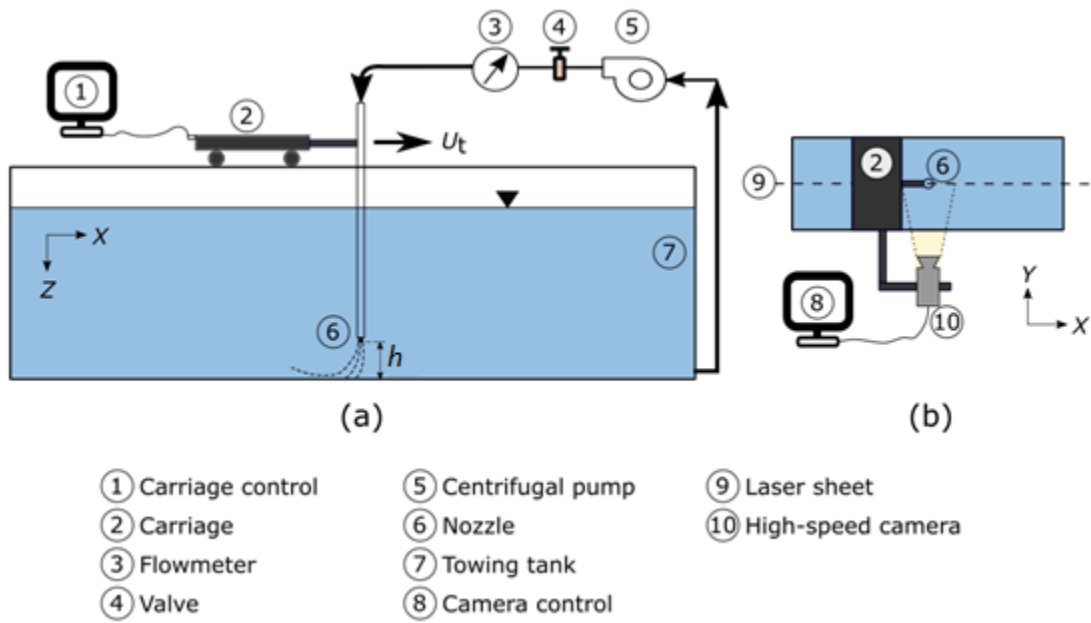
Figure 6.1: Schematics of the experimental setup: (a) flow control system and translating jet in the towing tank, and (b) image acquisition setup for PIV (top view).

① Carriage control	⑤ Centrifugal pump	⑨ Laser sheet
② Carriage	⑥ Nozzle	⑩ High-speed camera
③ Flowmeter	⑦ Towing tank	
④ Valve	⑧ Camera control	
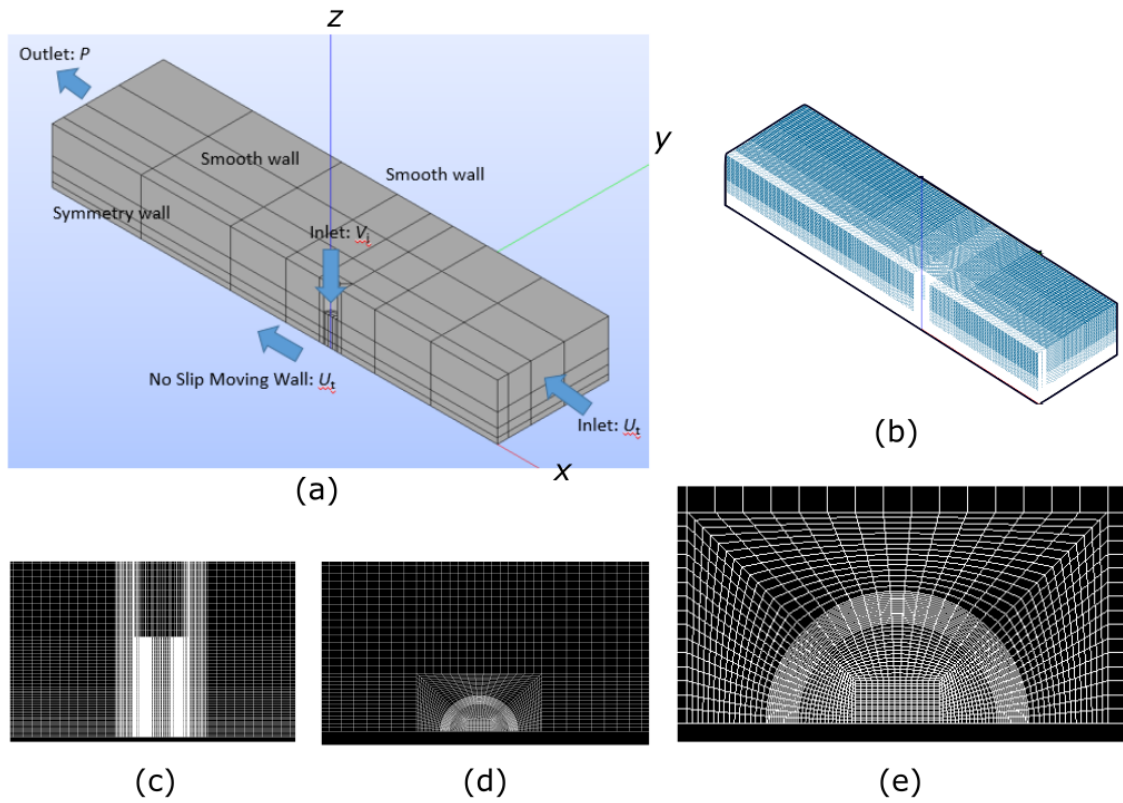
Figure 6.2: Model generation: (a) geometry and boundary conditions, (b) hexahedral mesh in generation in model, (c) zoomed view of the jet region in *z-x* plane, (c) zoomed view of the jet region in *x-y* plane, and (d) detail of the structured mesh at the jet nozzle.
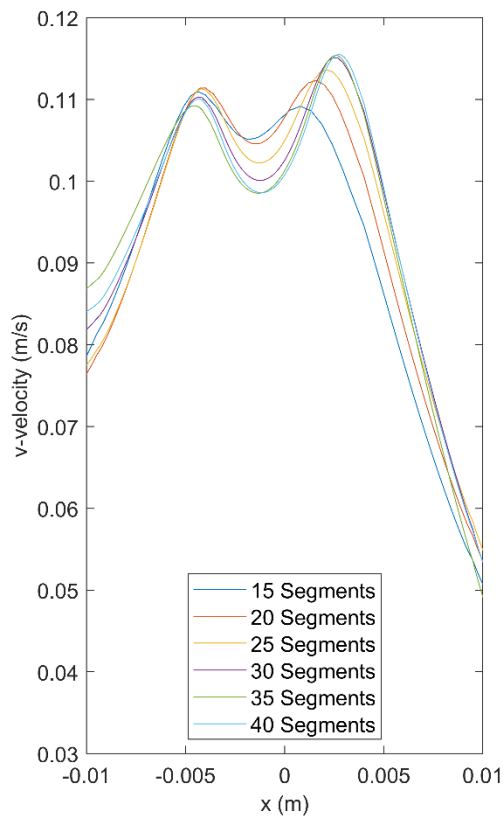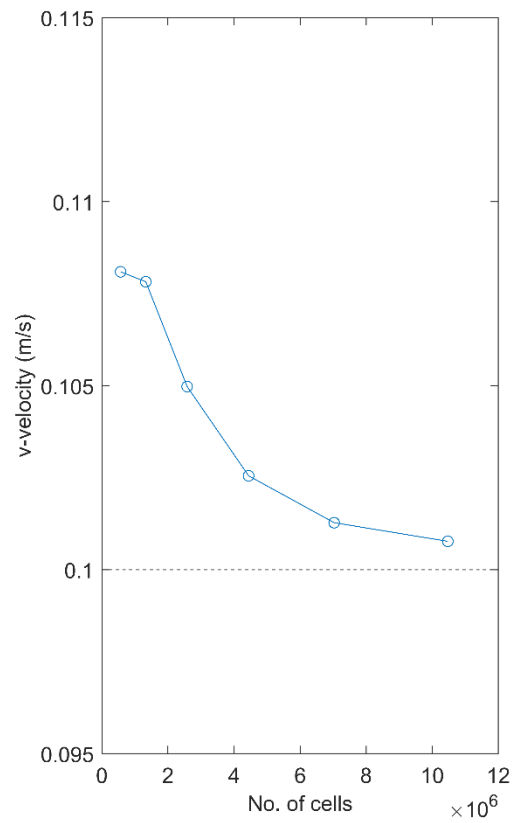
(a)   (b)

Figure 6.3: Grid independence testing for *v*-velocity component (a) profile at $z = 5$ mm, and (b) point velocity at $x = 0$ mm, and $z = 5$ mm.
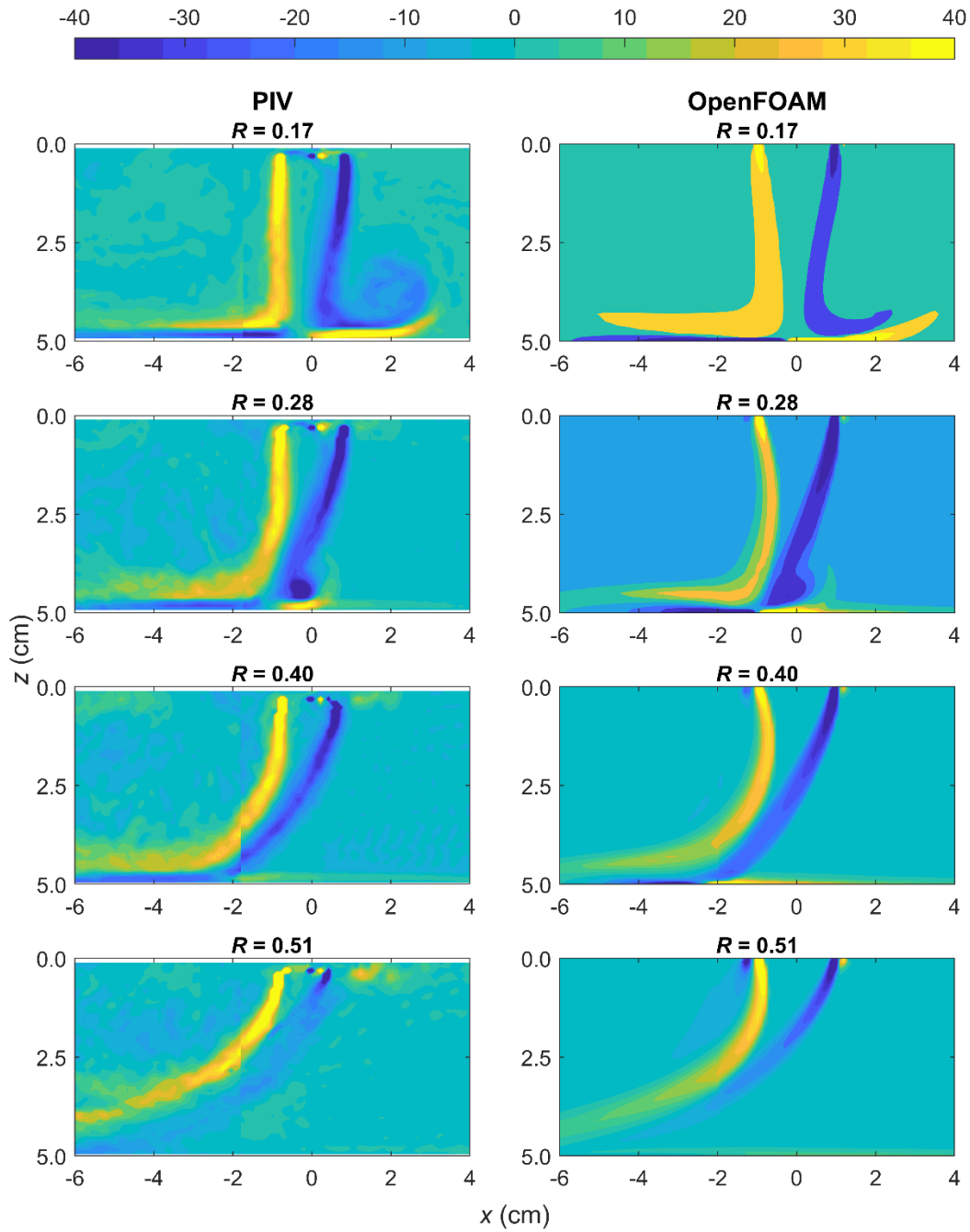
(a)

Figure 6.4: Comparison of PIV and OpenFOAM results for $U_t = 0.03$ to 0.09 m/s (a) vorticity contours (s^{-1}), and (b) velocity contours (ms^{-1}) and streamlines. The jet translates to the right.
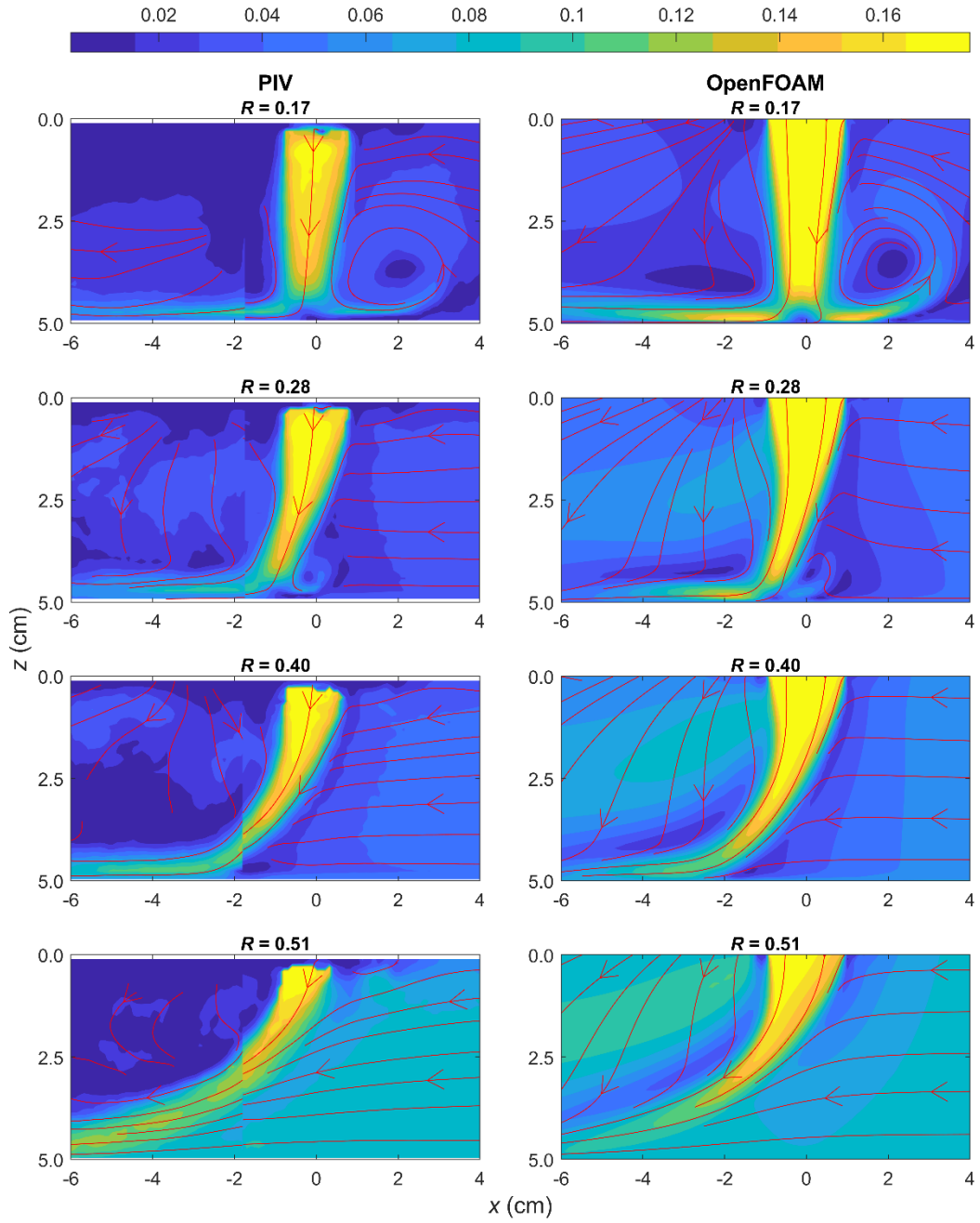
(b)

Figure 6.4: Cont'd.
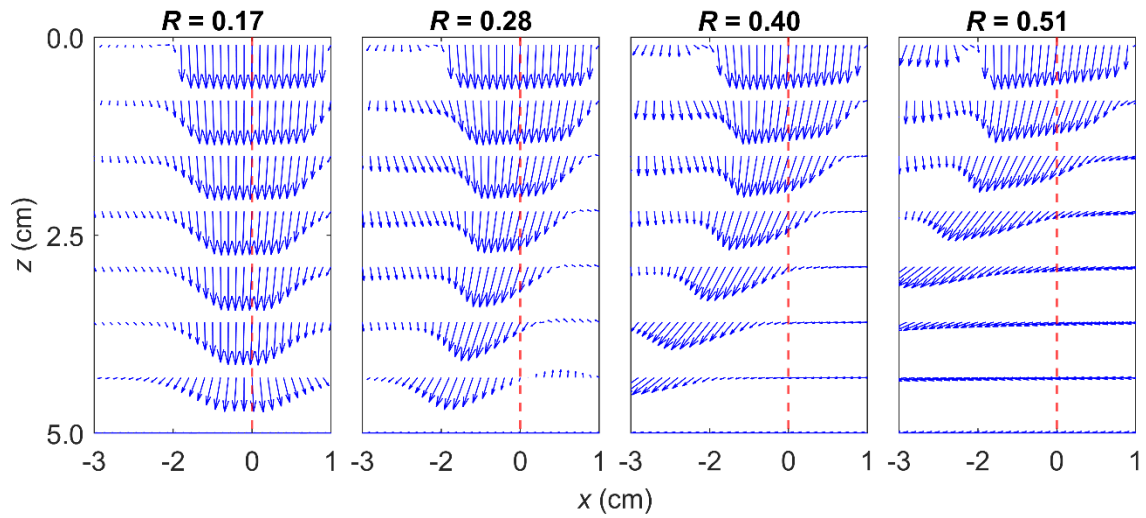
(a)
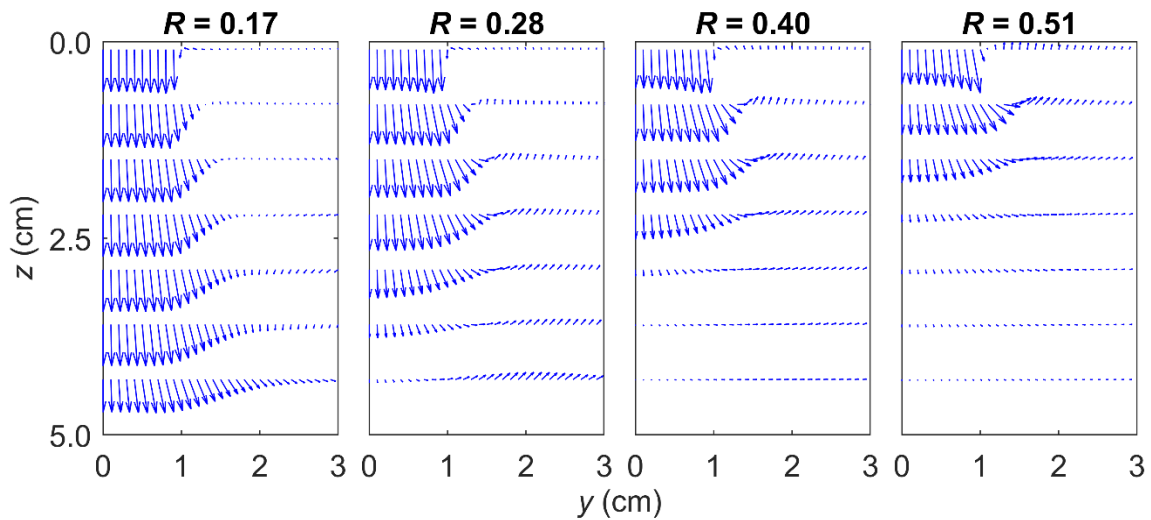
(b)

Figure 6.5: Velocity fields for the impinging jet at translating velocities $U_t = 0.03$ to 0.09 m/s for (a) developing jet in xz – plane; (b) developing jet in yz – plane, (c) impingement region in xz – plane; and (d) impingement region in yz – plane. At (a) and (c), the jet is translating to the right, and at (b) and (d), the jet is moving into the plane. In the plots, $(x, y, z) = (0, 0, 0)$ cm and $z = 5$ cm indicate the nozzle location and the impingement wall, respectively. Red broken lines in (a) and (c) indicate the nozzle axis.

(c)

(d)

Figure 6.5: Cont'd

118
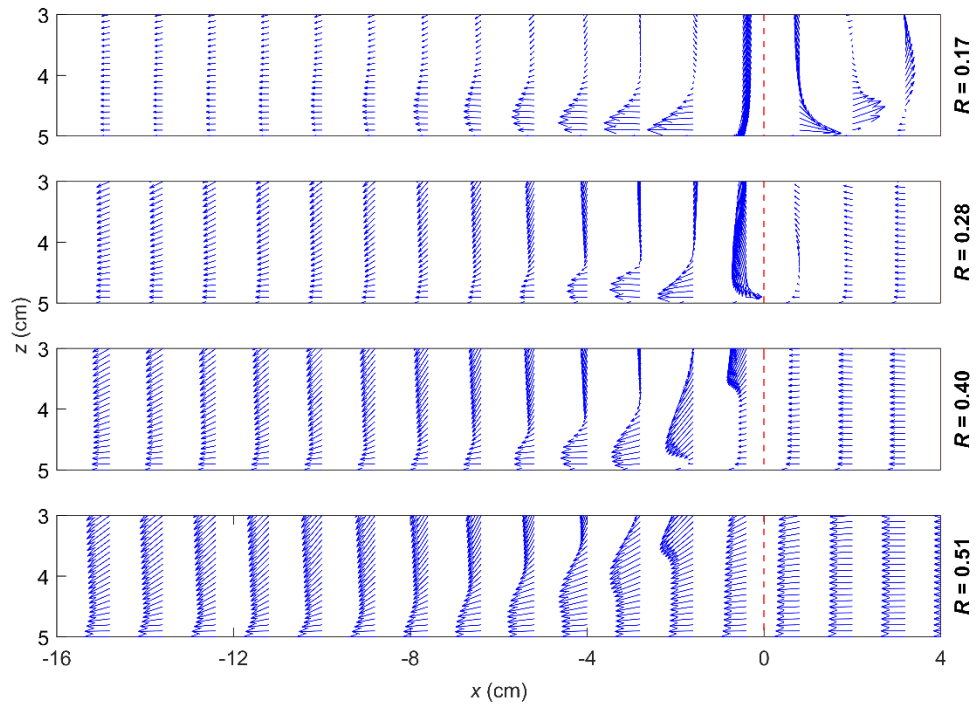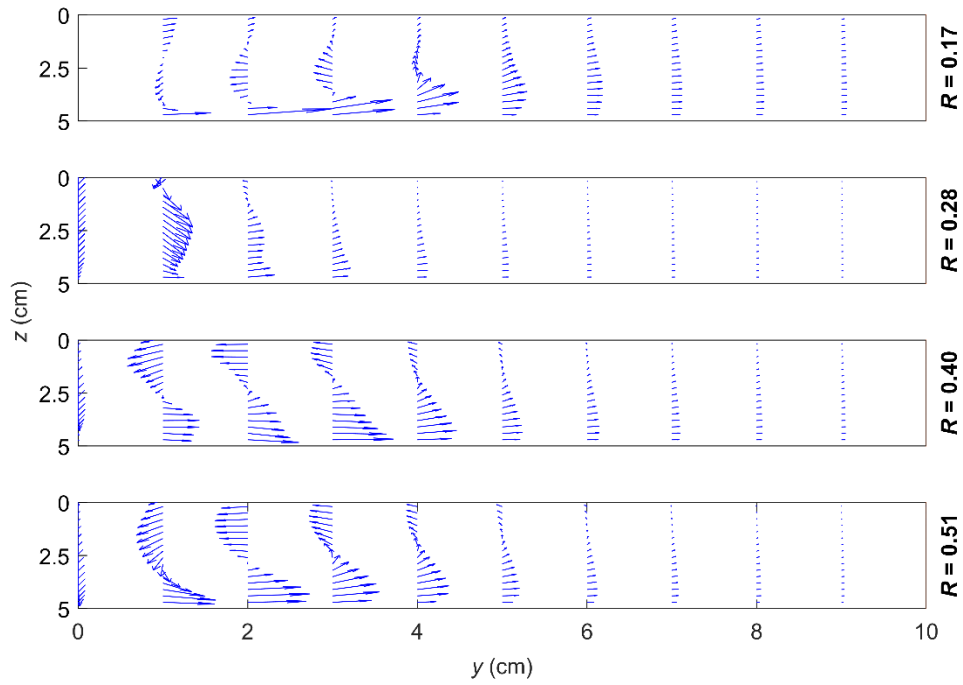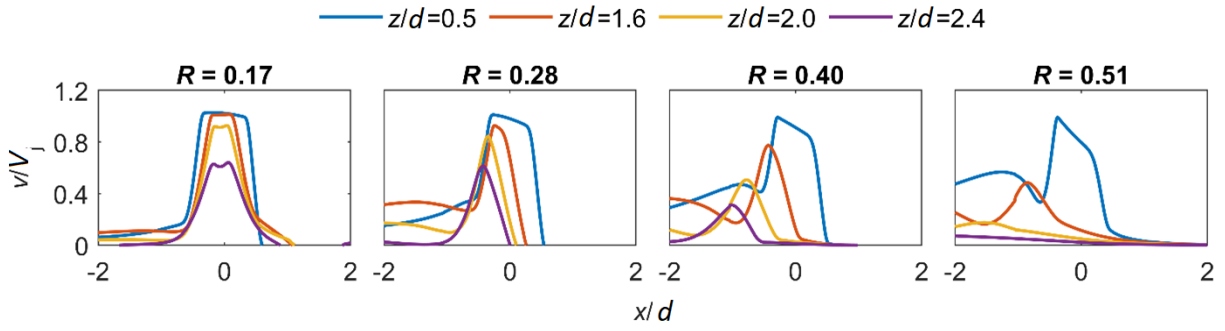
(a)
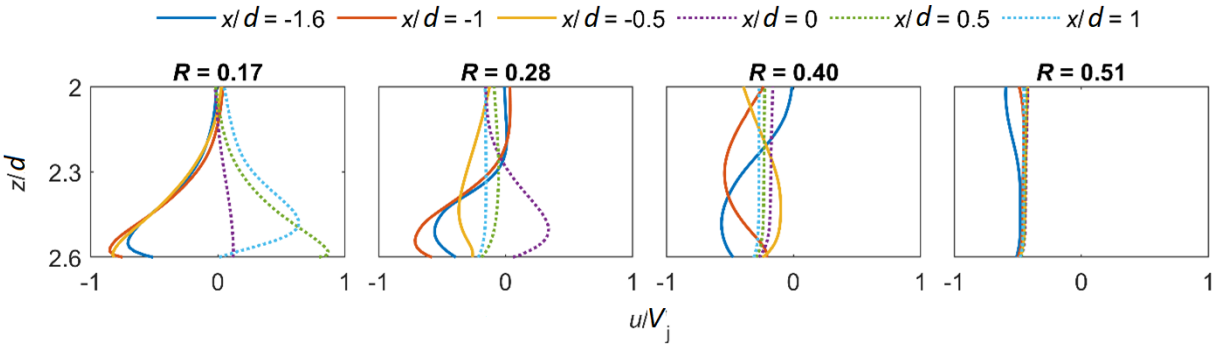
(b)

Figure 6.6: Profiles of the mean velocity components: (a) distributions of the mean vertical velocity component v; and (b) distribution of the mean horizontal velocity component u. For (b), broken and solid lines represent velocity profiles for the windward and leeward direction, respectively.
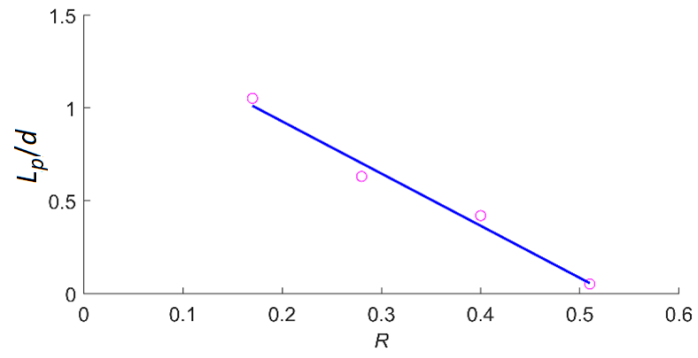
Figure 6.7: Evolution of the potential core length with the relative translating velocity.
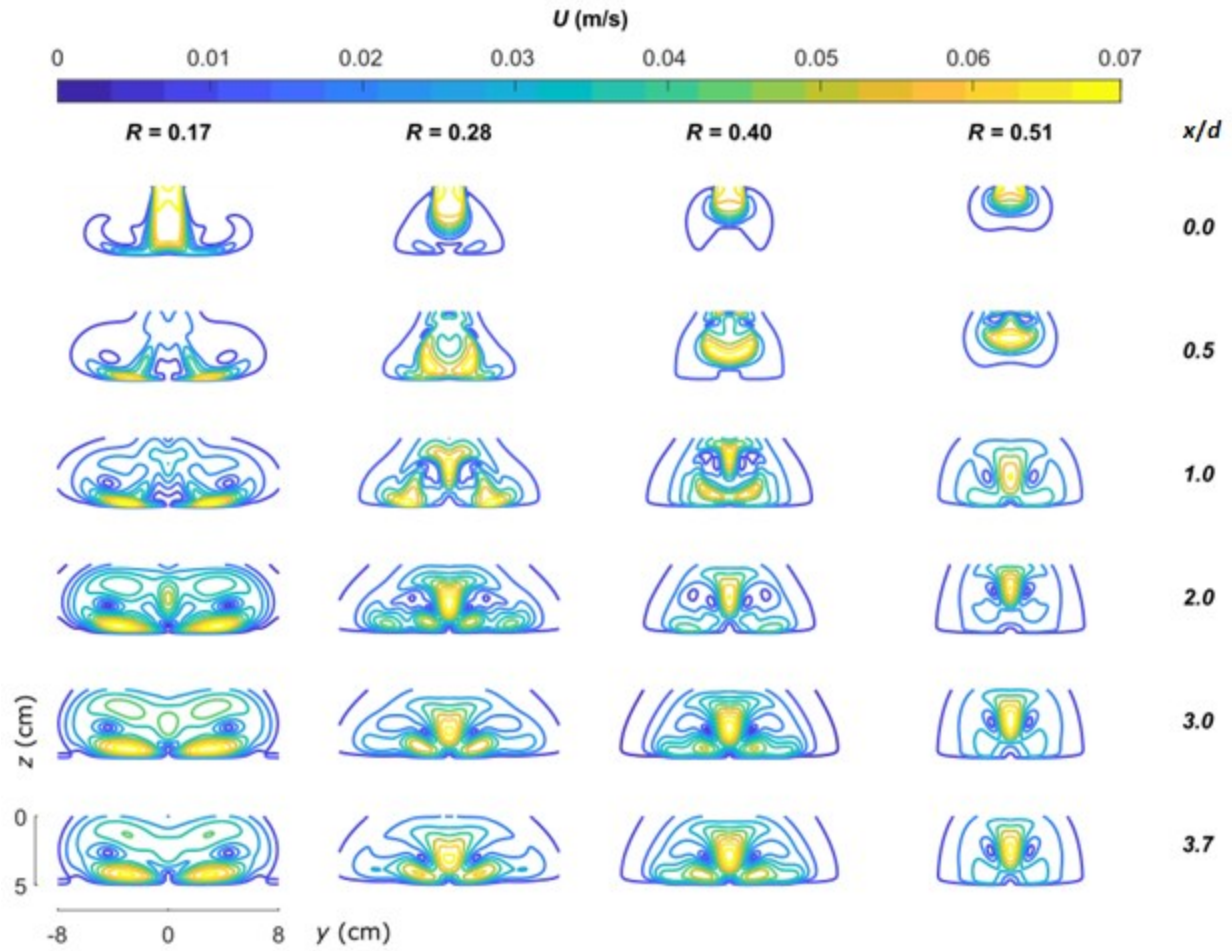
Figure 6.8: Velocity contours of the translating jet at sections normal to the impingement wall for $R = 0.17$ to 0.51 and $x/d = 0$ to 3.7.
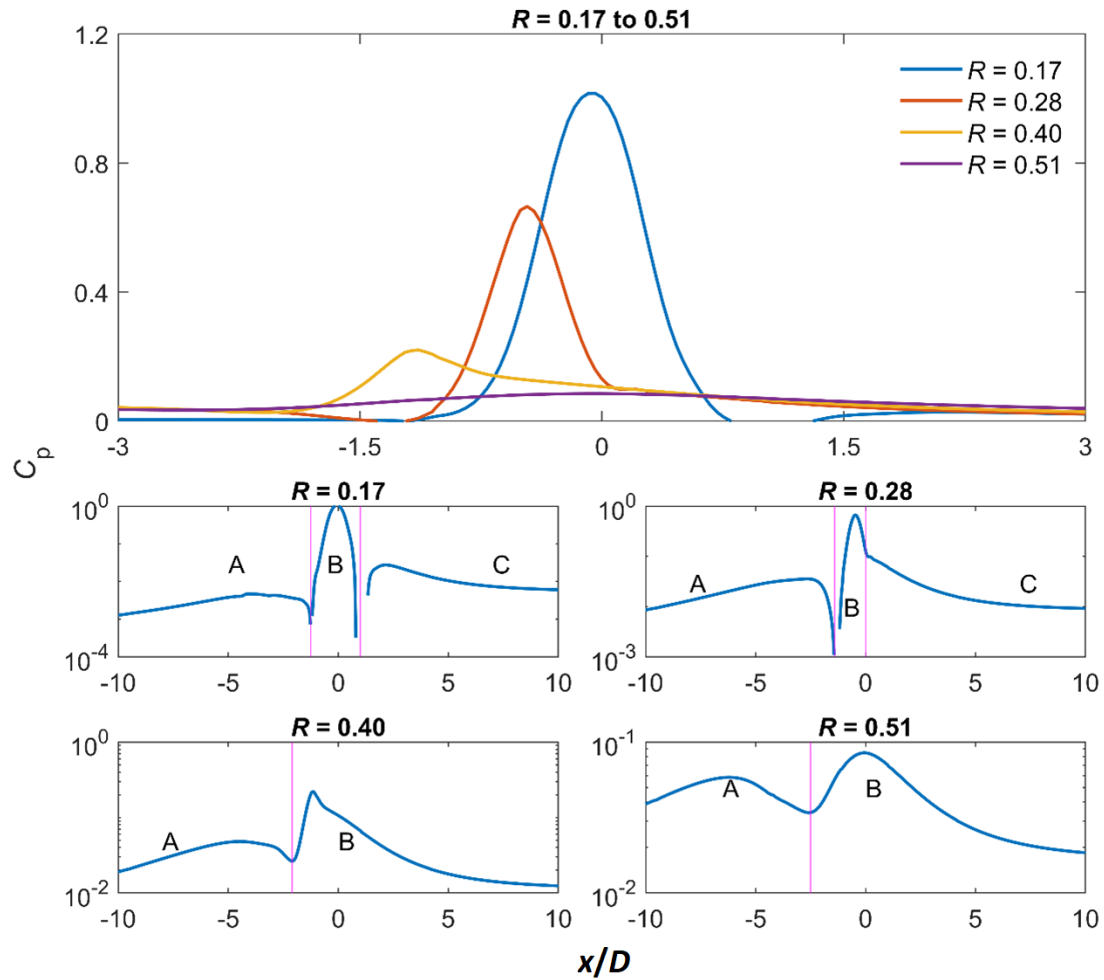
Figure 6.9: Distribution of the pressure coefficient C_p on the impingement wall along the jet translation. Red vertical lines demarcate the boundaries between different flow regions. Regions A, B, and C represent deflected jet, impingement, and recirculation regions, respectively.
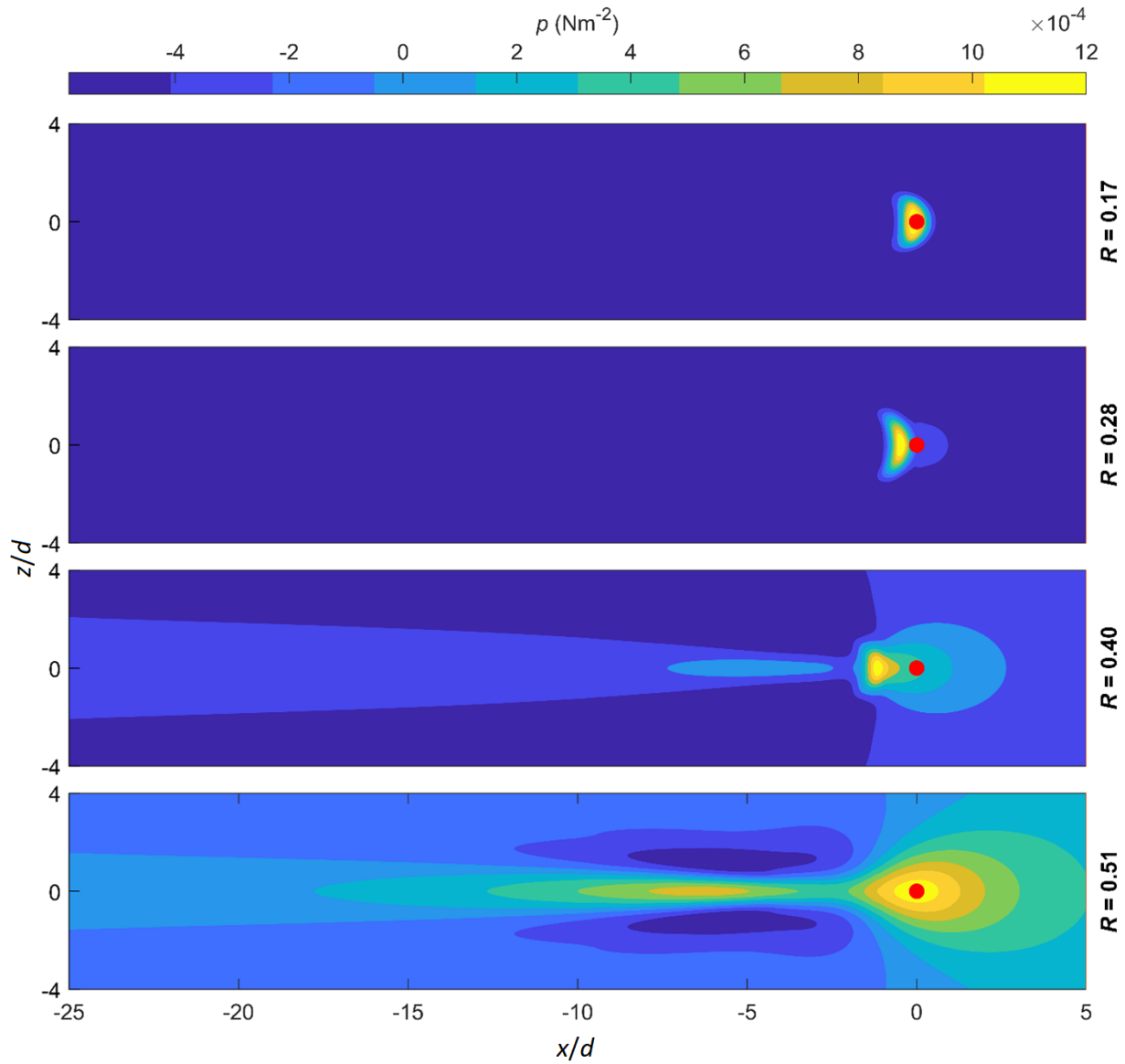
Figure 6.10: Distribution of wall pressure at the impingement wall for $U_t = 0.17$ to 0.51 m/s. Red dot denotes the position of the jet nozzle. The jet is translating to the right along x- axis.
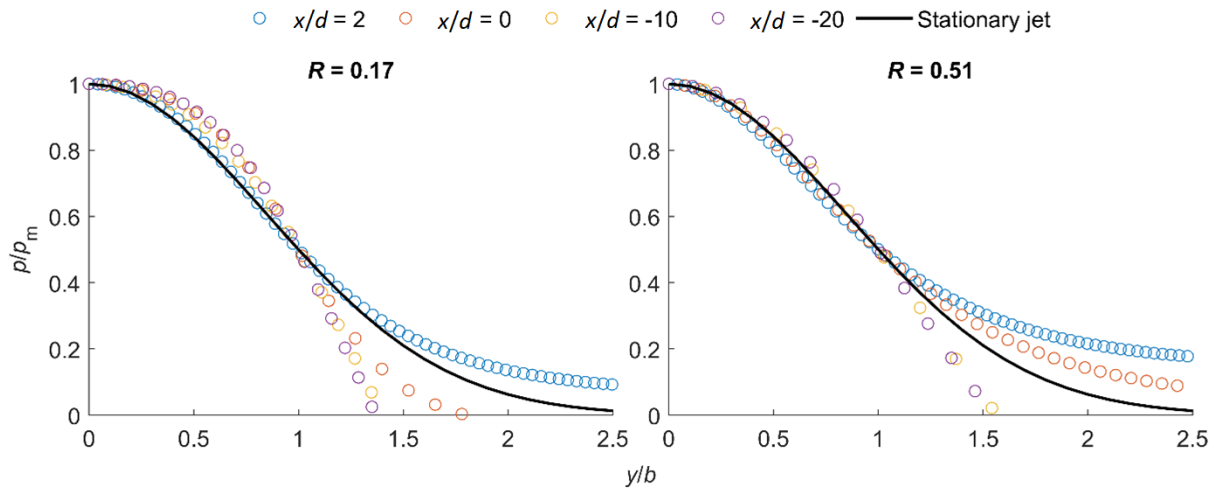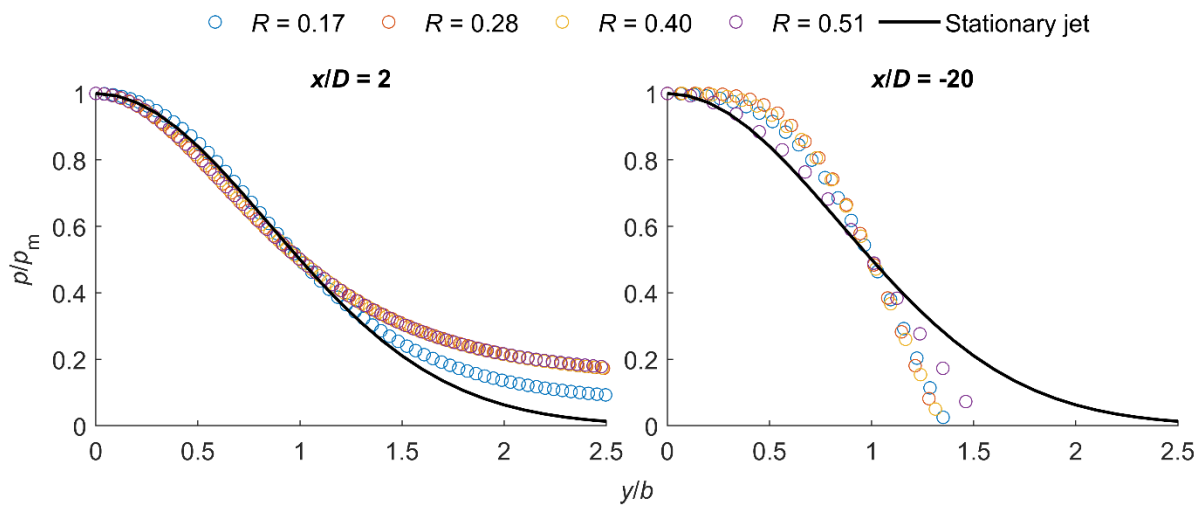
Figure 6.11: Dimensionless wall pressure distribution in the transverse direction of jet translation: (a) pressure profiles for $x/d = 2$ to -20; and (b) pressure profiles for $R = 0.17$ and 0.51.
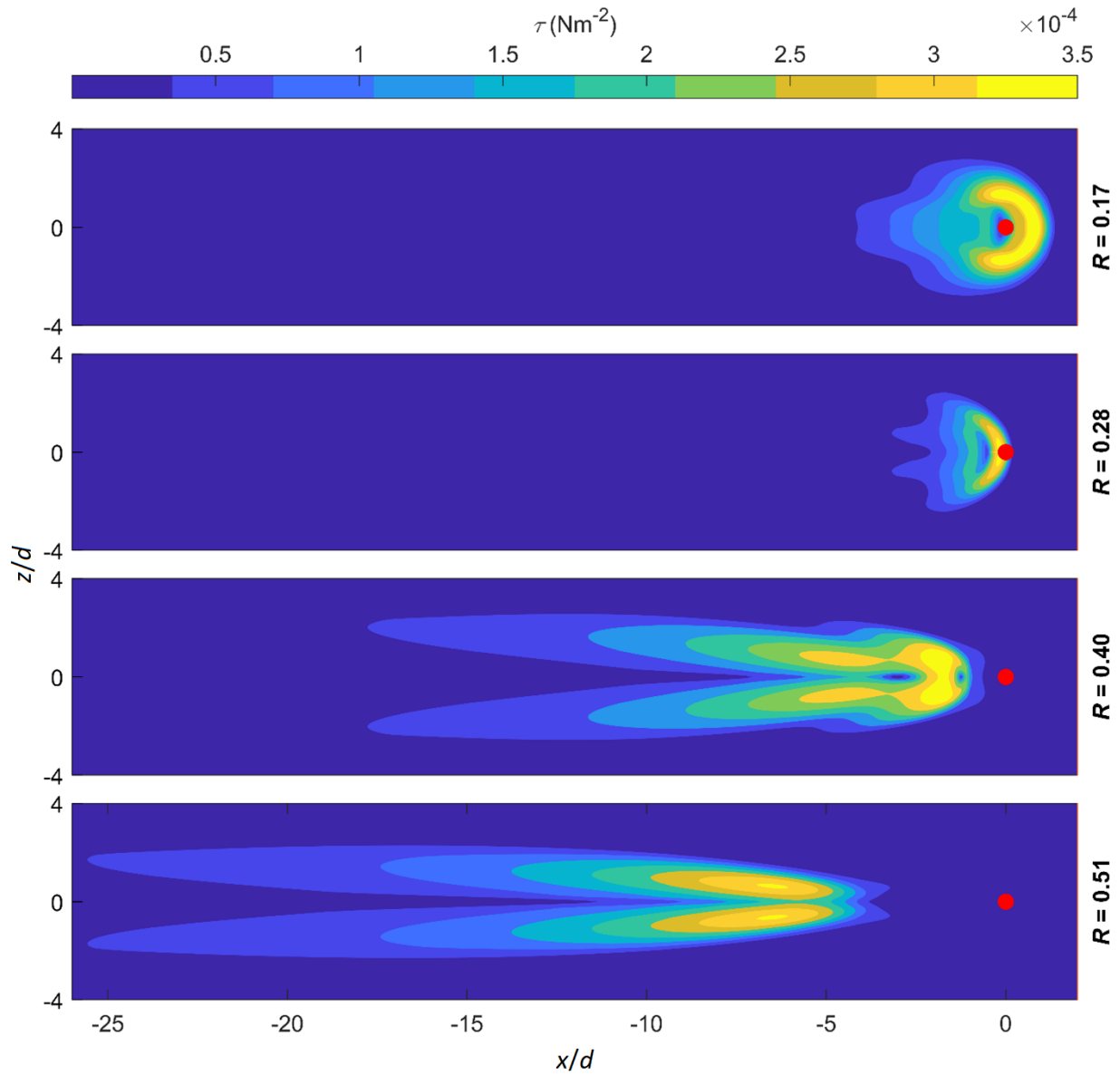
Figure 6.12: Distribution of wall shear stress at the impingement wall for $U_t = 0.17$ to 0.51 m/s. Red dot denotes the position of the jet nozzle. The jet is translating to the right along x- axis.
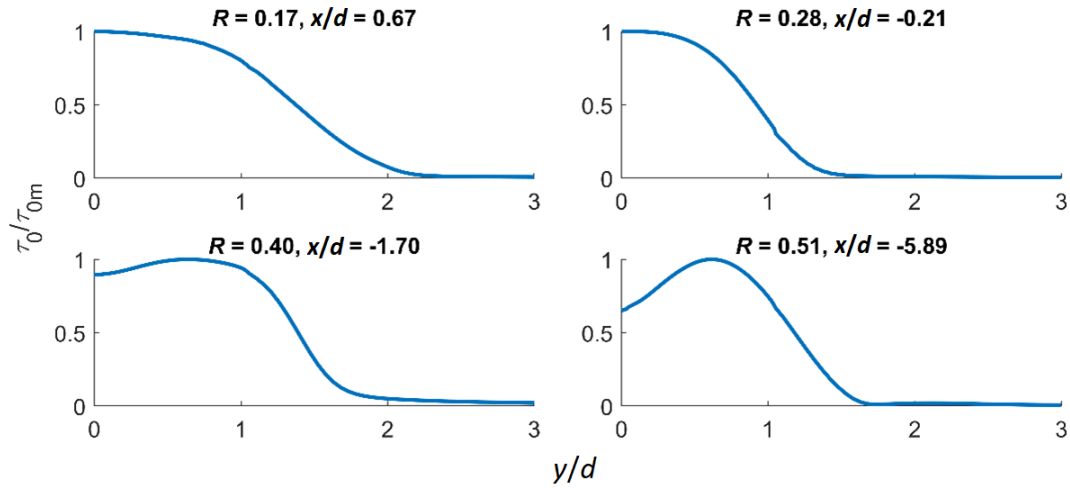
(a)
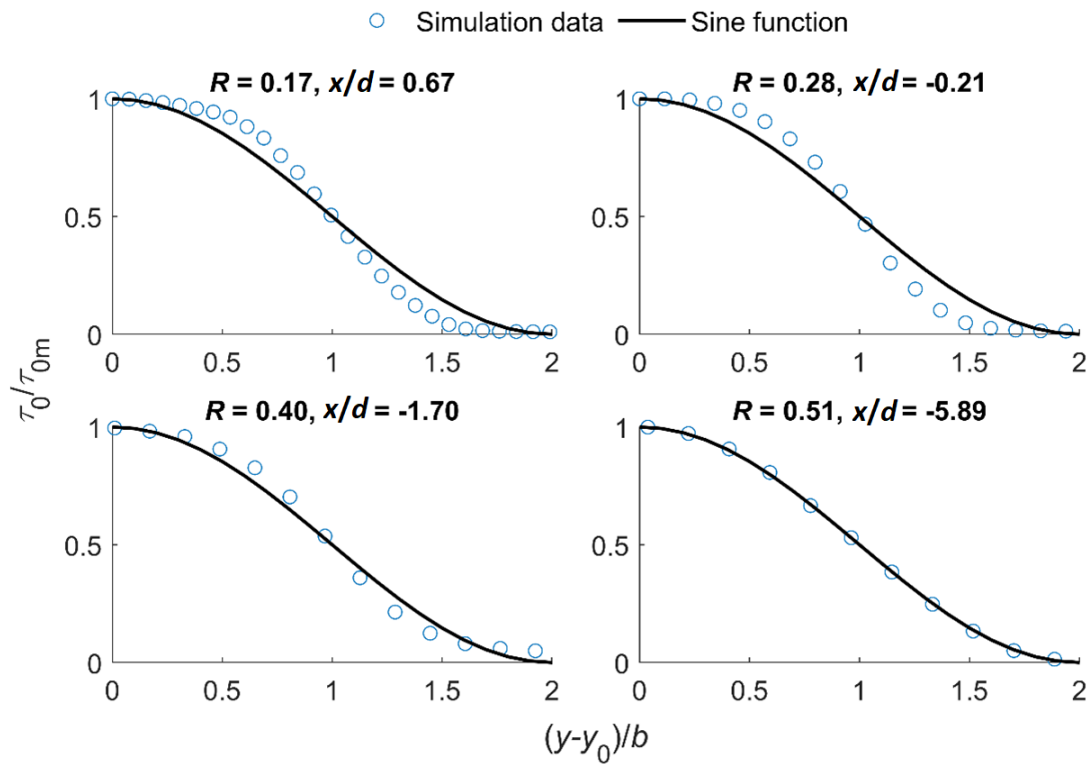
(b)

Figure 6.13: Wall shear stress distribution profile in the transverse direction of the jet translation and through the location of the maximum wall shear stress: (a) dimensionless plots, (b) similarity of the distributions after the location of the maximum wall shear stress.

CHAPTER 7. CONCLUSIONS AND RECOMMENDATIONS

7.1 General Conclusions

Turbulent jets are used in many industrial processes and have applications in several engineering problems. However, contemporary knowledge of turbulent jets is mainly limited to stationary turbulent jets and lacks the understanding of translating turbulent jets. This thesis attempted to contribute to three crucial applications of circular turbulent jets: (1) scouring of sand beds by stationary and translating jets, (2) air entrainment by plunging translating jets in a quiescent waterbody, and (3) impingement of a submerged translating jet on a flat wall. Following are the general conclusions of this thesis:

1. Scouring of Sand Beds by Short-Impinging Turbulent Jets: An experimental study was conducted to study the scouring of sand beds by submerged circular turbulent jets of short impinging height of 5.5 times the jet diameter. Experimental results showed that the scouring experiments by long and short jets are quite different. Semi-empirical prediction equations for the characteristic dimensions of the scour hole in the asymptotic state were developed, covering both long and short impinging jet regimes. Further, an expression for the asymptotic dynamic scour depth was developed, which was absent in previous studies. Lastly, empirical equations for the temporal development of the scour hole were developed.

2. Erosion of Sand Beds by Translating Turbulent Jets: This work showed an experimental study of the erosion of sand beds by translating submerged circular turbulent jets impinging at different inclinations. Experimental results showed that static scour is minimal for translating jet scouring. Therefore, dynamic scour is a critical characteristic for most practical purposes. The similarity in the dynamic scour profiles at constant impingement angles and different jet translating velocities were found, and empirical equations for the scour hole profiles for different jet impingement angles were developed. Furthermore, empirical prediction equations were developed for the maximum scour depth as a function of the jet translating velocity and impingement angle. The analysis of the sediment kinematics using particle image velocimetry (PIV) technique revealed that a principal vortex resides inside the scour hole along with a few minor vortices and plays a vital role in sand transport. Further, the horizontal velocity component was found to be the significant

component for sand transport due to the horizontal translation of the jet, which can be expressed as a Gaussian expression.

3. Air Entrainment by Translating Turbulent Plunging Jets: In this work, the mechanism of air bubble entraiment in a quiescent water tank by translating plunging circular jets was studied experimentally using shadowgraph and bubble image velocimetry (BIV) technique. Depending on the magnitude of the translating velocity, air entrainment was found to occur at the cusp of the cavity formed by the jet impact and at the upstream jet-water contact meniscus or at the cavity only. Highly unsteady shear-layer vortices were observed on the cavity's windward side, and a regular coherent structure of bubble swarm was observed on the leeward side. The Strouhal number of the coherent structure was comparable with vortex shedding by bridge piers. The probability distribution of the bubble diameters showed that the bubble size gets affected by the jet translating velocity. The maximum penetration depth of the bubble was found to be a function of the jet translating velocity and the interaction between the viscous drag force and surface tension of the air-water interface. Therefore, an equation for the maximum penetration depth was developed by correlating the jet velocity ratio and the capillary number. The dimensionless trajectory of the bubble swarm was found similar, and a general expression was developed. The spatial distribution of the bubbles in the bubble swarm was found to follow a Gaussian distribution, identical to the void fraction of bubbly jets in crossflow. Lastly, the bubbles' terminal rising velocity was unaffected by the jet translating velocity.

4. Impingement of Translating Turbulent Jets on a Flat Wall: This work showed a combined experimental and numerical study of the impingement of a translating submerged circular turbulent jet on a flat wall using particle image velocimetry (PIV) and computational fluid dynamics (CFD) techniques, respectively. Analysis of the mean velocity field showed a reduction of the potential core with translating velocity, and an expression for the length of the potential core was developed. Depending on the magnitude of the jet translating velocity, a high-velocity jet core and a counter-rotating vortex pair (CVP) were observed in the cross-sections of the jet. The CVP disrupted the formation of the wall jet at the leeward side after the impingement region. Based on the relative pressure distribution, three flow regions were identified: the impingement region, the deflected jet region, and the recirculation region. However, at bigger translating velocities, the recirculation region collapsed into the

impingement region. The maximum wall pressure and shear stress were reduced with translating velocity. As the translating velocity increased, the wall shear stress distribution evolved from a crescent shape to a fly-wing shape, with a low shear region at the axis of symmetry. Wall shear stress distribution at the transverse direction of the jet translation was found similar, and an expression for the distribution was developed.

7.2 Recommendations for Future Research

A limited number of studies have been conducted on translating turbulent jets compared to stationary ones. However, opportunities exist to broaden our understanding of translating jets to apply the acquired knowledge in potential engineering applications. Some recommendations for future research are described below.

1. Analytical Study: This thesis contains an experiment and numerical study of the impingement of a translating jet. However, the mechanics of a jet in crossflow and the impingement of a stationary jet were well-investigated in previous studies. Therefore, developing an analytical model to explain the mean flow field resulting from a translating jet impingement is plausible. This will also help simplify the governing equations of related CFD models for better convergence.

2. Experimental Study: Some industrial applications require the impingement of plane jets, e.g., cooling of sheet metals. One can follow the experimental setup for circular jet impingement described in this thesis and replace the jet with a plane jet to conduct an experimental study. Besides, a plane jet's flow field is simpler than a circular jet since the flow is two-dimensional. This helps to conduct PIV experiments only in a single plane to reveal most of the salient flow features.

3. Computational Study: A steady-state simulation was conducted in this thesis to reveal the mean flow features for the impingement of a translating jet. However, a short-impinging circular translating jet acts as a columnar obstacle to a crossflow, similar to a cylinder in a crossflow. Therefore, depending on the magnitude of the translating velocity, oscillatory behavior of the jet in relative crossflow and vortex shedding in the wake region can be observed. Therefore, a transient CFD model with large eddy simulation (LES) will be

instrumental in revealing all these exciting features of the impingement of translating jets.

Furthermore, there are still research gaps in the area of sediment transport by stationary circular oblique jets. Understanding the sediment kinematics will facilitate accurately assessing the temporal development and asymptotic dimensions of a scour hole on a sand bed. A study can be carried out for sand bed scouring by stationary circular oblique jets with an experimental setup similar to the one with translating circular jets (Chapter 4) to reveal the sand motion inside the scour hole.

BIBLIOGRAPHY

Adduce, C., and La Rocca, M. (2006). Local scouring due to turbulent water jets downstream of a trapezoidal drop: laboratory experiments and stability analysis. Water Resources Research, 42(2), W02405.

Adduce, C., and Sciortino, G. (2006). Scour due to a horizontal turbulent jet: numerical and experimental investigation. Journal of Hydraulic Reaserch, 44(5), 663-673.

Aderibigbe, O. O., and Rajaratnam, N. (1996). Erosion of loose beds by submerged circular impinging vertical turbulent jets. Journal of Hydraulic Research, 34(1), 19–33.

Ahmed, S., Ye, Y., Liu, H., and Rajaratnam, N. (2018). Preliminary study of surface hydraulic jumps. ASCE Journal of Irrigation and Drainage Engineering, 145(3), 06019001.

Amin, M. R. (2016). Development of scour in cohesive soils by normal impingement of a submerged circular turbulent jet. M.Sc. Thesis, University of Saskatchewan, Saskatoon, Canada.

Amin, M. R. (2018). Discussion of "Using an improved jet-erosion test to study the influence of soil parameters on the erosion of a silty soil" by Van-Nghia Nguyen, Jean-Robert Courivaud, Patrick Pinettes, Hanène Souli, and Jean-Marie Fleureau. Journal of Hydraulic Engineering, 144(11), 07018014.

Amin, M. R., Rajaratnam, N., and Zhu, D. (2019). Energy loss below rectangular sharp-crested weirs for free flows. Proc. 38th IAHR World Congress, Panama City, Panama, pp. 1-7.

Amin, M. R., Rajaratnam, N., and Zhu, D. Z. (2021). Scouring of sand beds by short impinging turbulent jets. Proceedings of the Institution of Civil Engineers - Water Management, 174(6), 309–320.

Ansari, S. A. , Kothyari, U. C., and Raju, K. G. R. (2003). Influence of cohesion on scour under submerged circular vertical jets. ASCE Journal of Hydraulic Engineering, 129(12), 1014–1019.

Ashforth-Frost, S., and Jambunathan, K. (1996). Effect of nozzle geometry and semi-confinement on the potential core of a turbulent axisymmetric free jet. International Communications in Heat and Mass Transfer, 23(2), 155–162.

Azimi, A. H., Rajaratnam, N., and Zhu, D. Z. (2016). Water Surface Characteristics of Submerged Rectangular Sharp-Crested Weirs. Journal of Hydraulic Engineering, 142(5), 06016001.

Barczewski, B. H., Gangadharaiah, T., Kobus, H. E., Rao, N. S. L. (1975). Characteristics of self-aerated free-surface flows. Berlin, pp. 224.

Baylar, A., Emiroglu, M.E. and Mualla, O. (2006). The development of aeration performance with different typed nozzles in a vertical plunging water jet system. International Journal of Science and Technology, 1(1), pp. 51–63.

Beltaos, S. (1976). Oblique impingement of circular turbulent jets. Journal of Hydraulic Research, 14(1), 1976.

Beltaos, S., and Rajaratnam, N. (1974). Impinging circular turbulent jets. Journal of the Hydraulics Division, 100(10), 1313–1328.

Beltaos, S., and Rajaratnam, N. (1977). Impingement of axisymmetric developing jets. Journal of Hydraulic Research, 15(4), 311–326.

Berghe, J.-F. Vanden, Pyrah, J., Gooding, S., and Capart, H. (2011). Development of a jet trenching model in sand. Frontiers in Offshore Geotechnics II - Proceedings of the 2nd International Symposium on Frontiers in Offshore Geotechnics, 889–894.

Biń, A. K. (1993). Gas entrainment by plunging liquid jets. Chemical Engineering Science, 48(21), 3585–3630.

Bombardelli, F. A., and Gioia, G. (2006). Scouring of granular beds by jet-driven axisymmetric turbulent cauldrons. Physics of Fluids, 18(8), 088101.

Bombardelli, F. A., Palermo, M., and Pagliara, S. (2018). Temporal evolution of jet induced scour depth in cohesionless granular beds and the phenomenological theory of turbulence. Physics of Fluids, 30(8), 085109.

Calomino, F., Gabelli, G., and Miglio, A. (2007). Water jetting for sewer cleansing- First experimental results for efficiency in non-cohesive sediment removal. In proceedings of the 6th International Conference on Sustainable Techniques and Strategies for Urban Water Management, Lyon, France, pp. 1309–1316.

Chakravarti, A., Jain, R. K., and Kothyari, U. C. (2014). Scour under submerged circular vertical jets in cohesionless sediments. ISH Journal of Hydraulic Engineering, 20(1), 32–37.

Chamani, M. R., Rajaratnam, N. (2008). Turbulent jet energy dissipation at vertical drops. ASCE Journal of Hydraulic Engineering, 134(10), 1532-1535.

Chanson, H. (1996). Air bubble entrainment in free-surface turbulent shear flows. Academic Press, San Diego.

Chanson, H. (1997). Air bubble entrainment in open channels: Flow structure and bubble size distributions. International Journal of Multiphase Flow, 23(1), 193–203.

Chanson, H. and Lee, J. F. (1997). Plunging jet characteristics of plunging breakers. Coastal Engineering, 31(1–4), 125–141.

Chanson, H. and Manasseh, R. (2003). Air entrainment processes in a circular plunging jet: Void-fraction and acoustic measurements. Journal of Fluids Engineering, Transactions of the ASME, 125(5), 910–921.

Chirichella, D., Gómez-Ledesma, R., Kiger, K. T., and Duncan, J. H. (2002). Incipient air entrainment in a translating axisymmetric plunging laminar jet. Physics of Fluids, 14(2), 781–790.

Chow, V. T. (1959). Open channel hydraulics. McGraw-Hill, New York, Chap. 14.

Clarke, F. R. W. (1962). The action of submerged jets on Movable Material. MSc. thesis, University of London, UK.

Cornaro, C., Fleischer, a. ., and Goldstein, R. . (1999). Flow visualization of a round jet impinging on cylindrical surfaces. Experimental Thermal and Fluid Science, 20(2), 66–78.

Cumming, I. W. (1975). The impact of falling liquids with liquid surfaces. Ph.D. Thesis, Loughborough University of Technology, Loughborough, UK.

Cummings, P. D. and Chanson, H. (1997). Air entrainment in the developing flow region of plunging jets-part 2: Experimental. ASME Journal of Fluids Engineering, 119(3), 603–608.

Doddiah, D., Albertson, M. L., and Thomas, R. A. (1953). Scour from jets. In Proceedings of 5th IAHR Congress, International Association for Hydraulic Research, Minneapolis, pp. 161-169.

Ervine, D. A. and Falvey, H. T. (1987). Behaviour of Turbulent Water Jets in the Atmosphere and in Plunge Pools. Proceedings of the Institution of Civil Engineers, 83(1), 295–314.

Ervine, D. A., McKeogh, E. and Elsawy, E. M. (1980). Effect of turbulence intensity on the rate of air entrainment by plunging water jets. Proceedings of the Institutions of the Civil Engineers, 69(2), 425–445.

Evans, G. M., Jameson, G. J. and Atkinson, B. W. (1992). Prediction of the bubble size generated by a plunging liquid jet bubble column. Chemical Engineering Science, 47, 3265–3272.

Fairweather, M., and Hargrave, G. (2002). Experimental investigation of an axisymmetric, impinging turbulent jet. 1. Velocity field. Experiments in Fluids, 33(3), 464–471.

Fenot, M., Dorignac, E., and Vullierme, J. J. (2008). An experimental study on hot round jets impinging a concave surface. International Journal of Heat and Fluid Flow, 29(4), 945–956.

Freedman, D. and Diaconis, P. (1981). On the histogram as a density estimator: L2 theory. Probability Theory and Related Fields, 57, 453–476.

Ghaneeizad, S. M., Atkinson, J. F., and Bennett, S. J. (2015). Effect of flow confinement on the hydrodynamics of circular impinging jets: implications for erosion assessment. Environmental Fluid Mechanics, 15(1), 1–25.

Giger, M., Dracos, T. and Jirka, G. H. (1991). Entrainment and mixing in plane turbulent jets in shallow water. Journal of Hydraulic Research, 29(5), 615–642.

Gioia, G., and Bombardelli, F. A. (2005). Localized turbulent flows on scouring granular beds. Physical Review Letters, 95(1), 1–4.

Giralt, F., Chia, C., and Trass, O. (1977). Characterization of the impingement region in an axisymmetric turbulent jet. Industrial and Engineering Chemistry Fundamentals, 16(1), 21–28.

Gómez-Ledesma, R., Kiger, K. T. and Duncan, J. H. (2011). The impact of a translating plunging jet on a pool of the same liquid. Journal of Fluid Mechanics, 680, 5–30.

Gu, L., Ni, F., Xu, L., and Li, Z. (2018). Determining the threshold pressure of clay-cutting by a mobile jet for coastal construction. Journal of Coastal Research, 34(5), 1209–1215.

Guan, D., Melville, B., and Friedrich, H. (2016). Local scour at submerged weirs in sand-bed channels. Journal of Hydraulic Research, 54(2), 172-184.

Guerra, D. R. S., Su, J., and Silva Freire, A. P. (2005). The near wall behavior of an impinging jet. International Journal of Heat and Mass Transfer, 48(14), 2829–2840.

Guyot, G., Cartellier, A., and Matas, J. P. (2019). Depth of penetration of bubbles entrained by an oscillated plunging water jet. Physics of Fluids, 9(7), 1864-1866.

Haehnel, R. B., Cushman-Roisin, B., and Dade, W. B. (2006) Cratering by a subsonic jet impinging on a bed of loose particles. In Proceedings of Earth and Space 2006, ASCE, Houston, pp. 1-8.

Haehnel, R. B., Dade, W. B., and Cushman-Roisin, B. (2008). Crater evolution due to a jet impinging on a bed of loose particles. In Proceeding of Earth and Space 2008, Reston, VA, 10p.

Hanson, G. J., and Cook, K. R. (1997). Development of excess shear stress parameters for circular jet testing. ASAE Paper No. 97-2227, American Society of Agricultural Engineers, St. Joseph, MI, 21p.

Hashiehbaf, A., Baramade, A., Agrawal, A., and Romano, G. P. (2015). Experimental investigation on an axisymmetric turbulent jet impinging on a concave surface. International Journal of Heat and Fluid Flow, 53, 167–182.

Hassan, M., Assoum, H. H., Martinuzzi, R., Sobolik, V., Abed-Meraim, K., and Sakout, A. (2013). Experimental investigation of the wall shear stress in a circular impinging jet. Physics of Fluids, 25(7), 077101.

Jahromi, M. E. and Khiadani, M. (2017). Experimental study on oxygen transfer capacity of water jets discharging into turbulent cross-flow. Journal of Environmental Engineering, 143(6), 04017007.

Jalil, A., and Rajaratnam, N. (2006). Oblique impingement of circular water jets on a plane boundary. Journal of Hydraulic Research, 44(6), 807–814.

Johnson, M. C. (2000). Discharge coefficient analysis for flat-topped and sharp-crested weirs. Irrigation Science, 19, 133–137.

Kandaswamy, P. K., and Rouse, H. (1957). Characteristics of flow over terminal weirs and sills. ASCE Journal of Hydraulics Division, 83(4), 1-13.

Katopodes, N. D. (2019). Free-surface flow: environmental fluid mechanics. Leiden, Netherlands.

Kawagoshi, N., and Hagar, W. H. (1990). B-Jump in sloping channel II. IAHR Journal of Hydraulic Research, 28(4), 461-480.

Kiger, K. T. and Duncan, J. H. (2011). Air-entrainment mechanisms in plunging jets and breaking waves. Annual Review of Fluid Mechanics, 44, 563–596.

Kindsvater, C. E., and Carter, R. W. (1957). Discharge characteristics of rectangular thin-plate weirs. ASCE Journal of Hydraulics Division, 83(6), 1–36.

Lasheras, J. C., and Tio, K. K. (1994). Dynamics of a small spherical particle in steady two-dimensional vortex flows. Applied Mechanics Reviews, 47(6), S61–S69.

Lee, J. H. W., and Chu, V. H. (2003). Turbulent jets and plumes: a Lagrangian approach. Kluwer Academic Publishers, Norwell, Massachusetts, USA, 390p.

Lim, H. J., Chang, K. A., Huang, Z. C., and Na, B. (2015). Experimental study on plunging breaking waves in deep water. Journal of Geophysical Research: Oceans, 120(3), 2007–2049.

Looney, M. K., and Walsh, J. J. (1984). Mean-flow and turbulent characteristics of free and impinging jet flows. Journal of Fluid Mechanics, 147(7), 397–429.

Mahesh, K. (2013). The interaction of jets with crossflow. Annual Review of Fluid Mechanics, 45, 379–407.

Manning, J. H. (1959). Commercial and biological uses of Maryland clam dredge. In proceedings of the 12th Annual Gulf and Caribbean Fisheries Institute. Gulf and Caribbean Fisheries Institute, Coral Gables, FL, USA, pp. 61–67.

Margason, R. J. (1968). The path of a jet directed at large angles to a subsonic stream. N.A.S.A., TN.D.-4919, Langley Research Center, Hampton, Virginia.

Margason, R. J. (1993). Fifty years of jet in crossflow research. Computational and Experimental Assessment of Jets in Cross Flow. AGARD-CP 534, Advis. Group Aeronaut. Res. Dev., Washington, DC.

Maxworthy, T., Gnann, C., Kürten, M., and Durst, F. (1996). Experiments on the rise of air bubbles in clean viscous liquids. Journal of Fluid Mechanics, 321, 421–441.

Mazurek, K. A. (2001). Scour of clay by jets. Ph.D. Thesis, University of Alberta, Edmonton, Canada.

Mazurek, K. A., and Hossain, T. (2007). Scour by jets in cohesionless and cohesive soils. Canadian Journal of Civil Engineering, 34(6), 744-751.

Mazurek, K. A., Rajaratnam, N., and Sego, D. C. (2001). Scour of cohesive soil by submerged circular turbulent impinging jets. ASCE Journal of Hydraulic Engineering, 127(7), 598-606.

McKeogh, E. J. and Ervine, D. A. (1981). Air entrainment rate and diffusion pattern of plunging liquid jets. Chemical Engineering Science, 36(7), 1161–1172.

Mih, W. C., and Kabir, J. (1983). Impingement of water jets on nonuniform streambed. ASCE Journal of Hydraulic Engineering, 109(4), 536–548.

Moore, W. L. (1943). Energy loss at the base of free overfall. Transactions of ASCE, 108, 1343-1360.

Morton, B. R. and Ibbetson, A. (1996). Jets deflected in a crossflow. Experimental Thermal and Fluid Science, 12(2), 112–133.

Neto, I. E. L., Zhu, D. Z. and Rajaratnam, N (2008b). Horizontal Injection of Gas–Liquid Mixtures in a Water Tank. ASCE Journal of Hydraulic Engineering, 134(12), 1722–1731.

Neto, I. E. L., Zhu, D. Z. and Rajaratnam, N. (2008a). Bubbly jets in stagnant water. International Journal of Multiphase Flow, 34(12), 1130–1141.

Nishino, K., Samada, M., Kasuya, K., and Torii, K. (1996). Turbulence statistics in the stagnation region of an axisymmetric impinging jet flow. International Journal of Heat and Fluid Flow, 17(3), 193-201.

Nobel, A. J. (2013). On the excavation process of a moving vertical jet in cohesive soil. Ph.D. Thesis, Delft University of Technology, Delft City, Nederland.

Oğuz, H. N. (1998). The role of surface disturbances in the entrainment of bubbles by a liquid jet. Journal of Fluid Mechanics, 372, 189–212.

Ohtsu, I., and Yasuda, Y. (1991). Hydraulic jump in sloping channels. ASCE Journal of Hydraulic Engineering, 117(7), 905-921.

Pagliara, S., Hager, W. H., and Unger, J. (2008). Temporal evolution of plunge pool scour. ASCE Journal of Hydraulic Engineering, 134(11), 1630–1638.

Palermo, M., Bombardelli, F. A., and Pagliara, S. (2018). From developing to developed phase in the scour evolution due to vertical and sub-vertical plunging jets: New experiments and theory. 7th IAHR International Symposium on Hydraulic Structures, 8p.

Perng, A. T. H., and Capart, H. (2008). Underwater sand bed erosion and internal jump formation by travelling plane jets. Journal of Fluid Mechanics, 595, 1–43.

Phares, D. J., Smedley, G. T., and Flagan, R. C. (2000). The inviscid impingement of a jet with arbitrary velocity profile. Physics of Fluids, 12(8), 2046–2055.

Pope, S. B. (2000). Turbulent Flows. Cambridge University Press, Cambridge, 771p.

Poreh, M., and Hefez, E. (1967). Initial scour and sediment motion due to an impinging jet. In Proceedings of the IAHR Congress, International Association for Hydraulic Research, Fort Collins, p. 8.

Poreh, M., Tsuei, Y. G., and Cermak, J. E. (1967). Investigation of a turbulent radial wall jet. Journal of Applied Mechanics, 34(2), 457–463.

Pratte, B. D., Baines, W. D. (1967). Profiles of the round turbulent jet in a crossflow. ASCE Journal of the Hydraulics Division, 93(6), 53–64.

Rajaratnam, N. (1967). Hydraulic jumps. Advances in Hydroscience: Volume 4, ed. V. T. Chow, Elsevier, New York.

Rajaratnam, N. (1976). Turbulent Jets. Elsevier, New York, 304p.

Rajaratnam, N., (1982). Erosion by submerged circular jets. ASCE Journal of Hydraulic Division, 108(2), 262-267.

Rajaratnam, N., and Beltaos, S. (1977). Erosion by impinging circular turbulent jets. ASCE Journal of the Hydraulics Division, 103(10), 1191–1205.

Rajaratnam, N., and Chamani, M. R. (1995). Energy loss at drops. Journal of Hydraulic Research, 33(3), 373-384.

Rajaratnam, N., and Flint-Petersen, L. (1989). Low reynolds number circular turbulent jets. In ICE Proceedings, 87, 299–305.

Rajaratnam, N., and Gangadharaiah, T. (1983). Vortex structure of circular jets in crossflow. Journal of Wind Engineering and Industrial Aerodynamics, 12(2), 155–164.

Rajaratnam, N., and Mazurek, K. A. (2003). Erosion of sand by circular impinging water jets with small tailwater. ASCE Journal of Hydraulic Engineering, 129(3), 225–229.

Rajaratnam, N., and Murahari, V. (1974). Flow characteristics of sloping channel jumps. ASCE Journal of Hydraulics Division, 100(6), 731-740.

Rajaratnam, N., and Muralidhar, D. (1969). Flow below deeply submerged rectangular weirs. Journal of Hydraulic Research, 7(3), 355–374.

Rajaratnam, N., and Pani, B. S. (1974). Three-dimensional turbulent wall jets. ASCE Journal of the Hydraulics Division, 100(1), 69–83.

Rajaratnam, N., Zhu, D. Z., and Rai, S. P. (2010). Turbulence measurements in the impinging region of a circular jet. Canadian Journal of Civil Engineering, 37(5), 782–786.

Ramamurthy, A. S., Tim, U. S., Rao, M. V. J. (1987). Flow over sharp-crested plate weirs. ASCE Journal of Irrigation and Drainage Engineering, 113(2), 163–172.

Rand, W. (1955). Flow geometry at straight drop spillways. Proc. of ASCE, 81(791), pp. 1-13.

Rehbock, T. (1929). Discussion of precise weir measurements by EW Schoder and KB Turner. Transactions of ASCE, 93, 1143–1162.

Rockwell, P. K. (1981). Water jet trenching in submerged clays. In proceedings of 1st U.S. Water Jet Conference, St. Louis, 12 p.

Rouse, H. (1936). Discharge characteristics of the free overfall. ASCE Civil Engineering, 6(4), 257–260.

Rouse, H. (1939). Criteria for similarity in the transportation of sediment. In Proceedings of 1st Hydraulic Conference, University of Iowa, pp. 33–49.

Roy, A. K., Maiti, B. and Das, P. K. (2013). Visualisation of air entrainment by a plunging jet. In International Conference on Thermal Engineering, pp. 468–473.

Ryu, Y., Chang, K. A. and Lim, H. J. (2005). Use of bubble image velocimetry for measurement of plunging wave impinging on structure and associated greenwater. Measurement Science and Technology, 16(10), 1945–1953.

Sarma, K. V. N. (1967). Study of scour phenomenon and its functional form. PhD thesis, Indian Institute of Sciences, India.

Schneider, C. A., Rasband, W. S. and Eliceiri, K. W. (2012). NIH Image to ImageJ: 25 years of image analysis. Nature Methods, 9(7), 671–675.

Schoen, J. J. (2014). Removal of a dumped rock cover with a low pressure jet. M.Sc. Thesis. Delft University of Technology, Delft City, Nederland.

Sene, K. J. (1988). Air entrainment by plunging jets. Chemical Engineering Science, 43(10), 2615–2623.

Settles, G. S. and Hargather, M. J. (2017). A review of recent developments in schlieren and shadowgraph techniques. Measurement Science and Technology, 28(4).

Shuai, Y. et al. (2019). Characterization of the bubble swarm trajectory in a jet bubbling reactor. AIChE Journal, 65(5), 1–11.

Si, J. H., Lim, S. Y., and Wang, X. K. (2018). Flow structures in evolving scour holes caused by a plunging jet downstream of a weir. ASCE Journal of Hydraulic Engineering, 144(6), 04018018.

Si, J. H., Lim, S. Y., and Wang, X. K. (2019). Jet-Flipping in scour hole downstream of unsubmerged weir with apron. ASCE Journal of Hydraulic Engineering, 145(10), 04019035.

Smith, S. H., and Mungal, M. G. (1998). Mixing, structure, and scaling of the jet in crossflow. Journal of Fluid Mechanics, 357, 83–122.

Stenstrom, M. K. and Gilbert, R. G. (1981). Effects of alpha, beta and theta factor upon the design, specification and operation of aeration systems. Water Research, 15(6), 643–654.

Su, J. C., Perng, A. T. H., and Hervé, C. (2007). Underwater trench incision and turbid overspill due to moving point jets. In IAHR (Ed.), XXXII Congress IAHR (pp. 1–10).

Sullivan, N. (2000) The use of agitation dredging, water injection dredging and sidecasting: Result of a survey of ports in England and Wales. Terra Aqua 78: 11–20.

Swamee, P. K., (1988). Generalized Rectangular Weir Equation. ASCE Journal of Hydraulic Engineering, 114(8), 945–949.

Thielicke, W. and Sonntag, R. (2021). Particle Image Velocimetry for MATLAB: Accuracy and enhanced algorithms in PIVlab. Journal of Open Research Software, 9, 1–14.

Unger, J., and Hager, W. H. (2005). Discussion on "The mean characteristics of horseshoe vortex at a cylindrical pier by By M. Muzzammil and T. Gangadhariah. Journal of Hydraulic Research, 43(5), 584–587.

Unger, J., and Hager, W. H. (2006). Temporal flow evolution of sediment embedded circular bridge piers. In proceedings of the International Conference on Fluvial Hydraulics - River Flow 2006, 11p.

Unger, J., and Hager, W. H. (2007). Down-flow and horseshoe vortex characteristics of sediment embedded bridge piers. Experiments in Fluids, 42(1), 1–19.

Weegenaar, R. A., Keetels, G. H., Winkelman, M. O., and Rhee, C. Van. (2015). Sand erosion with a traversing circular jet. In proceedings of the Institution of Civil Engineers, Maritime Engineering, 168(MA2), 76–83.

Westrich, B., and Kobus, H. (1973). Erosion of a Uniform Sand Bed by Continuous and Pulsating Jets. In International Association for Hydraulic Research Congress (Vol. 1). Istanbul, Turkey, 8p.

Wu, S., and Rajaratnam, N. (1996). Submerged flow regimes of rectangular sharp-crested weirs. ASCE Journal of Hydraulic Engineering, 122(7), 412-414.

Xie, Y., Li, P., Lan, J., and Zhang, D. (2013). Flow and heat transfer characteristics of single jet impinging on dimpled surface. ASME. J. Heat Transfer, 135(5), 052201.

Yeh, P. H., Chang, K. A., Henriksen, J., Edge, B., Chang, P., Silver, A., and Vargas, A. (2009). Large-scale laboratory experiment on erosion of sand beds by moving circular vertical jets. Ocean Engineering, 36(3–4), 248–255.

Zhang, D., Qu, H., Lan, J., Chen, J., and Xie, Y. (2013). Flow and heat transfer characteristics of single jet impinging on protrusioned surface. International Journal of Heat and Mass Transfer, 58(1–2), 18–28.

Zhang, S., Ge, T., Zhao, M., and Wang, C. (2017). The prediction of traveling jet trenching in stiff clay based on the erosion failure mechanism. Marine Georesources and Geotechnology, 35(7), 939-945.

Zhang, S., Wang, C., and Ge, T. (2017). Experimental prediction of the noncontact jet Trencher's excavation depth in clay. Marine Georesources and Geotechnology, 35(2), 300–304.

Zhang, S., Zhao, M., Ge, T., and Wang, C. (2016). Experimental Research on Trenching in Stiff Clay by Submerged Vertical Traveling Jets. Journal of Coastal Research, 32(2), 365–373.

Zhang, W. and Zhu, D. Z. (2013). Bubble characteristics of air-water bubbly jets in crossflow. International Journal of Multiphase Flow, 55, 156–171.

Zumbrunnen, D. A., Incropera, F. P., and Viskanta, R. (1989). Convective heat transfer distributions on a plate cooled by planar water jets. Journal of Heat Transfer, 111(4), 889–89.

APPENDIX: ESTIMATION OF THE FLOW AND ENERGY LOSS DOWNSTREAM OF RECTANGULAR SHARP-CRESTED WEIRS USING JET THEORY[†]

A.1 Introduction

The hydraulics of rectangular sharp-crested weirs have been studied extensively from the perspective of flow measurement (Rehbock, 1929; Rouse 1936; Kindsvater and Carter, 1957; Ramamurthy et al., 1987; Swamee, 1988; Johnson, 2000; and others). The flow varies from free flow for lower tailwater levels to submerged flow for sufficiently high tailwater levels. Another interesting aspect of this flow is the energy loss that occurs immediately downstream for free to fully submerged weir flows; this aspect has not been studied previously. This work considers in detail the flow and energy losses occurring immediately downstream of these weirs for the entire range of tailwater levels.

For free flow over rectangular sharp-crested weirs, the discharge per unit weir length, q, is given by

$$q = \frac{2}{3} C_d \sqrt{2g} h^{3/2} \tag{A.1}$$

where h is the upstream water level above the weir, g is the gravitational acceleration, and C_d is the coefficient of discharge, described well by the equation below (Kandaswamy and Rouse, 1957)

$$C_d = 0.605 + 0.08 \left(\frac{h}{P}\right) \qquad \text{for } 0 < h/P < 6 \tag{A.2}$$

where P is the height of the weir crest above the bed of the approach flow channel. As shown in Figure A.1a, when the tailwater depth y_t above the bed of the downstream channel approaches the crest level, the flow over the weir becomes submerged and a higher head is required to pass the

---

same discharge. Wu and Rajaratnam (1996) found that when the tailwater level t rises above the weir crest the flow gets submerged ($t = y_t - P > 0$), and changes from an impinging jet to a surface flow regime (Figure A.1b). The surface flow regime changes from a surface jump to a surface wave and finally to a surface jet as t increases. The surface jet was studied by Rajaratnam and Muralidhar (1969) and the surface jump by Ahmed et al. (2018).

Considering free flow in Figure A.1a (water surface 1), which occurs for relatively low tailwater depths, the falling nappe from the weir gets deflected by the bed which turns the falling nappe into a horizontal supercritical stream. Because of the formation of the pool behind the ventilated nappe and its turbulent interaction with the nappe, the supercritical stream has a non-uniform velocity profile (Moore, 1943). As the tailwater depth increases, a hydraulic jump is formed at a certain stage (water surface 2), and for higher tailwater depths, the toe of the jump forms on the falling nappe (water surfaces 3 and 4), similar to a jump on a steep slope (Amin et al., 2019). Further, the difference between the depth of the pool behind the nappe and the tailwater level disappears. Then, as the tailwater level approaches that of the weir crest, the nappe switches from the impinging jet to the surface flow regime (Wu and Rajaratnam, 1996).

This work considers the flow regimes and energy losses occurring just downstream of a sharp-crested weir for the entire range of tailwater levels. Although, the total energy loss for such weirs is already known, the objective of this study is to present an analytical treatment based on previous studies and theory of plane jet for the improved understanding of the major energy dissipation processes. For the surface flow regime, the analysis on surface jumps and surface waves are based on the experimental studies by Ahmed et al. (2018) and Rajaratnam and Muralidhar (1969), respectively. For the impinging jet regime, the first analysis considers free flow with supercritical downstream flow and no hydraulic jump based on the experimental study by Moore (1943). The second analysis in this regime considers impinging jets and jumps on nappe based on the theory of plane jet.

It should be noted that the experimental investigation in the impinging jet regime is very challenging and reliable measurements are hard to obtain since the velocity distribution is non-uniform, and the flow contains a significant amount of air bubbles. Perhaps, for this reason experimental study in this regime with carefully taken velocity profiles is still missing in the

literature. In the absence of experimental investigations, the analytical treatment shown in this study can improve the understanding of energy loss immediately downstream of a rectangular sharp crested weir. This likely can be an interesting future research project to validate the work presented herein with improved experimental techniques.

A.2 Free Flow with No Hydraulic Jump

For free flow below the weir, the falling nappe converts to a supercritical stream. Considering the region starting from the weir to the initiation of the supercritical stream, the energy loss is mainly due to the mixing behind the nappe (Moore, 1943; Rajaratnam and Chamani, 1995). There does not appear to be any experimental data on this loss, whereas for the corresponding case of flow at an abrupt drop, there are several studies (Moore, 1943; Rand, 1955; Rajaratnam and Chamani, 1995; and others]. Rajaratnam and Chamani (1995) found that the relative energy loss at an abrupt drop in a rectangular channel can be described by the equation

$$\frac{\Delta E}{E_0} = \frac{0.09}{(y_c/P)^{0.77}} \tag{A.3}$$

where ΔE is the loss of the energy head, E_0 is the energy head upstream of the drop, P is the drop height, and y_c is the critical depth of the flow. The flow for the drop and a weir of the same height is similar except the flow contraction above the weir. Since the energy loss is primarily due to the mixing in the pool behind the nappe, it is safe to assume that Equation A.3 can be used to calculate the energy loss for a weir with proper adjustment for the flow contraction. For open channel flow in a rectangular channel $y_c = (q^2/g)^{1/3}$, and for a sharp-crested weir q is given by Equation A.1 considering the flow contraction. Therefore, Equation A.3 is rewritten to describe the relative energy loss at a sharp-crested weir

$$\frac{\Delta E}{E_0} = \frac{0.09}{C_d^{0.51}} \left(\frac{h}{P}\right)^{-0.77} \tag{A.4}$$

A.3 Impinging Jet Flow and Jump on Nappe

As the tailwater level increases, a jump forms on the falling nappe (Amin et al., 2019). The shape of the nappe resembles the path of a projectile (Chow, 1959). After the nappe plunges into the tailwater as a plane jet, it keeps its trajectory as a tangent to the original path of the unsubmerged nappe at the point of impingement. This is because gravity does not affect the nappe trajectory as it gets submerged. Amin et al. (2019) reported that the slope of the submerged nappe, $\theta = 60°$ for a range of experiments with a 40.9 cm high sharp-crested weir, and flowrate q ranged between 0.04 and 0.07 m²/s. Although this slope depends on the weir height, flowrate per unit width, and tailwater depth; the slope of the nappe is quite steep. Therefore, the jump on the nappe resembles a jump on a steep slope.

Based on experiments on jumps formed on steep slopes, Rajaratnam and Murahari (1974) reported that the mean velocity profiles are similar to those within a plane wall jet rather than a jump on horizontal bed. Kawagoshi and Hager (1990) reported similar results for $\theta = 30°$, and high level of submergence. Ohtsu and Yasuda (1991) also confirmed resemblance of the velocity profiles to classical wall jets for slope $\theta>40°$. Rajaratnam (1967) concluded that for jumps on steep slopes, mixing inside the jump will not be violent and thus the energy dissipation will be less. Therefore, the energy loss below the weir for the impinging jet regime is described here adopting a model of a plane jet or plane shear layer, depending on the extent of the jet.

Consider the length of the submerged plane jet from the point of impingement on the tailwater level to the bed is L. Based on the trajectory of the nappe, L can be described as Equation A.5, for a short distance after the weir, and for velocity head less than $0.2h$ (see detailed derivation at the end of this appendix).

$$\frac{L}{y_t} = \frac{(P/h) - (y_t/h) + 0.5}{(P/h) - (y_t/h) + 0.23} \tag{A.5}$$

Following the work of Ahmed et al. (2018), the velocity of the jet V_j at the tailwater level is estimated as $\sqrt{2g(P + h - y_t)}$ using the Bernoulli equation, assuming negligible energy loss over this small drop, where $(P + h - y_t)$ is the drop height of the nappe to the tailwater surface. If $2b_0$ is the starting thickness of this submerged plane jet, then $q = 2b_0\sqrt{2g(P + h - y_t)}$. Therefore,

Equation A.1 is adopted to find the jet thickness

$$2b_0 = \frac{\frac{2}{3}C_d\sqrt{2g}h^{3/2}}{\sqrt{2g(P+h-y_t)}} = \frac{2}{3}\left(\frac{C_d h^{3/2}}{\sqrt{P+h-y_t}}\right) \tag{A.6}$$

For smaller values of h/P (≈ 0.2), C_d=0.621 (Equation A.2) and therefore, $2b_0$=0.414h/(P+h-y_t).

The energy loss of the plane turbulent jet is essentially the loss of the jet kinetic energy. Therefore, adopting the energy loss for the fully developed plane jet from Rajaratnam (1976),

$$\frac{\Delta E}{E_0} = 1 - \frac{2.64}{\sqrt{x/b_0}} \tag{A.7}$$

where x is the distance along the jet. For a value of x less than the length of the potential core (which is about 12b0), the flow must be treated as a plane shear layer or short jet (Rajaratnam, 1976). For energy dissipation in a vertical drop, Chamani and Rajaratnam (2008) also treated the flow as a plane shear layer for smaller drop height. Following their work, the relative energy loss in a short jet is described by the equation (see detailed derivation at the end of this appendix)

$$\frac{\Delta E}{E_0} = 0.007(x/b_0) \tag{A.8}$$

For the flow over a sharp-crested weir, consider a fully developed plane jet as a long jet (x/b_0 >12). Now after replacing b_0 from Equation A.6, and putting x=L, Equation A.7 reduces to

$$\frac{\Delta E}{E_0} = 1 - 1.52\sqrt{\frac{C_d h}{L[(P/h)-(y_t/h)+1]^{1/2}}} \tag{A.9}$$

Similarly, for a short jet (x/b_0 <12), Equation A.8 reduces to

$$\frac{\Delta E}{E_0} = 0.021\left[\frac{L\sqrt{(P/h)-(y_t/h)+1}}{C_d h}\right] \tag{A.10}$$

Consider the stage when the weir is just submerged, i.e., the tailwater level is equal to the height of the weir. Putting y_t=P in Equation A.5 gives, L=2.17P. Therefore, for upper regime of the impinging jet flow, Equations A.9 and A.10 reduce to Equations A.11 and A.12, respectively.

147

$$\frac{\Delta E}{E_0} = 1 - 1.03\sqrt{C_d\left(\frac{h}{P}\right)} \qquad\qquad (A.11)$$

$$\frac{\Delta E}{E_0} = \frac{0.046}{C_d\left(\frac{h}{P}\right)} \qquad\qquad (A.12)$$

Equations A.11 and A.12 are plotted in Figure A.2b. The relative energy loss decreases continuously from 0.6 to about zero for h/P increasing from about 0.2 to 6.0. The transition from long jet to short jet occurs at $h/P=1.2$, and the relative energy loss at transition is 0.06.

Although major portion of the energy loss in the impinging jet regime is described here as a result of the energy decay of a plane jet, energy dissipation also occurs due to mixing in the pool behind the nappe and in the jump at the lower stage of the tailwater level.

A.4 Surface Jump to Surface Jet

The surface jump was studied by Ahmed et al. (2018) who found that the supercritical Froude number at the start of the surface jump had a maximum value of 2.5 and that the relative energy loss varied with t/h, falling from 0.19 for $t/h=0.05$ to about 0.02 for $t/h=0.9$. The relative energy loss for a surface jump is described by the equation below (Ahmed et al., 2018)

$$\frac{\Delta E}{E_0} = 0.20\left(1 - \frac{t}{h}\right) \qquad\qquad (A.13)$$

In the surface wave regime, the relative energy loss is expected to be very small. Rajaratnam and Muralidhar (1969) studied the surface jet regime, and reported that this regime starts at $t/h>0.9$. They found that the surface flow can be considered as one-half of a plane turbulent free jet, with a velocity V_j equal to $\sqrt{2g(h-t)}$ and thickness of $0.74t$ with a potential core of a short length of $2t$. Then the relative energy loss can be described by replacing $b_0=0.74t$ for the equation for fully developed flow (Equation A.7) as

$$\frac{\Delta E}{E_0} = 1 - \frac{2.27}{\sqrt{x/t}} \qquad\qquad (A.14)$$

for a length of $5.3t$ to $20t$. Energy loss after the distance $20t$ becomes minimal as the flow gradually

decays into turbulent open channel flow (Rajaratnam and Muralidhar, 1969).

A.4 Conclusions

We have described the flow processes immediately downstream of a sharp-crested weir for different flow regimes. This analysis first considers a free flow with a low tailwater, then a hydraulic jump front forming on the falling nappe and an impinging plane jet, referred as the impinging jet regime. As the tailwater rises to the crest level, the flow gets submerged, and the surface flow regime starts. With further increase of the tailwater depth, this regime passes through a surface jump first, then a smooth surface wave, and finally to a deeply submerged surface jet regime. Although, the energy dissipation in each of these regimes can occur due to various processes, we have developed equations for the relative energy loss with a focus on the major energy dissipation in each regime, using the plane turbulent jet model. To compare the losses, it is necessary to evaluate ΔE for all the cases. The initial energy E_0 is different in these equations depending on the energy dissipation process considered.

For the supercritical stream, E_0 is the initial energy before the drop, mainly the potential energy. Therefore, $E_0 \approx P + h$. Therefore, Equation A.4 reduces to

$$\frac{\Delta E}{h} = \left[\frac{(1 + P/h)}{(h/P)^{0.77}} \frac{0.09}{C_d^{0.51}} \right] \tag{A.15}$$

$$\frac{\Delta E}{h} = 0.021 \left[\frac{L\sqrt{(P/h) - (y_t/h) + 1}}{C_d h} \right] \tag{A.17}$$

Similarly, for the upper stage of impinging jet flow, $E_0 \approx h$. Therefore, Equations A.11 and A.12 reduce to

$$\frac{\Delta E}{h} = 1 - 1.03 \sqrt{C_d \left(\frac{h}{P} \right)} \tag{A.18}$$

$$\frac{\Delta E}{h} = \frac{0.046}{C_d \left(\frac{h}{P} \right)} \tag{A.19}$$

For the surface jump, E_0 is the effective head before the jump, i.e., $E_0 \approx h\text{-}t$. Therefore, Equation

A.13 reduces to

$$\frac{\Delta E}{h} = 0.20 \left(1 - \frac{t}{h}\right)^2 \qquad (A.20)$$

Again, for the surface jet, E_0 is the initial kinetic energy of the jet, where the head (h-t) converts into the kinetic energy, i.e., $E_0 \approx h$-t. For the energy loss for $t/h = 0.9$ and $x = 2.17P$, Equation A.14 reduces to

$$\frac{\Delta E}{h} = 0.1 \left(1 - 1.46 \sqrt{\frac{h}{P}}\right) \qquad (A.21)$$

Note that the loss ΔE is significant only for the supercritical stream, especially for values of h/P less than about 0.5. For all other cases, the loss is not significant. The flow regimes and corresponding energy loss equations are described in Table A.1 as a summary of this study. The ideas and equations presented in this work present an analytical treatment of the full range of flows and the related major energy dissipation processes downstream of a rectangular sharp-crested weir, using the concept of plane turbulent jet and previous studies.

Derivation of Equation A.5

For a sufficiently high weir, (i.e., $P/h>1.33$), velocity of the approach flow is negligible. Therefore, the energy head is approximately equal to the static head, h. Now, for $x'/h > 0.5$, and the velocity head less than $0.2h$, the trajectory of the nappe for flow over a sharp crested weir can be described by the equation below (Rajaratnam & Muralidhar, 1969)

$$\frac{y'}{h} = -0.425 \left(\frac{x'}{h}\right)^2 + 0.055 \left(\frac{x'}{h}\right) + 0.150 \qquad (A.22)$$

where x' and y' represent the co-ordinates on the nappe, and y' can be expressed as a function of the weir height and the tailwater depth, i.e., $y' = P - y_t$ (see Figure A.3). Therefore, Equation A.22 reduces to

$$\frac{P}{h} - \frac{y_t}{h} = -0.425 \left(\frac{x'}{h}\right)^2 + 0.055 \left(\frac{x'}{h}\right) + 0.150 \tag{A.23}$$

Differentiation of Equation A.23 gives the tangent of the trajectory

$$\frac{dy_t}{dx} = 0.85 \left(\frac{x'}{h}\right) - 0.055 = \tan\theta \tag{A.24}$$

From the right-angled triangle the length of the jet tangent to the trajectory is given by

$$\frac{L}{y_t} = \frac{1}{\sin\theta} \tag{A.25}$$

Now for a range of values of P/h and x/h, one can find the corresponding values of y_t/h, θ, and L/y_t from Equations A.23, A.24, and A.25, respectively. Therefore, after plotting the values of L/y_t vs. y_t/h, the general equation for the jet length can be expressed as

$$\frac{L}{y_t} = \frac{(P/h) - (y_t/h) + 0.5}{(P/h) - (y_t/h) + 0.23} \tag{A.26}$$

Alternatively, Figure A.3 can be used to find L for given P, y_t, and h.

Derivation of Equation A.8

For the region from the starting of the jet to the end of the potential core of a length of $12b_0$, the main characteristics of the flow are shown in Figure A.4, which is from Rajaratnam (1976). At any section at a distance of x from the nozzle, the flow has a potential core of radius y_1, and velocity V_j, surrounded by shear layers on both sides. Consider the velocity at any point in the shear layer u at a radial distance y from the jet axis. For this flow, the piezometric pressure is approximately constant and the change in the energy of the flow is only due to the decrease in the kinetic energy due to the diffusion of the shear layer. The kinetic energy flux per unit width E^* can be written as:

$$\frac{E^*}{2} = (y_1 U_0 \rho)\left(\frac{V_j^2}{2}\right) + \int_{y_1}^{\infty} \frac{(udy\rho)u^2}{2} \tag{A.27}$$

where ρ is density of water. It is useful to point out that E is equal to E^* per unit weight and the ratio (E/E_0) is equal to (E^*/E_0^*). Equation A.27 is evaluated using the following, from Figure A.4

$$y_1 = b_0 - x \tan 4.8° = b_0 - 0.084x \qquad \text{(A.28)}$$

$$\frac{u}{U_0} = f(\eta) \quad \text{where} \quad \eta = \frac{(y - y_1)}{b} \qquad \text{(A.29)}$$

where b is the length scale, equal to $(x \tan 9.5° + x \tan 4.8°)$ or $0.126x$. The velocity distribution in the shear layer is assumed to be given by the equation below (Rajaratnam, 1976)

$$f(\eta) = e^{-0.693\eta^2} \qquad \text{(A.30)}$$

Considering the integral part of Equation A.6,

$$\int_{y_1}^{\infty} \frac{(udy\rho)u^2}{2} = 0.126x \left(\frac{\rho V_j^3}{2}\right) \int_0^{\infty} f(\eta)^3 d\eta$$

$$= 0.126x \left(\frac{\rho V_j^3}{2}\right) \int_0^{\infty} \left(e^{-0.693\eta^2}\right)^3 d\eta$$

$$= 0.126x \left(\frac{\rho V_j^3}{2}\right) \left(\frac{1}{2}\sqrt{\frac{\pi}{2.079}}\right)$$

$$= 0.077x \left(\frac{\rho V_j^3}{2}\right)$$

Now Equation A.27 reduces to

$$\frac{E^*}{2} = (b_0 - 0.084x) \left(\frac{\rho V_j^3}{2}\right) + 0.077x \left(\frac{\rho V_j^3}{2}\right) \qquad \text{(A.31)}$$

The initial kinetic energy flux per unit width $E_0{}^*$ is given by

$$\frac{E_0{}^*}{2} = (b_0 U_0 \rho) \left(\frac{V_j^2}{2}\right) \qquad \text{(A.32)}$$

Since (E/E_0) is equal to $(E^*/E_0{}^*)$, Equations A.31 and A.32 reduces to

$$\frac{E}{E_0} = 1.0 - 0.007 \left(\frac{x}{b_0}\right)$$

(A.33)

$$\frac{\Delta E}{E_0} = 0.007 \left(\frac{x}{b_0}\right)$$

(A.34)

Table A.1: Expressions for energy dissipation within different flow regimes for flow below a sharp crested weir

---

<center>A. IMPINGING JET REGIME</center>

I. Free flow with no hydraulic jump

$$\frac{\Delta E}{E_0} = \frac{0.09}{C_d^{0.51}}\left(\frac{h}{P}\right)^{-0.77} \qquad \frac{\Delta E}{h} = \left[\frac{(1+P/h)}{(h/P)^{0.77}}\frac{0.09}{C_d^{0.51}}\right]$$

II. Impinging jet flow and jump on nappe

For $x/b_0 > 12$

$$\frac{\Delta E}{E_0} = 1 - 1.52\sqrt{\frac{C_d h}{L[(P/h)-(y_t/h)+1]^{1/2}}} \qquad \frac{\Delta E}{h} = 1 - 1.52\sqrt{\frac{C_d h}{L[(P/h)-(y_t/h)+1]^{1/2}}}$$

For $x/b_0 < 12$

$$\frac{\Delta E}{E_0} = 0.021\left[\frac{L\sqrt{(P/h)-(y_t/h)+1}}{C_d h}\right] \qquad \frac{\Delta E}{h} = 0.021\left[\frac{L\sqrt{(P/h)-(y_t/h)+1}}{C_d h}\right]$$

For upper stage of impinging jet flow

For $x/b_0 > 12$

$$\frac{\Delta E}{E_0} = 1 - 1.03\sqrt{C_d(h/P)} \qquad \frac{\Delta E}{h} = 1 - 1.03\sqrt{C_d(h/P)}$$

For $x/b_0 < 12$

$$\frac{\Delta E}{E_0} = \frac{0.046}{C_d(h/P)} \qquad \frac{\Delta E}{h} = \frac{0.046}{C_d(h/P)}$$

<center>B. SURFACE JET REGIME</center>

I. Surface Jump

$$\frac{\Delta E}{E_0} = 0.20\left(1-\frac{t}{h}\right) \qquad \frac{\Delta E}{h} = 0.20\left(1-\frac{t}{h}\right)^2$$

II. Surface Jet

$$\frac{\Delta E}{E_0} = 1 - \frac{2.27}{\sqrt{x/t}} \qquad \frac{\Delta E}{h} = 0.1\left(1-1.46\sqrt{h/P}\right)$$

<center>RELEVANT PARAMETERS</center>

$$b_0 = \frac{1}{3}\left[\frac{C_d h}{\sqrt{(P/h)-(y_t/h)+1}}\right] \qquad \frac{L}{y_t} = \frac{(P/h)-(y_t/h)+0.5}{(P/h)-(y_t/h)+0.23}$$
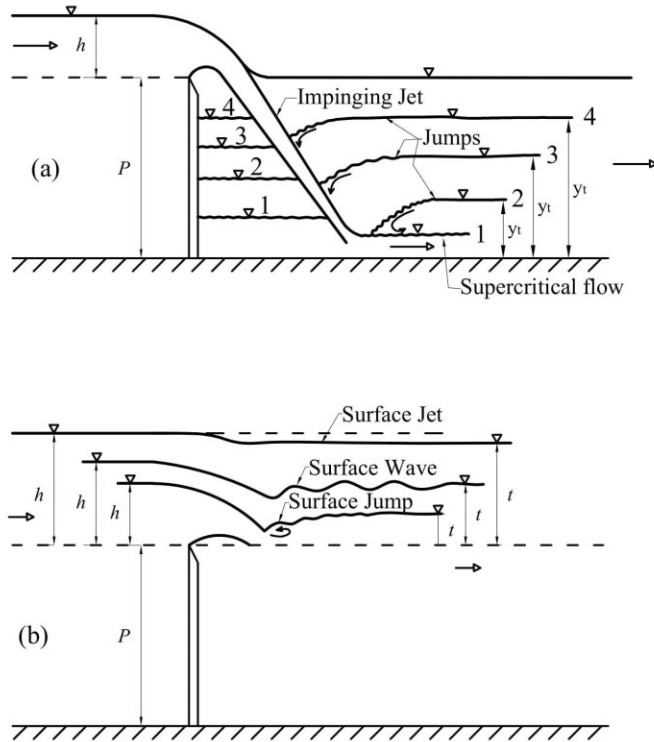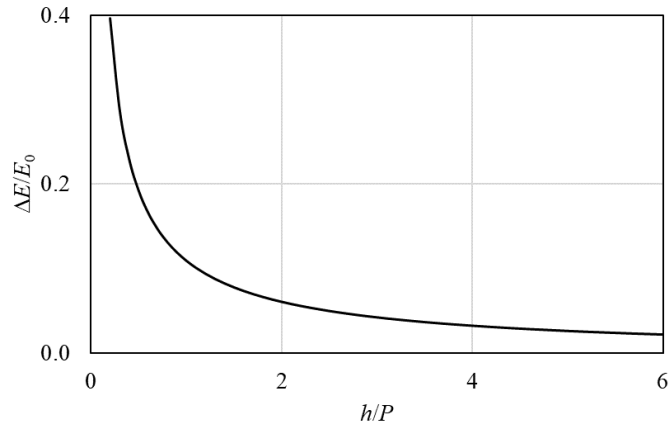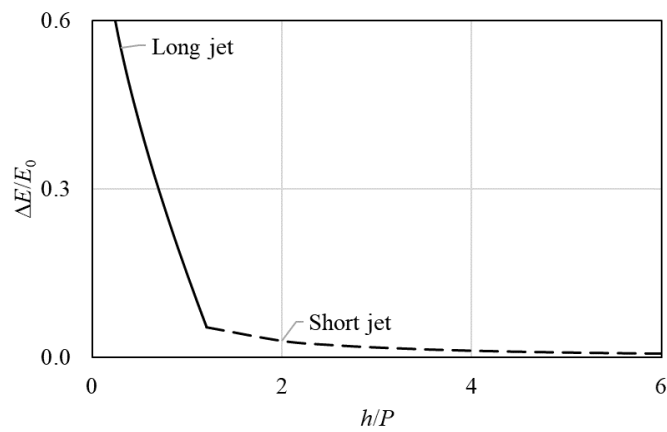
Figure A.1: Definition sketches for flow downstream of sharp-crested weirs: (a) impinging jet regime, (b) surface flow regime

(a)

(b)

Figure A.2: Relative energy loss downstream of sharp-crested weirs for (a) free flow with no jump, and (b) upper stage of impinging jet flow
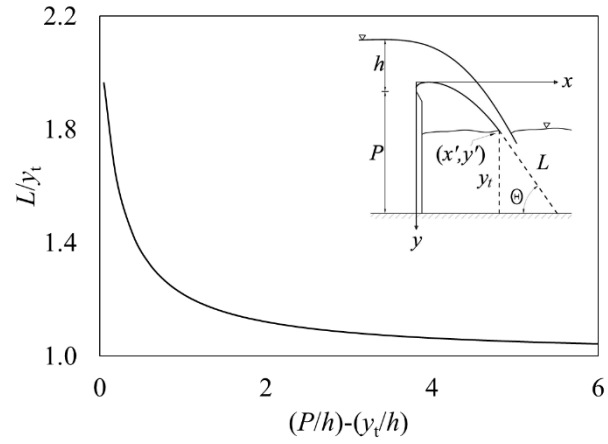
Figure A.3: Length of submerged plane jet as a function of weir height, upstream water level above the weir, and tailwater depth
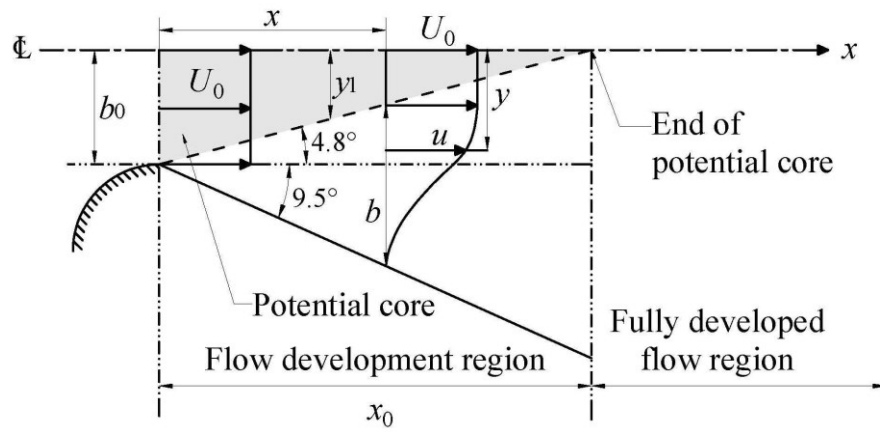
Figure A.4: Definition sketch of flow development region of plane jets (adapted from Rajaratnam, 1976)